2017

A Computational Study of the Kinematics of Femoroacetabular Morphology During A Sit-to-Stand Transfer

Brandon K. Marine
marinebk

A COMPUTATIONAL STUDY OF THE KINEMATICS OF FEMOROACETABULAR MORPHOLOGY DURING A SIT-TO-STAND TRANSFER

A thesis submitted in partial fulfillment of the requirements for the degree of Masters of Science in Biomedical Engineering at Virginia Commonwealthy University.

by

BRANDON K. MARINE
B.A. Physics, Virginia Polytechnic Institute and State University, 2014

Director: Jennifer S. Wayne, Ph.D.
Professor, Biomedical Engineering & Orthopaedic Surgery
Director, Orthopaedic Research Laboratory

Virginia Commonwealth University
Richmond, Virginia
December 2017

This thesis is dedicated to my grandmother. You were always so invested in helping me through my education and I wish you were able to see me complete it.

I love and miss you.

Acknowledgments

I would like to acknowledge all of the people who have supported and encouraged me throughout this process. First, I would like to extend my gratitude to my advisor, and fellow Hokie fan, Dr. Wayne. Along the way, you provided me with guidance though my research and a strong foundation in biomechanics that I did not have previously. You provided me with opportunities outside of coursework and research to help me familiarize myself in many areas. I am very grateful for all you have done for me over the past two and a half years.

Next, I would like to thank the other two members of my thesis committee: Dr. Kalore and Dr. Wetzel. I appreciate what both of you have done to help me through this process and the time commitment as a member of my thesis committee.

To all members of the Orthopaedic Research Laboratory, thank you for all of the collaboration and friendship over the past couple years. To Ruchi, Nathan and Johnny, you have played a major role in helping me get this far. As my first stop for questions, you guys were always willing to help as much as you could. To Rachel, Tyler and Patrick, I wish you luck over the years to come. I had a great experience and learned a tremendous amount in the lab and hope you have the same experience.

I would also like to thank my family. To my mother Robin and father Keith, thank you for always providing me with the best opportunities to succeed throughout my life and continuing to be there for me. To my brother Nolan and sister Ashlyn, thank you for all the good times we have had and I am really excited to see all of us continue to grow together.

Finally, to Lindsey I want to thank you for everything you have done to be there for me every day. From making the long drives down to Blacksburg in less than ideal weather conditions to continually dealing with my quirky personality. You have been a huge influence on my life and I am beyond grateful.

Table of Contents

List of Tables

List of Figures

List of Abbreviations

2D	Two-Dimensional
3D	Three-Dimensional
AAFD	Adult Acquired Flatfoot Deformity
ACL	Anterior Cruciate Ligament
ADAMS	Automatic Dynamic Analysis of Mechanical Systems
AIIS	Anterior-Inferior Iliac Spine
AKP	Anterior Knee Pan
Ant	Anterior
AP	Anteroposterior
AIIS	Anterior-Inferior Iliac Spine
ASIS	Anterior-Superior Iliac Spine
BMG	Bulk Metal Glass
CAD	Computer-Aided Design
CEA	Center Edge Angle
CNS	Central Nervous System
COM	Center of Mass
CT	Computerized Tomography
CV	Combined Version
DJD	Degenerative Joint Disease
DOF	Degree of Freedom
ECM	Extracellular Matrix
EMG	Electromyography
FAI	Femoroacetabular Impingement
FEA	Finite Element Analysis
HF	Hip Flexion

ILFL	Iliofemoral Ligament
Inf	Inferior
ISB	International Society of Biomechanics
ISFL	Ischiofemoral Ligament
IT	Iliotibial (IT Band)
KF	Knee Flexion
Lat	Lateral
LCL	Lateral Collateral Ligament
LH	Long Head
MCL	Medial Collateral Ligament
Med	Medial
MRI	Magnetic Resonance Imaging
MSD	Musculoskeletal Disease
OA	Osteoarthritis
PCL	Posterior Cruciate Ligament
PE	Polyethylene
PFL	Pubofemoral Ligament
Post	Posterior
PIIS	Posterior-Inferior Iliac Spine
PSIS	Posterior-Superior Iliac Spine
PT	Pelvis Tilt
PTFE	Polytetrafluoroethylene
RA	Rheumatoid Arthritis
RBM	Rigid Body Motion
RMSE	Root Mean Square Error
RMSD	Root Mean Square Deviation

SH	Short Head
SIMM	Software for Interactive Musculoskeletal Modeling
STL	Stereolithographic
STS	Sit-to-Stand
Sup	Superior
TFL	Tensor Fasciae Latae
THA	Total Hip Arthroplasty
UHMWPE	Ultra-High Molecular Weight Polyethylene

Abstract

A COMPUTATIONAL STUDY OF THE KINEMATICS OF FEMOROACETABULAR MORPHOLOGY DURING A SIT-TO-STAND TRANSFER

Brandon K. Marine

A thesis submitted in partial fulfillment of the requirements for the degree of Masters of Science in Biomedical Engineering at Virginia Commonwealthy University.

Director: Jennifer S. Wayne, Ph.D.
Professor, Biomedical Engineering & Orthopaedic Surgery
Director, Orthopaedic Research Laboratory

Virginia Commonwealth University
Richmond, Virginia
December 2017

Computational modeling in the field of biomechanics is becoming increasingly popular and successful in practice for its ability to predict function and provide information that would otherwise be unobtainable. Through the application of these new and constantly improving methods, kinematics and joint contact characteristics in pathological conditions of femoroacetabular impingement (FAI) and total hip arthroplasty (THA) were studied using a lower extremity computational model. Patients presenting with FAI exhibit abnormal contact between the femoral neck and acetabular rim leading to surrounding tissue damage in daily use. THA is the replacement of both the proximal femur and acetabular region of the pelvis and is the most common surgical intervention for degenerative hip disorders. A combination of rigid osteoarticular anatomy and force vectors representing soft tissue structures were used in developing this model. Kinematics produced by healthy models were formally validated with experimental data from Burnfield et al. This healthy model was

then modified to emulate the desired morphology of FAI and a THA procedure with a range of combined version (CV) angles. All soft tissue structures were maintained constant for each subsequent model. Data gathered from these models did not provide any significant differences between the kinematics of healthy and FAI but did show a large amount of variation in all THA kinematics including incidents of dislocation with cases of lower CV angles. With the results of these computational studies performed with this model, an increased understanding of hip morphology with regards to STS has been achieved.

Chapter 1: Introduction

1.1 Overview of Biomechanics Research

The field of biomechanics takes a mechanical approach towards studying biological systems at multiple scale levels. On a cellular level, mechanical interactions have become a popular and promising area of research in investigating causes of pathological situations. Cells have a constant mechanical interaction with their neighboring cells thus affecting their behavior. For example, formation of extra-cellular matrix (ECM) is being studied to understand the role mechanotransduction signals have between cells and their underlying substrate. Stem cell differentiation and, to an extent, cancer detection are both believed to be affected by the cells biomechanical behavior [1–3]. On a higher scale level, biomechanics can be used to study systems such as musculoskeletal, cardiovascular, and respiratory [4–6]. The musculoskeletal system primarily comprises structures, or tissues, involved in force transmission, locomotion, and structural support. Each tissue provides a unique function and contributes to the overall behavior of the system as a whole. Biomechanics of this system is studied primarily through investigating various healthy and diseased states and then applying that information towards improving the functionality of various musculoskeletal tasks [4, 7, 8].

To achieve an increased understanding of musculoskeletal system behavior, both experimental and computational approaches have been pursued. Typically, experimental work is separated into two different categories; cadaveric studies and clinical studies. During experimental clinical studies, data is gathered directly from patients regarding the devices or tissues being investigated. A comparison can then be made either between a single patient both pre- and post-operatively or between several patients displaying different symptoms of a similar disorder [7]. This is effective for learning the overall success of a procedure or

device in addition to providing general measures, such as range of motion. Clinical studies, however, are not capable of providing some important biomechanical measurements such as muscle forces and joint stresses due to the invasive nature of the techniques necessary for obtaining this information. Experimental cadaveric studies allow for a target region within the musculoskeletal system to be accurately analyzed using various testing equipment. Cadaveric studies are able to provide useful information regarding localized regions of the human body such as bone resection, implant placement and tissue strength amongst others [9–11]. Typically, preparing a successful cadaveric experiment requires expensive equipment along with the acquirement and storage of a cadaver and therefore, the cost tends to be much higher compared to other options. Cadavers also contain the possibility of tissue degeneration over time leading to alteration in material properties and potentially unreliable results. That being said, proper cadaveric studies are apt at finding information like joint stresses and strains as well as material properties for the various tissues found in the musculoskeletal system [12, 13]. As it is not currently possible to easily and humanely perform biomechanical testing on live tissue structures, cadavers remain the best experimental option for obtaining these results.

More recently, the field of computational biomechanics has grown profoundly in success and popularity and is becoming an alternative to the more traditional practices. Utilizing mathematical models with a foundation of data gathered from the aforementioned experimental studies allows for a diverse range of physiological parameters to be quantitatively studied without the need for patients, cadavers or additional equipment. Utilizing computational biomechanics requires not only an understanding of the anatomical environment but also a fundamental understanding of the mathematical foundations to perform an analysis. This field has a great deal of potential for gathering information not obtainable through experimental methods.

1.2 Computational Modeling

Computational modeling applied to the field of biomechanics has become an increasingly popular and reliable means to study many aspects of biological systems. It provides an approximation that relies on various physical and physiological constraints to determine an end result, the accuracy of which depends entirely on the input parameters. With the development of more powerful computers, increasingly complex and dynamic models are able to be developed and analyzed more efficiently. More specifically, models containing more components and allowing higher degrees of freedom controlled through the use of applied forces and body contact can be studied accurately and efficiently. However, introducing more complexity and higher levels of freedom consequently increases the potential sources of error [14, 15]. Therefore, it is essential that each model be validated against experimental data known to have confidence in the results [15]. A properly validated computational model is capable of performing analyses not possible in an experimental setting, whether clinical or cadaveric. Furthermore, the predictive capacity for computational modeling improves upon the potential of the more traditional experimental means.

1.2.1 Types of Computational Modeling

Finite Element Analysis (FEA) and Rigid Body Motion (RBM) are the two primary forms of computational modeling. Both cases are mathematically complex and have been proven to be useful means for performing mechanically-based analyses. They differ, however, in the type of information that they can provide. FEA serves as an accurate alternative to experimental techniques in providing deformable body information about a given sample such as stress and strain [16]. However, the amount of computational power required for these types of calculations is exceptionally large and therefore simplifications or idealizations are made. FEA is based on breaking a complex domain into a finite number of nodes and elements, each containing specific data pertaining to its location and properties. Each node

or element utilizes mathematical models comprised of a combination of physical equations and interpolation functions to provide an estimation of the resulting outcome. FEA is capable of being applied to a range of situations such as fluid flow, mechanical loading, and heat transfer [16]. Pertaining to biomechanical research, FEA is capable of providing an understanding about how tissues or different implanted devices will handle the applied loads in their native or altered environment [17]. It has been proposed that information from finite element analyses may also be able to provide insight into the etiology of some common disorders. For example, the potential relationship between hip morphology and development of osteoarthritis in the hip joint has been suggested and studied extensively [18, 19]. Finite element analysis has been proposed as a means of quantifying this relationship between pathology and morphology [20].

RBM allows for an effective alternative to experimental testing for studying the interaction of forces and solid body motion and how one affects the other [14]. As the name suggests, rigid body motion assumes each individual body to be rigid and thus removes the contributions of deformation to the analysis. This approximation is acceptable in situations where the resulting strain in the bodies will be much less than 1% or essentially zero, or where the questions posed do not require a deformable body model. High stiffnesses seen in bones provide these infinitesimal strain values and make RBM an appropriate means of investigating skeletal motion. Soft tissues, however, experience higher levels of deformation and thus FEA is more appropriate. Including soft tissue structures as a means for controlling and maintaining stability in RBM becomes a challenge that is constantly requiring creative solutions for implementation. Each soft tissue has its own individual size, shape and behavior that need to be considered in implementation into the model. Line of action, force behavior and primary function all need to be considered.

Calculations that go into solving these rigid body models become greatly simplified by removing deformation of the major bodies, thus cutting down on the required computational

power and subsequently the about of time required to solve. Early rigid body models included an additional level of simplification through constraining the joints motion to a single degree of freedom (DOF) such as a hinge. Utilizing the true contact between articulating surfaces and surrounding soft-tissue support as a control for joint motion is a much more accurate and realistic option for providing insight about joint function and kinematics. RBM has two different forms depending upon the flow of calculations relative to how motion actually occurs. Forward dynamics estimates kinematics produced by a given force or set of forces. In contrast to this, inverse dynamics analyzes a given motion for a system and estimates the forces necessary. Forward kinematic calculations were used in this thesis to study how sit-to-stand motion varies based on altered body or skeletal form whilst maintaining consistent muscle forces.

1.2.2 Software Packages

There are several software packages capable of performing FEA and RBM. Each differ in user interface simplicity, complexity of problems, etc. For example, SIMM (Software for Interactive Musculoskeletal Modeling, Musculographics Inc., USA) is able to solve the necessary governing equations for RBM but idealizes joints to permit rotation around single points or axes. Motions are based upon a predefined coordinate system and points of rotation for each part rather than the actual interaction between parts. Anybody (AnyBody Technology A/S, Denmark) is another, more recent, option that is very similar in its capabilities than SIMM but still lacks the ability to base motion on true anatomical constraints.

Alternatively, SolidWorks (SolidWorks Corp. Concord, MA) is a 3D computer-aided design (CAD) software commonly used in modeling solid bodies. Within the SolidWorks interface are add on packages Simulation and Motion capable of performing FEA and RBM analyses respectively. SolidWorks Motion relies on the ADAMS solver (Automatic Dynamic Analysis of Mechanical Systems, MSC Software Corp, USA) which utilizes user-defined constraints along with the volumetric shape of interacting parts to dictate the resulting kinemat-

ics instead of specifying simplified joints that could lead to inaccurate motion. Additionally, ADAMS is capable of providing information about volumetric overlap between bodies for determining the repelling contact forces [21]. SolidWorks Motion allows for more freedom in that the analysis is fully user-generated and the degree of constraint and simplification is highly customizable. Various part interactions, customizable force and damper elements along with external fixations provide control over this higher DOF when using SolidWorks Motion. This methodology has been used extensively within biomechanics research as an option for anatomical kinematic studies [22–25].

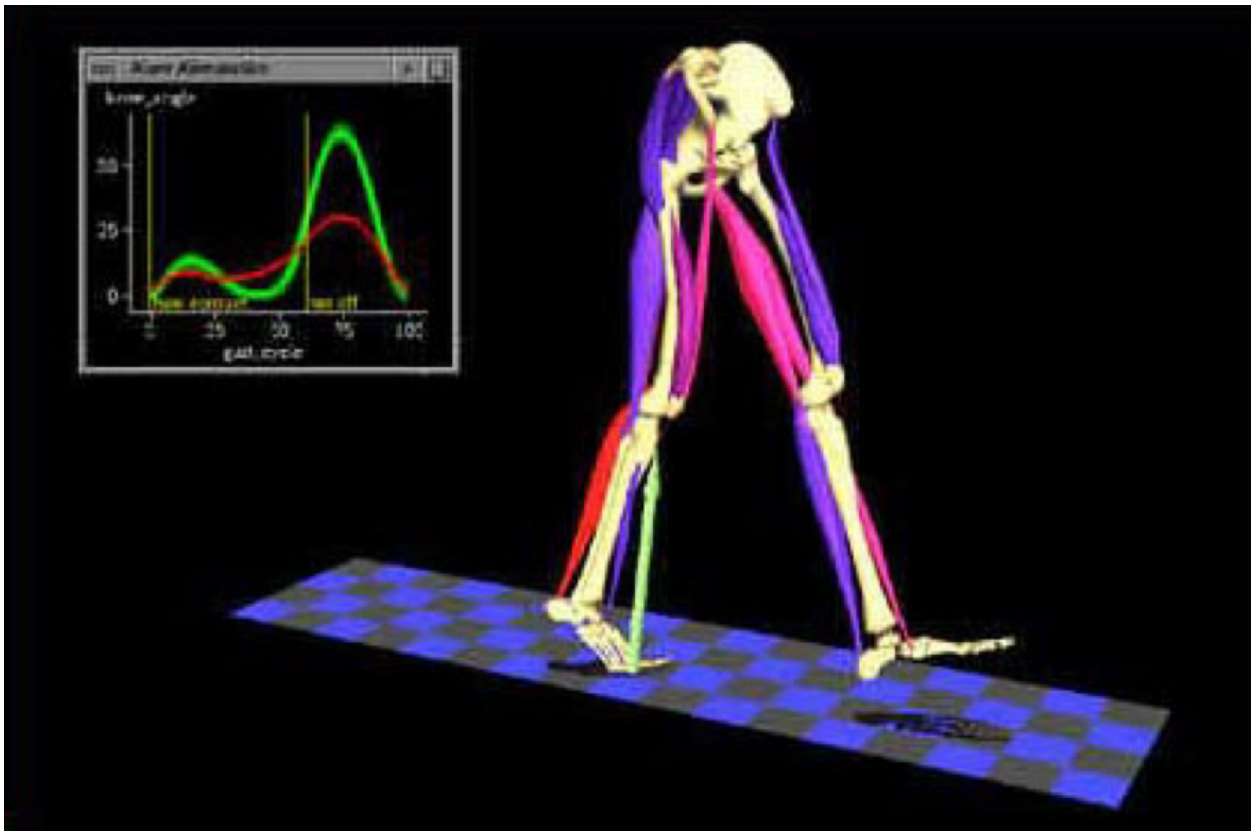

Figure 1.2-1: Image taken from the Musculographics website displaying the interface of SIMM and a typical simulation of gait with muscle colors signifying activation state [26].

1.3 Hip Joint Modeling

The femoroacetabular joint, more commonly referred to as the hip joint, is a diarthrodial ball-and-socket joint containing the femur and pelvis as well as a complex network of soft tissue anatomy. Due to this arrangement, with all six degrees of freedom permitted and high magnitudes of loading experienced through daily tasks [27], it is prone to both musculoskeletal disorders (MSDs), such as femoroacetabular impingement (FAI), dysplasia and labral tears, as well as degenerative joint disease (DJD) or osteoarthritis (OA). Femoroacetabular impingement occurs as a result of a bony overgrowth in the anterosuperior region of either the femoral neck or the acetabulum bringing about unusual contact between the femur and pelvis tissue damage and painful joint motions [28–32]. Damage from FAI is typically a result of repetitive motions rather than a single traumatic incident [8]. DJD typically develops with age from high frequencies of hip joint usage and motion. Total Hip Arthroplasty (THA) is the most common surgical intervention for DJD by replacing previously damaged tissue with artificial, inorganic materials [33]. THA has proven to be a successful approach in correcting pain and motion hindrances but improper placement and implementation of the implants can produce separate issues of impingement and dislocation [34–36].

In consideration of these issues, the hip joint is a common area of musculoskeletal research. Previous studies involving the hip joint have taken advantage of the aforementioned computational and experimental techniques to understand kinematic, contact and interaction between the structures through many situations in the hip joint [37–39]. For example, a recent finding suggests there is an association between anterior knee pain (AKP) and hip morphological alterations such as FAI. Clinically, this relationship has been observed and thus was investigated retrospectively through follow-up studies on patients presenting with AKP secondary to being diagnosed with FAI [39]. Typically, studies involving the relationship between hip pathology and kinematics have been done experimentally using patients and expensive marker systems to track the joint movements [7, 40, 41].

Computationally speaking, previous work on the hip joint has focused primarily on static relationships between the skeletal parts. Finite element studies have been done in joint contact analyses or joint capsule strength [17, 42]. A study by Weiss et al used FEA in an attempt to understand how the labrum is able to assist in load support across the hip joint through different situations [43]. Information such as this is difficult to acquire experimentally as a consequence of both the size and placement of the labrum. Gathering stress and strain information for an intricate structure such as the labrum is much less rigorous computationally through FEA. Rigid body motion is a relatively untouched area with respect to the hip joint. There has been a study utilizing a forward dynamic rigid body computational model to study how proximal femur deformities affect the full hip joint range of motion but there has yet to be a rigid body model of the lower extremity developed for more dynamic situations such as sit-to-stand (STS) [44]. Inverse dynamic models have provided estimations of muscle force magnitudes based upon body motion for various activities including gait and STS [45, 46]. This information helps to provide data necessary to develop more robust and complex computational models.

1.4 Objective

With the STS transfer being one of the most commonly performed activities of daily living and the prevalence of both FAI and total hip arthroplasties (THA), there is a need to examine how either case affects the joint during a STS movement [47, 48]. Factors such as pain and damage cannot be quantified or measured computationally, but can be inferred via force and contact analyses. Biomechanical parameters such as joint reaction forces, altered kinematics and muscle forces can be easily investigated computationally and cannot always be found efficiently experimentally. Additionally, it has already been mentioned that there is very little work done in the realm of computational rigid body modeling for the hip joint. As a result, this work involves the development of such a model for understanding how

hip morphology impacts hip mechanics during a sit-to-stand transfer. More specifically, the effect of alterations in proximal femur morphology for both native tissue and replacement cases were investigated. Initially a healthy, non-symptomatic lower extremity model was developed, examined and compared against experimental data for validation. This data was then used as a base for comparison against models with altered femoral morphology such as FAI and THA. Ultimately, results from this study will provide insight on how these morphological alterations affect a commonly performed task of STS through kinematics and joint contact regions with the hope of providing a better indication of potential issue to arise from performing STS with these conditions.

Chapter 2: Anatomy Overview

2.1 Introduction

The lower extremity is a complex network of soft and hard tissues that permits the activities of daily living performed by people. Tasks such as gait and sit-to-stand are relatively simple and overlooked visually but require a complex interplay among the different tissues coupled with a high magnitude of force output from muscles. These tissues include skeletal anatomy, providing the structural support, layers of muscles that generate necessary locomotive forces and additional soft tissue structures for flexibility as well as restraint. The aforementioned movements of walking and rising from a seated position involve primarily flexion and extension in the hip, knee and ankle (Figure 2.1-1) as well as some other minor movements within the foot. Human lower extremities are responsible for withstanding approximately 60% of total body weight and thus there can be impactful deviations from typical motion with just slight anatomical variations [49].

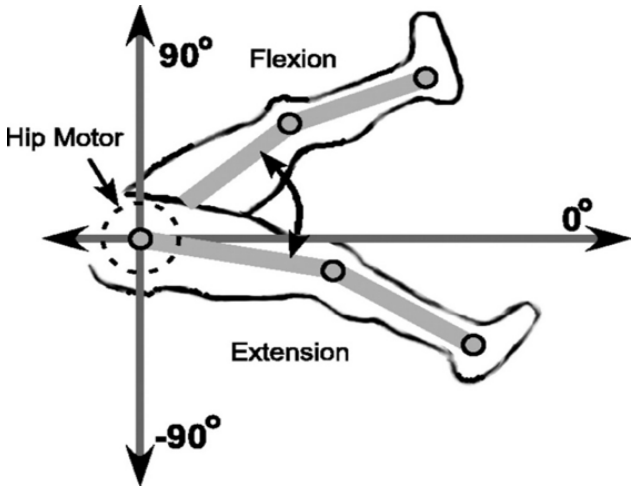

Figure 2.1-1: Lower extremity motions in the hip along the mid-sagittal plane. The knee and hip flexion and extension motions occur in this plane [50]

2.1.1 Skeletal Anatomy

Excluding the foot and ankle, the lower extremity only contains a handful of skeletal structures including the femur, tibia, fibula, patella and pelvis. The femur is the longest bone in the human body, stretching from hip joint to knee joint [51]. Long bones contain an outer, dense cortical layer containing a stiff, nearly-rigid shell providing a frame for motion and body support as well as a calcium reserve for body nutrition. Within this cortical shell is a second layer called cancellous or trabecular bone. Trabecular bone is more deformable than cortical bone and typically resides in the epiphyseal regions of the long bones allowing for better distribution of loads experienced within the joints at either end [52]. Along the shaft is a diaphysis region closing at either end at metaphysis regions (Figure 2.1-2). This metaphysis region is where bone growth primarily occurs during maturation [53,54]. With regards to the femur, distally the condyles and epicondyles form a rounded articulating surface promoting knee rotation (Figure 2.1-4) while the proximal portion contains the ball-like head that provides rotational motion in the hip joint (Figure 2.1-3). This head attaches to the femoral shaft via a cylindrical neck and articulates with the acetabulum of the pelvis [55].

The pelvis contains two irregularly shaped bones, each referred to as a hemipelvis, marking the other half of the hip joint (Figure 2.1-5). These two bones meet anteriorly at the pubic symphysis and posteriorly at the sacrum. Each individual hemipelvis is made up of three sections called the ilium, ischium and pubis which are all fused together and meet at the acetabulum. During developmental years, triadiate cartilage connects these three sections allowing for acetabular growth synchronous with femoral head growth. After puberty, the pelvis takes its final form with the full fusion of the three sections [56, 57]. The acetabulum is an inferolaterally facing cup-like feature which constitutes the "socket" portion of the hip joint cupping the femoral head and allowing for various rotational movements and some slight translational motion. The depth and amount of which the acetabulum wraps around the femoral head contribute to defining the joint range of motion. A healthy hip joint

permits approximately 120° of flexion, 25° of extension, 45° of abductions, 25° of adduction, 15° of internal rotation and 35° of external rotation [58, 59].

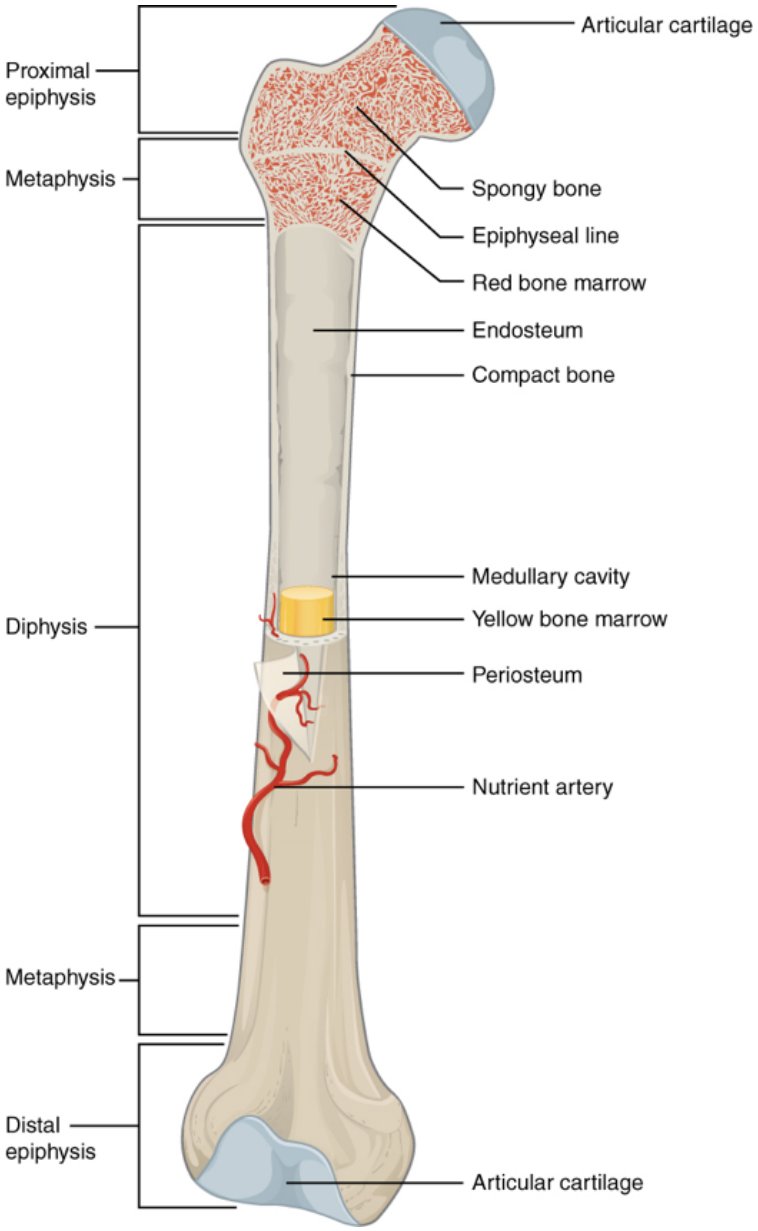

Figure 2.1-2: The structure of a long bone including the five primary regions along with a section cut of the upper half to show cortical (compact) bone and trabecular (spongy) bone [60]

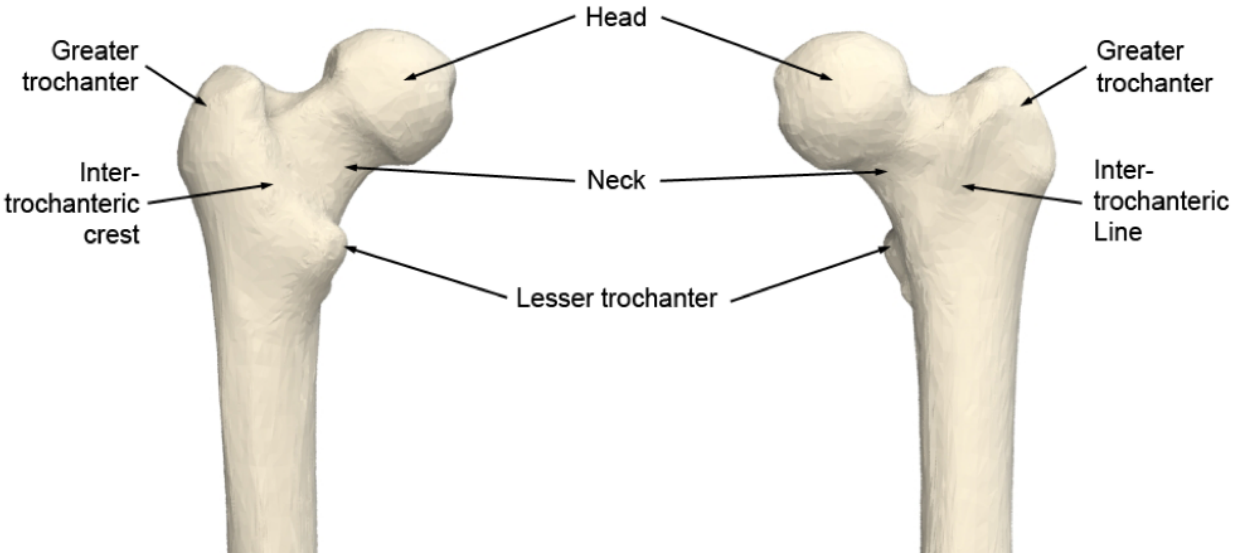

Figure 2.1-3: Anterior and posterior views of the proximal femur with key features highlighted.

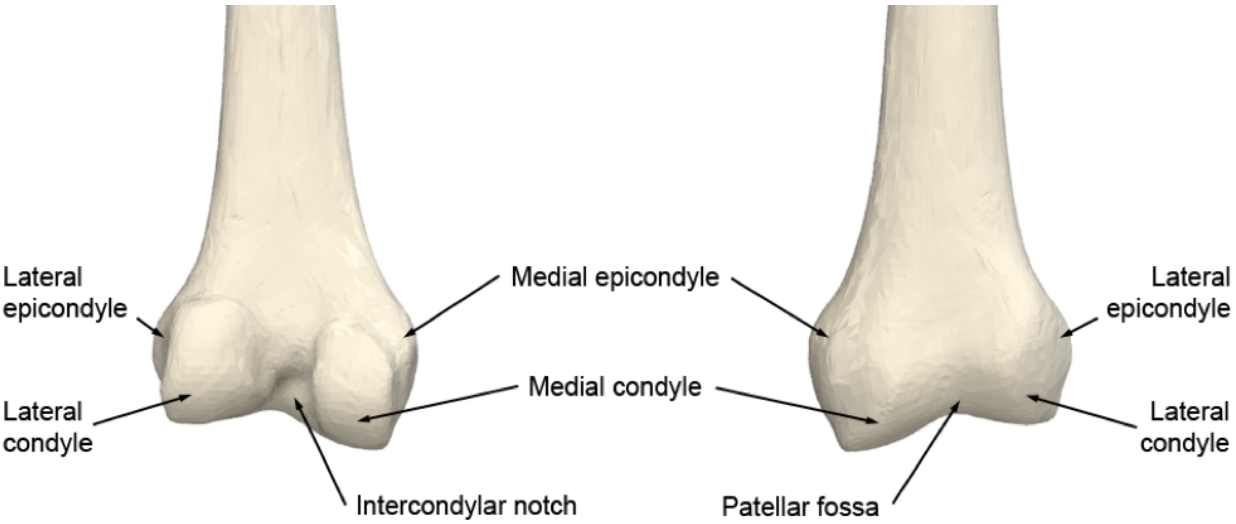

Figure 2.1-4: Anterior and posterior views of the distal femur with key features highlighted.

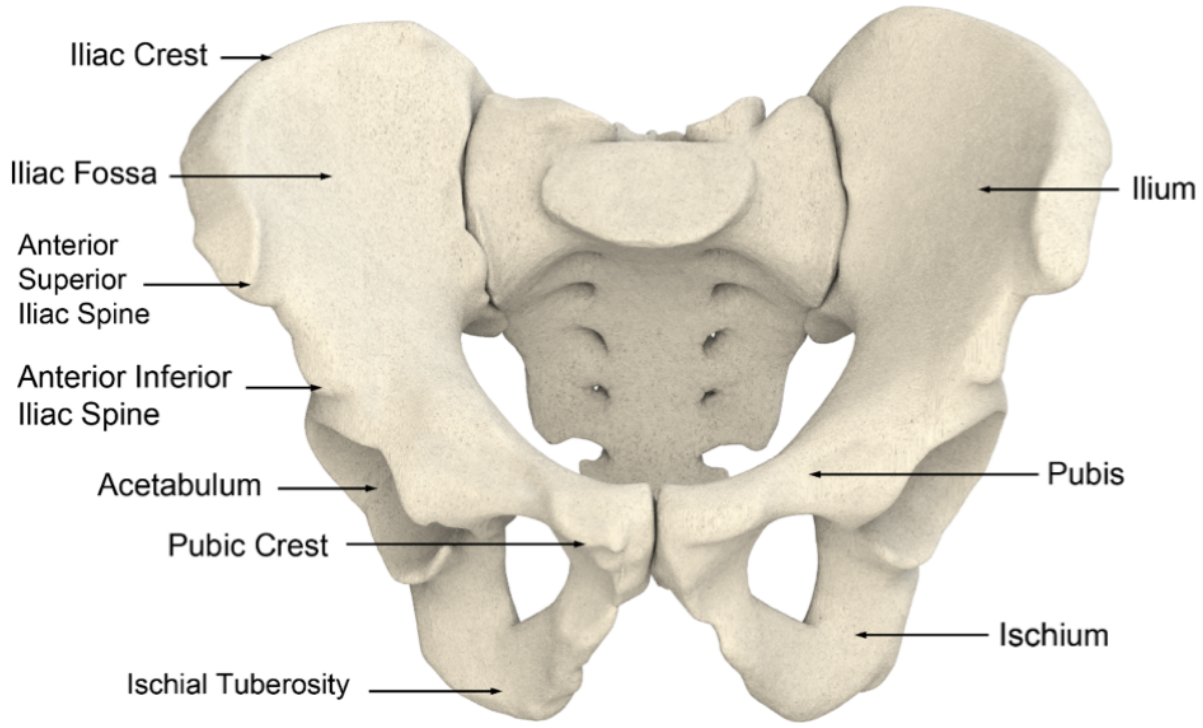

Figure 2.1-5: Anterior view of the full pelvis with key features highlighted. The sacrum of the spine is included in the image but is not labeled.

Morphology in the hip joint plays a large role in determining range of motion and is an area largely affected by abnormal pathology. Regions of overgrowth in either the proximal femur or acetabulum can reduce the range limits while a lack of acetabular coverage compromises the innate stability typically provided by the hip joint. These disorders are referred to as femoroacetabular impingement and hip dysplasia respectively. Quantifying this morphology is done through measures such as anteversion and inclination angles, alpha angle and center-edge angle (CEA) to describe proximal-distal relationship in the transverse and frontal planes as well as the femoral head and acetabular cup shape [61]. Femoral anteversion and inclination along with the alpha angle are used to describe femoral morphology. With the alpha angle, a circle closely defining the femoral head contour is placed over the 2D radiographic image. A line between the center of this circle and the point of bony defect

is connected to the line defining the neck axis passing through the center of the circle. The alpha angle is defined as the angle between these two lines. Femoral anteversion and inclination describe femoral neck orientation in the transverse and frontal planes respectively and will be discussed more in Chapter 5. Similar to the femoral head, the acetabulum contains measures used for quantifying its morphology such as acetabular version, acetabular inclination and a center-edge angle [61]. Acetabular version and inclination are angular measurements describing the orientation of the acetabulum relative to anatomic planes while CEA describes the acetabular coverage. More specifically, CEA is the angle between a line perpendicular to the horizontal plane starting at the center of the femoral head and a line connecting the lateral-most aspect of the acetabulum with the center of the femoral head. Acetabular anteversion and inclination will be discussed more in Chapter 5. Both acetabular measures along with the femoral measures are instrumental in the diagnosis of FAI in addition to pre-operative planning and placement of total hip arthroplasty.

Further distal, in the shin or lower portion of the leg, there are the tibia and fibula. The tibia is the stronger of the two and thus bears more weight while the fibula provides some mobility. Each run roughly parallel to the other with the tibia being medial to the fibula. These two bones connect proximally at the knee joint, though the fibula does not directly articulate with the femur. Distally, the two create the tibiotalar, or ankle joint, contributing to the mortise joint with the lateral malleolus [62]. Interaction between them allows for the inversion and eversion motions of the foot through rotation of one around the other. Both the tibia and fibula are long bones and have a similar structure to the femur with a diaphysis capped closed on either end with a metaphysis and epiphysis [63].

2.2 Soft Tissue Anatomy

Throughout the lower extremity exists a complex network of ligaments, muscles and tendons that provide functional movements. Most commonly known are the knee ligaments anterior cruciate ligament (ACL), medial collateral ligament (MCL), posterior cruciate ligament (PCL) and lateral collateral ligament (LCL). Injury to the ACL is a frequent issue experienced in athletics as a consequence of quick, lateral motions and leads to destabilization of the knee joint [64]. Within the hip joint, however, there is a fibrous network of ligamentous structures surrounding the femoral neck known as the joint capsule, a fibrocartilaginous ring along the acetabular rim called the labrum, articular cartilage on both the femoral head and acetabulum, a series of muscles driving the actual motions and a small fibrous band, called the ligamentum teres, connecting the fovea capitis to the acetabular notch [37, 43, 65–67]. Proper joint function is reliant upon each of these tissues performing synergistically. Detailed explanations on their function within the hip joint is discussed throughout this section.

2.2.1 Hip Capsule Ligaments

The hip joint capsule contains the iliofemoral ligament (ILFL), pubofemoral ligament (PFL) and ischiofemoral ligament (ISFL) and serves to connect the pelvis to the femur (Figure 2.2-1) [30, 68]. Generally, ligaments are composed primarily of collagen Type I fibers in a parallel arrangement. For the joint capsule, these fibers mostly run longitudinally, relative to the femoral neck, originating near the acetabular rim and then attaching along the intertrochanteric line of the femur [69]. Functionally, they help in maintaining joint stability by preventing hip distraction in addition to limiting range of motion. There is a slight spiral orientation of the joint capsule that tightens more in end-range for hip extension than in hip flexion thus limiting extension as well as rotational motion more [69, 70]. The thickness and true fiber arrangement are dependent on location and help in discerning each

individual ligament. More anteriorly lies the thicker ILFL with fibers that split between two bands: the superior and inferior portions. The superior ILFL originates proximally from the lower portion of the anterior inferior iliac spine (AIIS) and run horizontally where it attaches distally to upper portion of the intertrochanteric line. The inferior ILFL originates on the iliac portion of the acetabular margin and runs more downward to the lower part of the intertrochanteric line [69,71]. Both bands of the ILFL tighten and provide most stability in hip extension while being completely lax in hip flexion. Being the thicker part of the capsule, the ILFL displays a higher stiffness ($97.8 \pm 67.5\, N/mm$ and $100.7 \pm 54.0\, N/mm$ for the superior and inferior respectively) and is stronger than both the PFL and ISFL [12].

The PFL originates proximally between the obturator crest and superior ramus of the pubis bone and runs longitudinally where it meets with the distal part of the inferior ILFL [71]. It is thinner and thus less stiff than the ILFL ($35.8 \pm 19.8\, N/mm$) [12,72]. This ligament primarily serves to limit motion in abduction and therefore is at its greatest length when the hip is in that position [69]. Finally, the ISFL lies on the posterior of the femoral neck axis, originating proximally at the ischial circumference of the acetabular rim and inserting distally at base of the greater trochanter. This ligament runs in a spiral-like manor and has a similar reported stiffness as the PFL ($36.9 \pm 24.4\, N/mm$) [69].

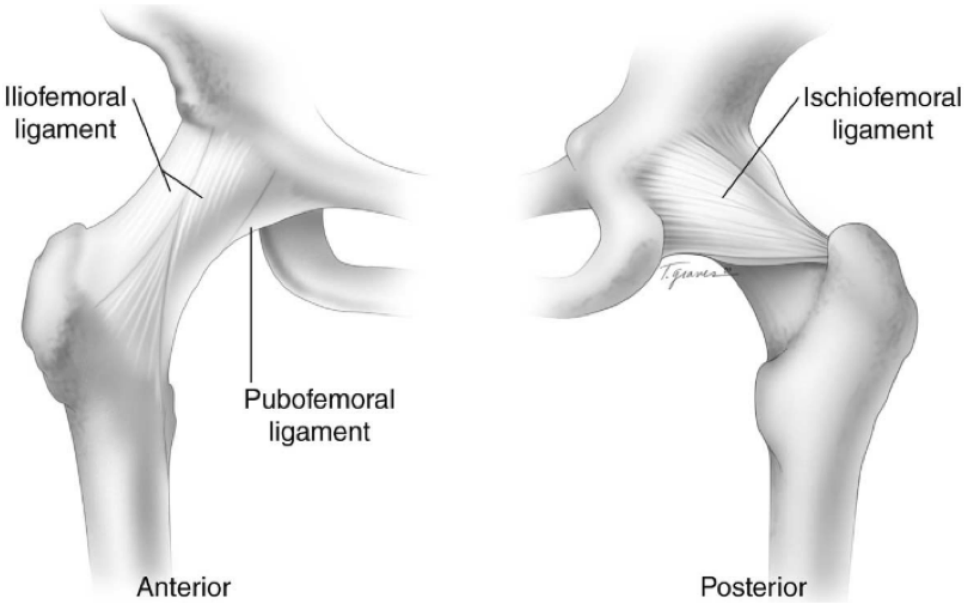

Figure 2.2-1: Each of the three hip capsular ligaments and their locations along the femoral neck. Each has unique fiber orientation and this can be seen here [70].

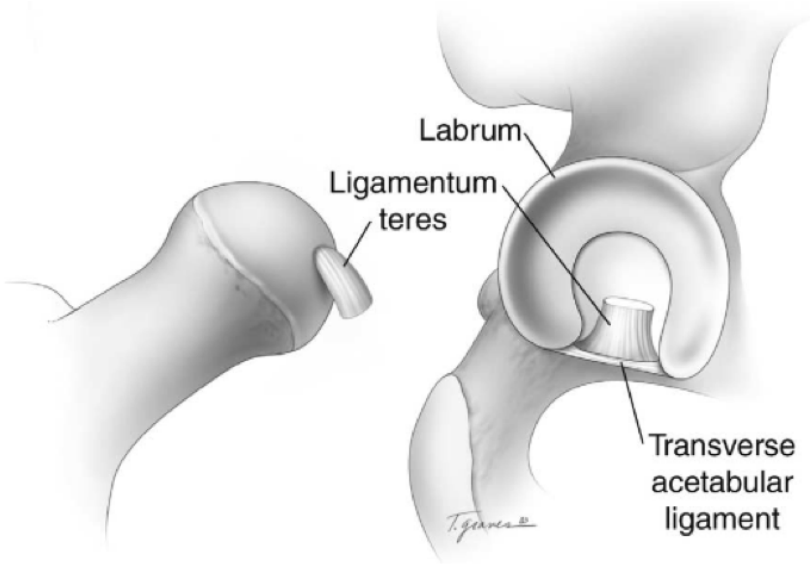

Figure 2.2-2: A femur dislocated from the acetabulum to visualize the labrum and ligamentum teres from within the interarticular space [70].

2.2.2 Articular Cartilage

Both the femoral head and acetabular surfaces contain a layer of hyaline articular cartilage comprised primarily of a network of type-II collagen, proteoglycans and interstitial fluid (Figure 2.2-2) [65]. The collagen and proteoglycans together form the primary cartilage ECM which is maintained by chondrocytes. The ECM and fluid combine to determine the overall mechanical properties of the cartilage [73, 74]. As previously mentioned, the hip joint undergoes a diverse range of motions and experiences a variety of loads in performing the functional tasks of gait or rising from a chair [27]. Bone on bone contact can lead to damage under these conditions if it occurs continuously and thus these cartilage layers act to cushion and reduce friction in the joint. On an instant applied load, such as jumping, the interstitial fluid pressure plays a large role in raising the tissue stiffness value and maintaining an adequate repulsive force. However, under a more prolonged applied load, this fluid is dispersed through the tissue causing the proteoglycans to be the primary factor in the stiffness value [73, 74].

Both femoral and acetabular articular cartilage layers are relatively thin, ranging from approximately $1.0mm$ to $2.5mm$ in thickness, and are highly organized into zones based on depth and makeup. Superficially, there are primarily thin collagen fibers running parallel to the articular surface providing mostly tensile strength [65, 75]. Below this, is a middle layer containing spherical chondrocytes, larger collagen fibers and proteoglycans in a more random and scattered orientation and a deep layer with columnar collagen fibers fixed perpendicularly to the articulating surface providing additional tensile strength. Both femoral and acetabular cartilage are fixated to the underlying bone by a layer of partially calcified cartilage [76–78].

2.2.3 Acetabular Labrum

The acetabular labrum is a fibrocartilaginous ring lying around the rim of the acetabular cup (Figure 2.2-2, Figure 2.2-3). It typically has a triangular cross-section that spans nearly the entire bony rim of the acetabulum, connecting on both sides to the transverse acetabular ligament [43, 79]. This connection is difficult to discern due to their visual continuity. In the same fashion, the labrum is difficult to discern from the articular cartilage which covers the acetabular surface [80].

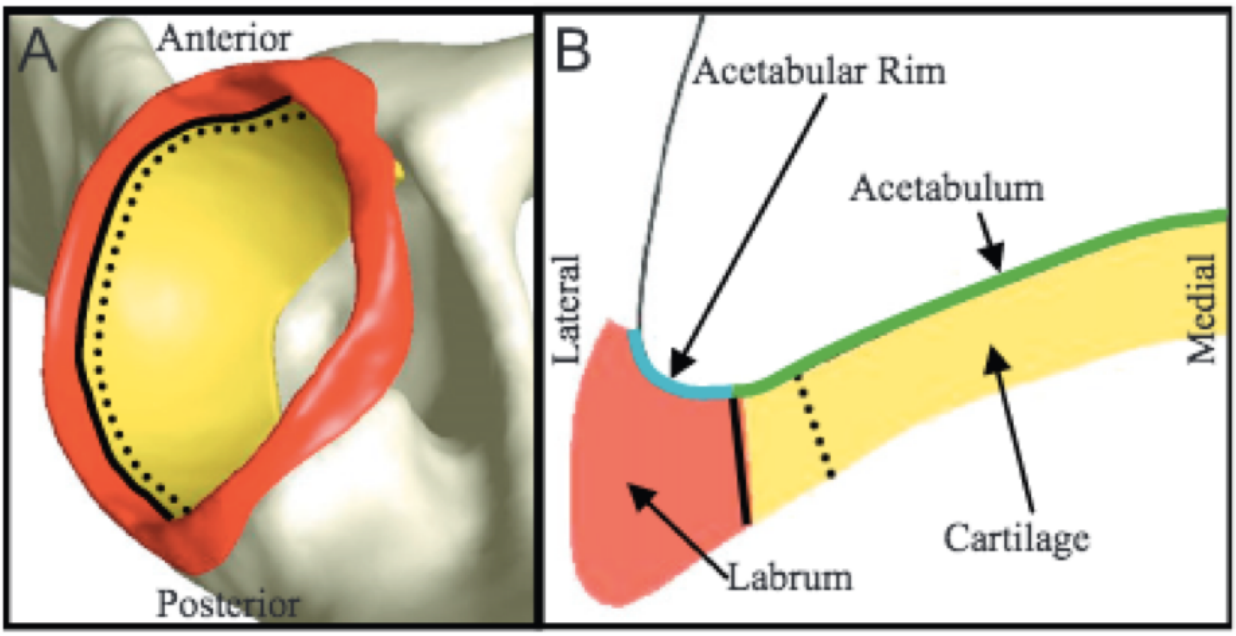

Figure 2.2-3: The labrum (red) acts as a continuation of the acetabular cartilage (yellow) with a transition zone between the solid and dotted lines. Visually these tissues are difficult to discern. (Left) A 3D representation of the labrum and acetabular cartilage positioned within the acetabulum. (Right) A section view showing the continuity between cartilage and labrum [43].

Collagen is the most predominant part of the labral structure and is intermixed with proteoglycans to provide its compressive strength. More specifically, circumferential, type-I collagen fibers are arranged in bundles parallel to the acetabular rim with some obliquely oriented fibers scattered throughout and no fibers oriented radially [81]. These type-I collagen

fibers intermix with the type-II fibers seen in the articular cartilage thus contributing to the continuity between the labral and cartilaginous surfaces [80]. Mechanically speaking, the labrum plays a large role in maintaining joint integrity. By extending the acetabular surface by up to 27%, the labrum is able to further encapsulate the femoral head, cushion the interaction between femoral neck and pelvis, and help maintain the joint synovial fluid for proper lubrication [82]. The combination of both collagen fibers and proteoglycans allow for the labrum to effectively perform these functions [43].

2.2.4 Muscles

Muscles are the primary means of physical movement in the body. Force generation in these soft tissues is done through various mechanisms on a cellular level involving concentration gradients of several ions such as calcium, sodium and potassium causing many slight and rapid shifting of muscle cells [83]. As a result, all muscle activity provides a slight electrical signal called electromyography (EMG) [84]. This signal provides information regarding the amount or degree of muscle activation but does not directly relate to the force output magnitude [85]. Muscle force output is dependent upon the number of muscle cells being activated, providing stabile, smooth motion with the potential for a variation in force output. The central nervous system (CNS) provides the ability to monitor and coordinate body segments within space providing a feedback mechanism for determining the amount of force to output dependent upon the desired task [84, 86, 87]. This phenomenon is most commonly referred to as coordination or proprioception and can vary between people.

Motion involving the lower extremity requires the coordination of several muscle groups. With the hip joint having six degrees of freedom for movement, it is important for control in each direction to maintain stability. Muscles are grouped according to their function and attachment sites (Table 2.2-1) [63]. The most commonly known muscle groups in reference to hip control are the quadriceps, hamstrings and glutes. Each of these contain several individual muscle bodies that work synergistically to promote motion about an axis. A single

muscle can have multiple tasks such as hip extension and external rotation seen in the gluteus maximus muscle. STS transfer primarily involves the aforementioned muscle groups as each of them have their primary function in hip flexion/extension or knee flexion/extension [88].

The three vasti muscles originate on the proximal portion of the femoral shaft and span longitudinally the length of the femur attaching on the patella via the quadriceps tendon. Similarly, the rectus femoral spans the length of the femur, attaching to the quadriceps tendon. It, however, originates on the anterior inferior iliac spine (AIIS) of the pelvis. Together, these muscles form the quadriceps group and promote knee extension. On the posterior side of the femur, the biceps femoris, semitendinosus and semimembranosus of the hamstring group each originate on the ischial tuberosity of the pelvis and attach distally just below the knee on the tibia or fibula. Together, these antagonize the quadriceps by causing knee flexion as well as some hip extension. Lastly, the gluteus maximus originates on the iliac crest and sacrum and wraps around posteriorly attaching on the gluteal tuberosity and on the iliotibial (IT) band. It produces primarily hip extension.

Muscle Name	Hip Motion	Attachment Sites
Adductor brevis	Flex, Add	Inferior ramus of the pubis, Linea aspera
Adductor longus	Flex, Add	Anterior pubis, Middle of linea aspera
Adductor magnus	Flex, ER, Ext	Edge of pubic crest, Linea aspera
*Biceps femoris - long head)	Ext, ER	Ischial tuberosity, Head of the fibula
*Biceps femoris - short head)	Ext, ER	Lower half of the linea aspera, Head of the fibula
*Gluteus maximus	Ext, ER, Abd	Lower posterior iliac crest and posterior surface of the sacrum, Gluteal tuberosity and Iliotibial (IT) band
Gluteus medius	Abd, IR, ER	Outer surface of the ilium, Greater trochanter
Gluteus minimus	Abd, IR, Flex	Outer surface of the ilium, Greater trochanter
Gracilis	Flex, Add, IR	Pubic crest, Medial condyle of the tibia
Iliacus	Flex	Iliac fossa, Lesser trochanter
Pectineus	Flex, Add	Pubic crest, Inferior to the linea aspera
Psoas major	Flex	Lumbar and thoracic vertebral bodies, Lesser trochanter
*Rectus femoris	Flex	Anterior-inferior iliac spine (AIIS), Patella
Sartorius	Flex, Abd	Anterior-superior iliac spine (ASIS), Anterior-medial condyle of the tibia
Semimembranosus	Ext, IR	Ischial tuberosity, Medial surface of the proximal tibia
Semitendinosus	Ext, IR	Ischial tuberosity, Medial surface of the proximal tibia
Tensor Fascia Latae (TFL)	Flex, Abd, IR	Iliac crest, Iliotibial (IT) band

Table 2.2-1: Lower extremity muscles involved in hip motion and their functions and attachment sites [61]. The vasti muscles only contribute to knee motion and thus are not included in this chart. They were however included in the model. (Refer to Figure 2.1-3, Figure 2.1-4 and Figure 2.1-5 for insertion sites)

Abbreviations: Flex – flexion, Ext – extension, Add – adduction, Abd – abduction, IR – Internal Rotation, ER – External Rotation.
*Muscles included in the model

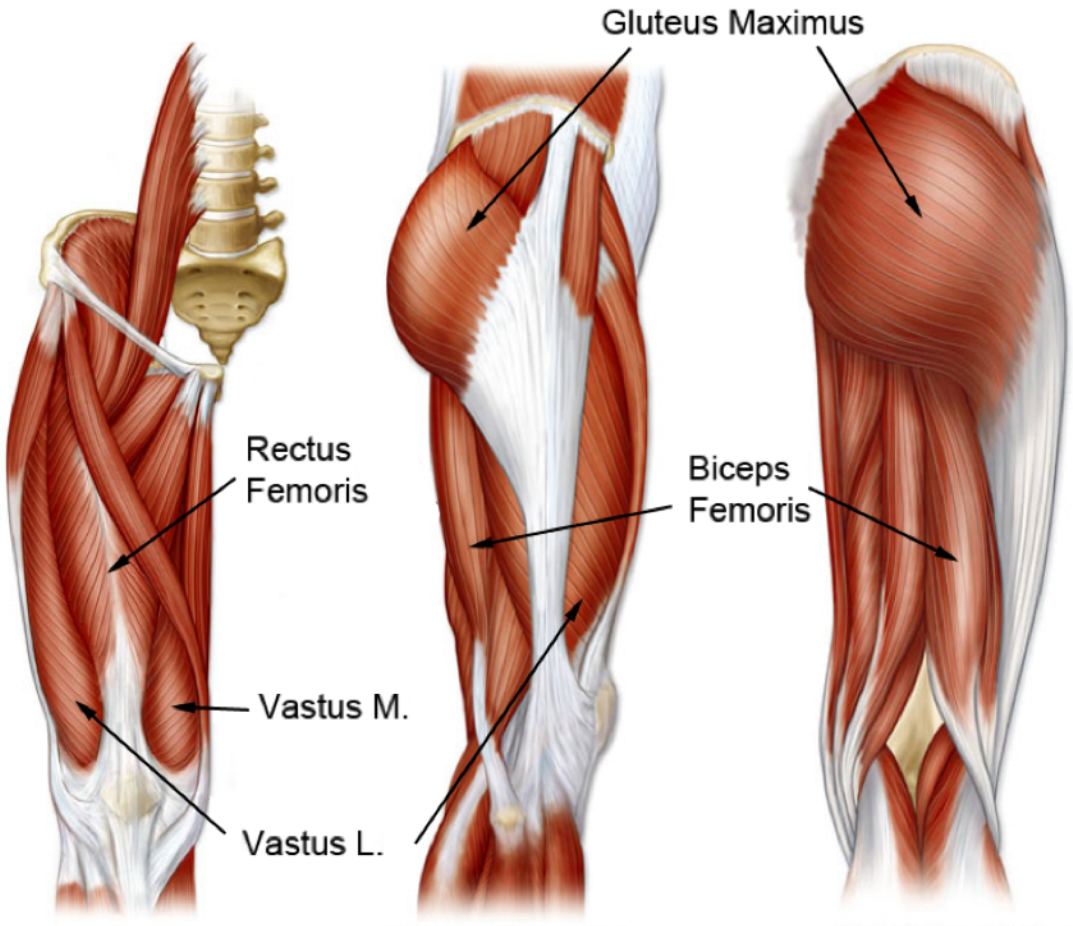

Figure 2.2-4: Anterior, lateral and posterior views of the lower extremity muscles. The muscle included in this model are highlighted.

Chapter 3: Development and Validation of a Sit-to-Stand Computational Model

3.1 Introduction

Creation of this rigid body model involved a series of steps to take a patient's computerized tomography (CT) scan and develop a fully functional series of solid bodies and force vectors representing the necessary skeletal and soft tissue structures. Accuracy with regards to true anatomy and function was considered throughout the development process. Skeletal anatomy for the hip joint is rather simple relative to other joints modelled in our laboratory, with the only skeletal structures being the femur and pelvis [63]. However, the motion and tissue structures involved are rather complex.

All lower extremity bones proximal to the ankle were included in the model to allow for the desired sit-to-stand motion and a more accurate representation of muscle insertion sites. CT scans provide accurate representation of this skeletal anatomy but do not provide much information as to the surrounding soft tissue structures. Consequently, literature-reported insertion sites were used to construct the force vectors necessary for muscles and ligament structures. Essentially, a combination of the specific skeletal anatomy and the applied forces were used in developing this model. With the ultimate goal of this work being to provide a general means for studying how different conditions affect sit-to-stand transfer, there was not a need for complete patient specificity during the development of this model.

3.2 Methods

3.2.1 Body Creation and SolidWorks Implementation

To accurately generate the necessary skeletal geometry, a CT scan of a single patient (female, 58 years old) was imported into a commercially available software package known as Mimics. This scan included the entirety of the patient's lower extremity, along with some of the lower abdomen, and was taken for the purpose of a non-musculoskeletal issue. There were not any reported signs or symptoms of hip joint disorders present in this patient.

Mimics is capable of transforming DICOM (Digital Imaging and Communications in Medicine) files, consisting of an array of 2D images generated during the CT scan in three planes, into a 3D body usable in computational modeling. Mimics allows for the scan to be visualized slice-by-slice in each plane with an additional 3D view of the already segmented bodies. More importantly, Mimics allows for the user to highlight or select desired tissues from within the scans on each slice. These CT scans provide an inherent visual contrast due to the variation in radiodensity between hard and soft tissues, making the process of selecting desired tissues much more straight forward. A thresholding tool within the software highlights areas within each slice based on this contrast allowing the user to filter out various types of tissue to simplify this selection. Herein, a mask was created, overlaying the tissue of choice, where the boundary was determined by a sharp change in contrast or radiodensity and was marked through polylines.

For this particular model, focus was on the long bones of the lower extremity including the femur, pelvis, sacrum, tibia, fibula and patella. The above process was done on each image slice for each tissue to provide a 3D visual of the tissue. A combination of user input along with automation made this task less daunting. Moving forward, Mimics then utilized interpolation functions to combine these 2D masks and polylines from all three planes into a full 3D shell representing the tissue. This shell contained highlighted voxels, or 3D

representations of the 2D pixels, which fill the tissue shape. Differentiation between cortical and trabecular bone was not considered in extracting skeletal tissues as RBM excludes deformation. The entirety of the bones was filled, forming a full solid body (Figure 3.2-1). Before proceeding, the body was checked as to its visual accuracy and refinements were made.

Figure 3.2-1: Mimics interface showing the progression from scan (left) to mask creation (center) and finally 3D body generation (right) for a right femur.

The 3D shell was converted into a series of facets, or planes and vertices, which could be read by various CAD programs for further use. This is a process known as meshing and it provides a 3D body representative of the desired tissue in a simplified manor. Each of the facets are typically triangular or polygonal in shape and can number in the thousands to millions for a single body, largely depending on the curvature of the surface. It is preferred that this number remain below around 20,000 for use in SolidWorks to reduce computational power needed. The meshed body was further refined within a Mimics add-on called 3-Matic through a process called remeshing, which reduces the number of faces along with smoothing out some irregularities. During this process, it was important to maintain the correct anatomical shape but to still provide an appropriately simplified mesh for computational purposes (Figure 3.2-2). With the goal of having this model be reliant upon articulation, it was important to include this process and provide smooth and accurate surfaces for each of the bones. The final product was saved as a stereolithographic (STL) file for use later. STL files describe the surface geometry of a particular object via points and unit-normal of the faces in a 3D Cartesian workspace. For the meshed product, the STL file type easily encompassed the geometry in an efficient and minimal manner. Each of the aforementioned target bones of the lower extremity were saved as an individual STL files for future use.

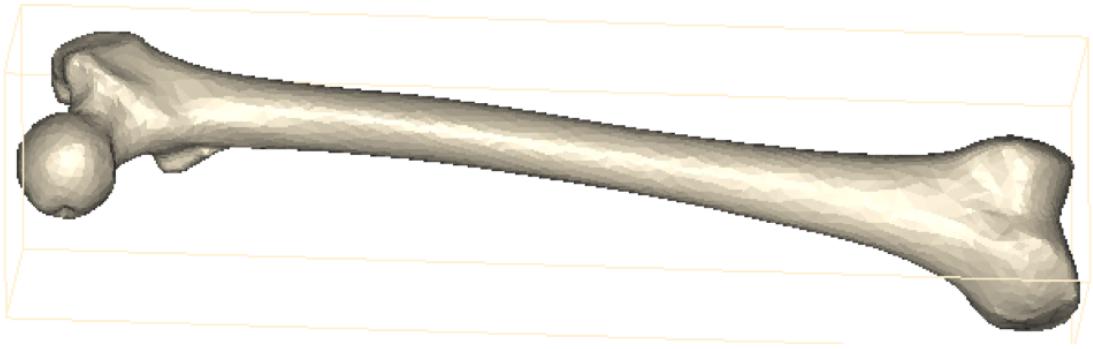

Figure 3.2-2: This is a result of the remeshing and refining done within 3-Matic on the femur used for this model. The native structure and shape were preserved while minimizing the number of faceted surfaces and smoothing out rough areas.

SolidWorks 2016 was the primary software used for simulating musculoskeletal kinematics and stress analysis. It is a multifaceted 3D CAD program that allows for engineering design and testing of that design to be performed within a single user interface. Within the program, a user can design solid or surface bodies, known as parts, and combine them into larger assemblies for analysis. For this work, the parts were imported via the bone STL files previously mentioned, rather than being manually created, allowing for an accurate representation of each bone. SolidWorks is capable of reading a STL file to create a single solid body based upon the points and faces structure. After some elementary rendering the bones of were successfully brought into the SolidWorks interface, with each saved as an individual SolidWorks part (Figure 3.2-3). Providing unique colors allowed for easier distinguishing between structures during the development phase.

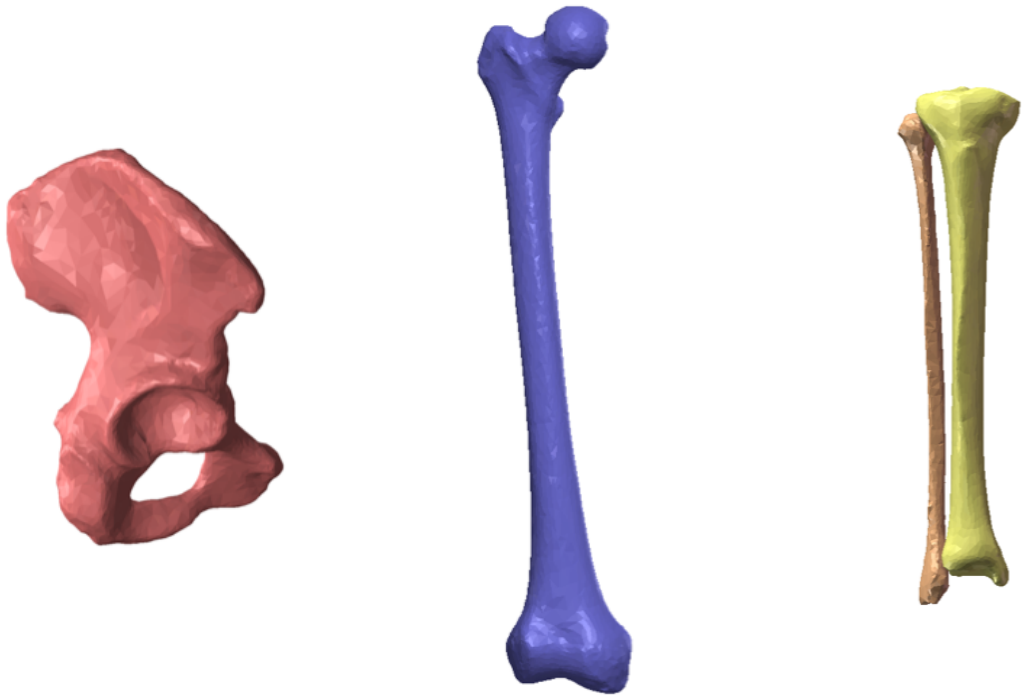

Figure 3.2-3: Images showing how bones look after being imported into the SolidWorks workspace. (Left) Lateral view of the right hemi-pelvis, (Center) anterior view of the right femur and (Right) anterior view of the right tibia and fibula.

3.2.2 SolidWorks Assembly and Part Arrangement

SolidWorks contains separate add-in packages capable of performing different analyses such as a Finite Element Analysis simulation as well as a Rigid Body Motion kinematic solver with the latter being used for the work in this thesis. As mentioned previously, each bone was saved as its own separate part file upon being imported into SolidWorks. For them to be useful in a Motion study, they needed to all be individually opened and appropriately arranged within a single SolidWorks assembly. From the assembly workspace, parts can be arranged relative to each other and different boundary conditions applied. The bones were initially arranged according to their original scan orientation by matching, or mating, their origins together. However, this does not guarantee alignment in a true neutral position.

The International Society of Biomechanics (ISB) created a means for defining the true anatomical coordinate system within each bone allowing for each to be placed in their anatomical position (Figure 3.2-4) [89]. ISB utilized prominent bony features or landmarks to define the universal anatomical coordinate system on a local scale within each individual bone. Using this, each bone was aligned with a consistent universal coordinate system based upon their individual axes wherein the assembly as a whole could be easily manipulated into the desired position for testing. A combination of geometric fitting and manual selection was used on each part to fully implement this coordinate system. Spherical fitting on both the femoral head and acetabular surface permitted an estimation of the center of rotation for each structure with regards to hip motion (Figure 3.2-5, Figure 3.2-7). Peak fitting for different regions was used to find the locations of the epicondyles along with the iliac spines. According to ISB, the centers of rotation become the origin for the respective parts while the epicondyles and iliac spines provide additional points to define the anatomical planes (Figure 3.2-6, Figure 3.2-7).

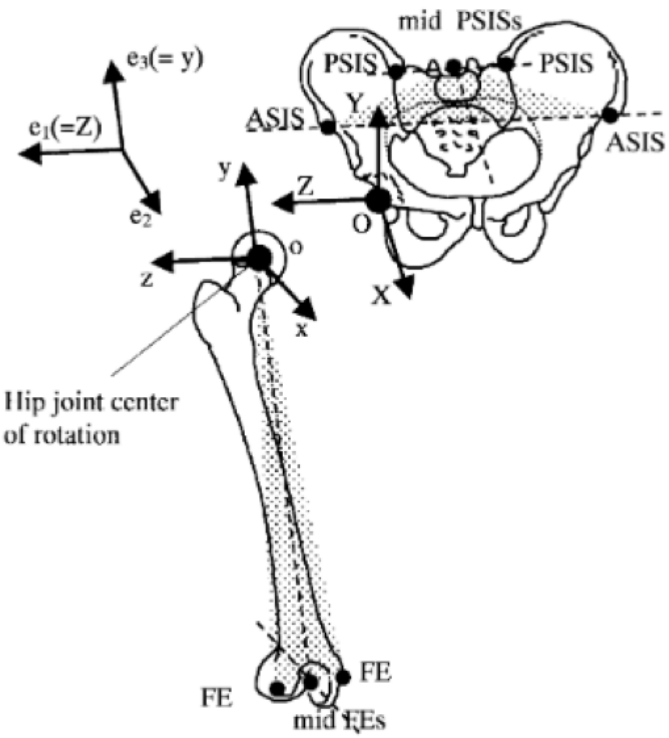

Figure 3.2-4: ISB used various common anatomical landmarks within the bones to define a coordinate system for aligning each bone relative to each other. Both the femur and the pelvis have a local set of axes with the origin centered on the point of rotation for the hip joint [89]

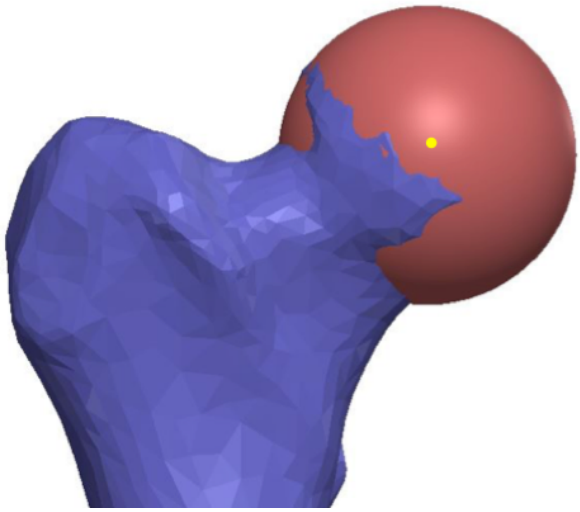

Figure 3.2-5: An anterior view of the proximal femur (blue) with spherical fitting on the head (red) to determine an approximate center of rotation. This center of rotation was then used as the coordinate system origin.

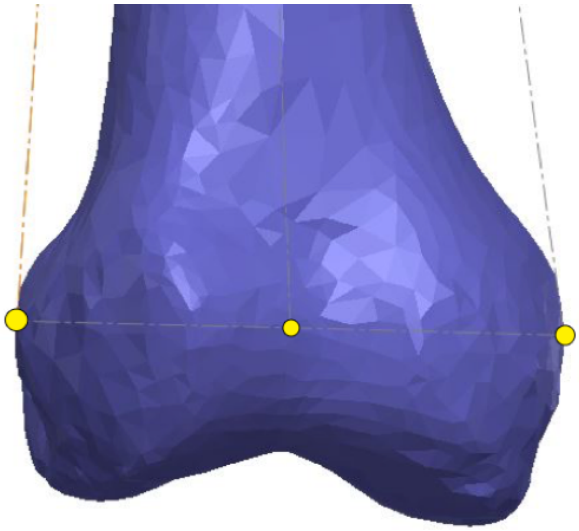

Figure 3.2-6: An anterior view of the distal femur showing that selection of the epicondyles was done though the most lateral and most medial points in the distal femur. These points were used in defining the frontal plane of the knee.

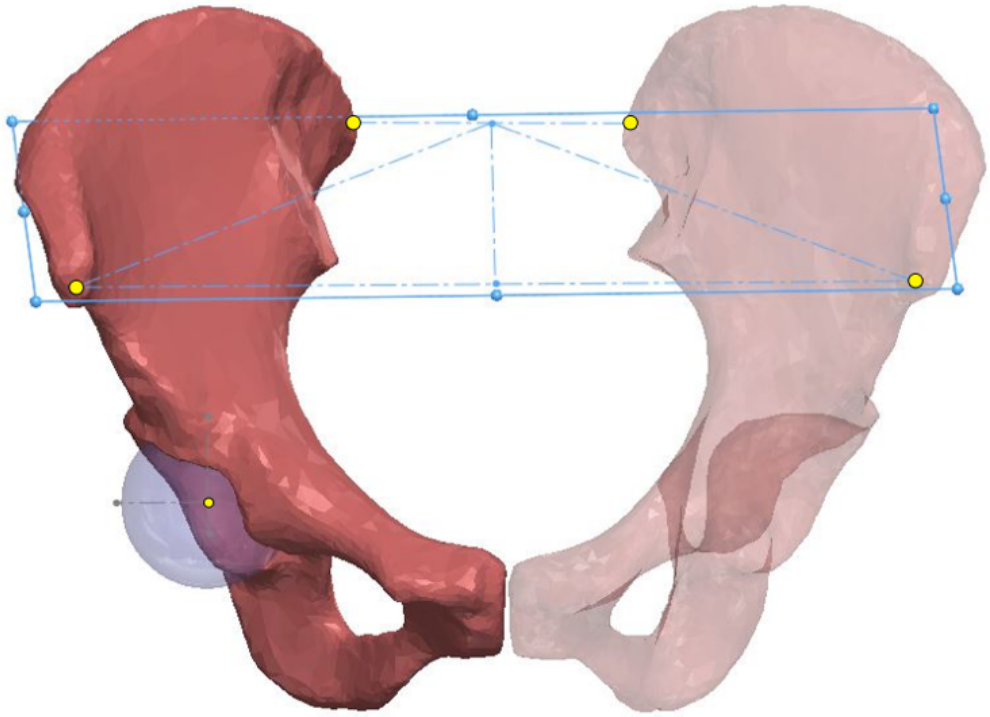

Figure 3.2-7: An anterior view of the entire pelvis with spherical fitting on the acetabulum and a plane defined by locations of the PSIS and ASIS points. Both of these geometric fitting techniques were used in defining the coordinate system according ISB.

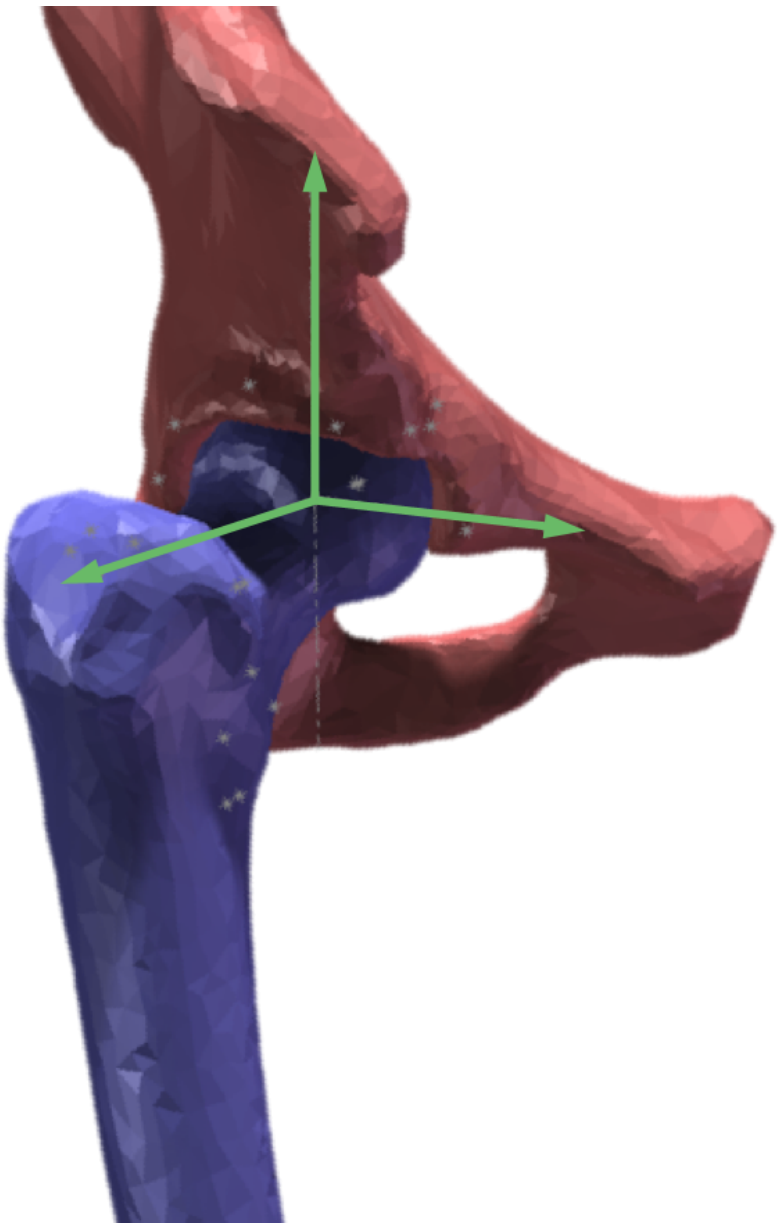

Figure 3.2-8: Anterolateral view of how the femur and pelvis were correctly aligned with each other according to the ISB-defined anatomical coordinate system. The green arrows show the 3-dimensional coordinate system.

With the bones correctly aligned according to this coordinate system, each joint was manipulated based on their approximated points or axes of rotation to arrange the entire model in a seated position [90]. There is not a single defined 'seated position' but rather an

ambiguity based upon personal preference. A starting position for rising out of a chair with 100° of knee flexion, slight hip abduction, a vertical pelvis and a 20° posterior tilt of the tibia/fibula was chosen as the initial seated position for this study based on the kinematics reported by Burnfield et al (Figure 3.2-9) [91]. To mimic the upper body center of mass (COM), an extension of the spine was created up to a point calculated as the COM based upon anthropometric data provided by NASA [92]. From here a force vector was applied in the negative vertical direction as a means for providing an estimation of the contribution of the upper body weight. Total body weight was set to be $75\,kg$ ($\sim 165\,lbs$) and, based upon anthropometric data, upper body weight comprises 59.28% of this total body weight [92]. As this model only incorporates a unilateral situation, this amount was further cut in half to represent weight experienced by a single lower limb. An additional vector representing forces generated through the torso along with two stabilizing dampers were attached to this COM point as well. Magnitudes for the torso force were calculated retrospectively based upon the expected moment about the hip joint and the moments generated by each of the current applied muscles [93]. Ambiguity about this particular force provided an opportunity for some adjustment to during the validation phase. The stabilizing dampers provided the ability to control the rate of motion and prevented abrupt movement. These were assigned a damping coefficient of $0.5\,kg \cdot s^{-1}$ permitting a level of smoothing and stability without drastically altering the results.

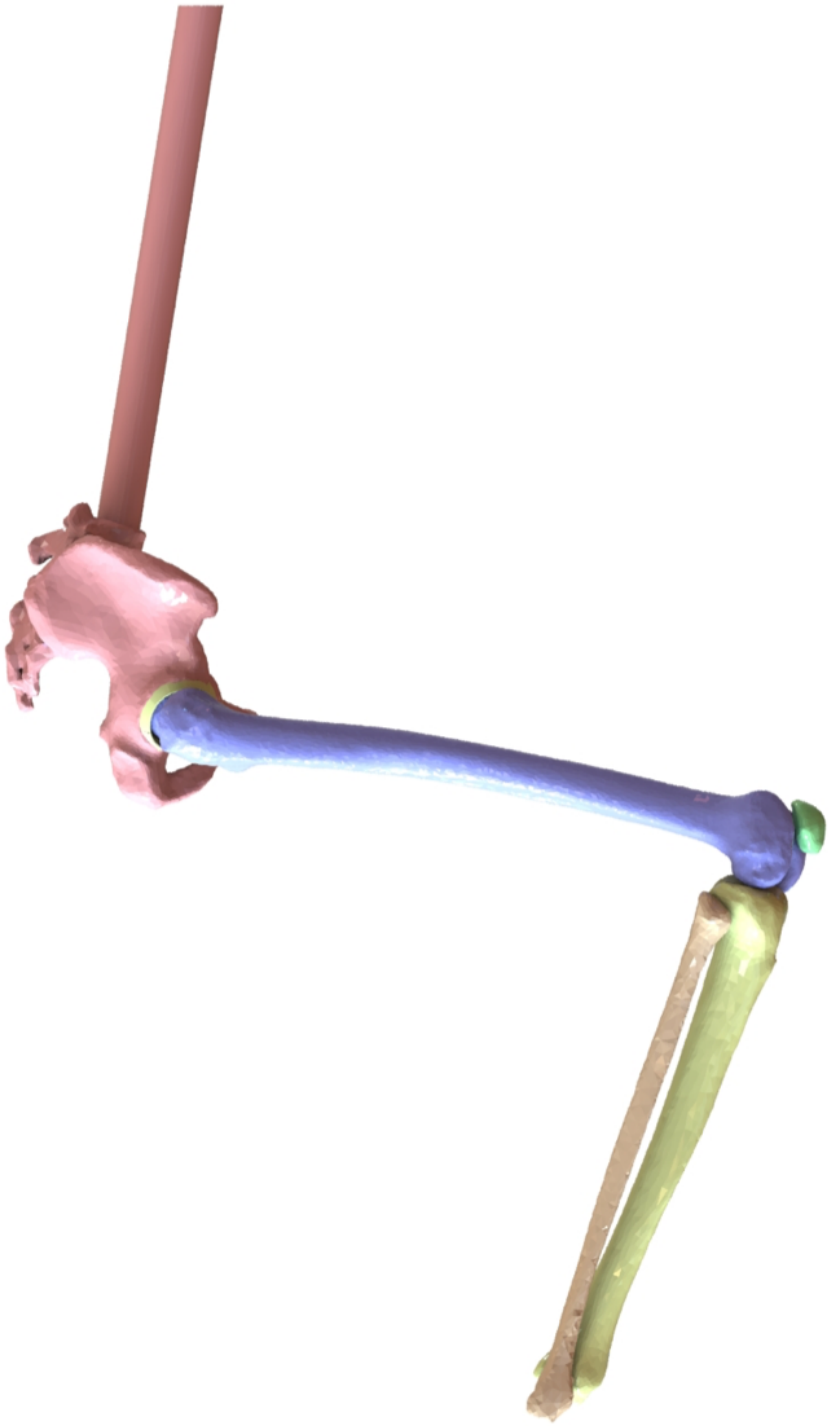

Figure 3.2-9: A lateral view of the skeletal structures positioned in the initial seated position. The hemi-pelvis and physical representation of the torso COM (red), the femur (blue), tibia (yellow), fibula (orange) and patella (green) can all be seen. Soft tissue structures were hidden for clarity.

3.2.3 SolidWorks Motion and Soft Tissue Implementation

With this anatomically correct lower extremity model appropriately arranged in a seated position, the aforementioned SolidWorks Motion package was used to implement contact and penetration interactions between bones, restraints provided by ligaments, forces emulating muscles and weights, and fixtures set to allow/prevent the bones to translate and/or rotate with respect to one another. The fixtures were important in creating a basis or reference for all other parts and preventing the entire assembly from freely moving in space. As the focus of this work was on the hip the knee was simplified to be a simple hinge and the tibia and fibula were both fixed in their initial position. This allowed for the femur, pelvis and even patella to still move relative to the tibia/fibula while simplifying the necessary soft tissue structures and preventing uncontrolled motion in space. It also removes the ability to incorporate ankle joint into the model, an aspect that should be considered moving forward.

Motion of the hip joint was completely governed by the 3D articular anatomy, ligamentous restraints, and muscle activation. Contact between the articular surfaces was defined such that penetration between parts was minimized. SolidWorks Motion provides the ability to apply penetration and contact settings between two different parts based upon a stiffness value, maximum damping and penetration at this maximum damping. Utilizing the ADAMS solver and these predefined parameters, SolidWorks recognizes regions of overlap between two parts and applies a force projecting outward on both parts. This force is applied at the centroid of the overlap region and the magnitude is calculated as the product of the stiffness and overlap depth. A viscous element is included to prevent destabilization and is dependent on the maximum damping input parameter and the rate of interference between the two parts. Any parts that should not overlap one another were applied appropriate contact parameters for minimal overlap between bodies while preventing unnecessary penetration forces (Table 3.2-1). Lastly, friction was ignored between parts as synovial joints experience negligible friction coefficients [94, 95].

Parameter	**Value**
Geometric Accuracy	100%
Contact Type .	Impact
Stiffness (k)	8000 N/mm
Exponent (e)	2
Maximum Damping (c_{max})	400 $N \cdot s/mm$
Penetration at Max Damping (d_{max})	0.001 mm
Friction	None

Table 3.2-1: Contact parameters used to prevent penetration between bodies in SolidWorks Motion.

Soft tissue structures were represented through a series of force vectors with the number of vectors varying dependent upon size and shape. For the more complex structures such as the hip capsule, a larger number of force vectors were linked together to represent the intricate shape of these ligaments. Both the fiber orientation and mechanical properties were considered in aligning and connecting these force vectors. These properties were gathered from a combination of cadaveric experimental studies and anatomic textbooks to most accurately replication the shape and behavior of the native tissue [96, 97]. SolidWorks allows for force vectors to be programmed through a simple FORTRAN expression allowing for conditional behavior to be implemented (Equation 3.1). Ligaments were given tension-only behavior based on an initial-length and a stiffness value (Table 3.2-2) to determine the magnitude and thus providing them with the ability to react to the environment.

Ligament	**Force Vector**	**L_0 (mm)**	**Stiffness (N/mm)**
Superior ILFL	1	23.7504	48.9
	2	13.3824	97.8
	3	16.9536	97.8
Inferior ILFL	1	23.3664	100.7
	2	29.9328	100.7
	3	24.1152	151.05
	4	23.0112	151.05
	5	29.1168	151.05
PFL	1	28.656	35.82
	2	21.744	35.82
	3	21.5616	68.565
	4	17.3472	68.565
	5	19.45928	68.565
ISFL	1	12.6144	100.7
	2	11.9328	100.7
	3	20.5536	151.05
	4	17.9136	151.05
	5	26.592	151.05
	6	21.8592	151.05

Table 3.2-2: The parameters used for each individual force vector that comprise the hip capsular ligaments. Initial length values were based upon in-situ strain in the defined femur resting position relative to the pelvis and stiffness values were gathered from previous studies and adjusted depending on the number of vectors used to define the ligament [12].

$$F = IF(\{Length\} - L_0 : 0, 0, -S \cdot (\{Length\} - L_0)) \tag{3.1}$$

In the previous expression, $\{Length\}$ refers to the distance between attachment points of the force throughout the simulation time and was constantly compared to an initial length (L_0) for each tissue. This initial length was defined based upon an in-situ strain of 0.04 with the joint in a resting position. In this case, the resting position for the hip joint capsular ligaments is 30 degrees of flexion and abduction with a slight internal rotation [41, 98]. S represents the stiffness parameter with each ligament applied a specific stiffness value. The expression itself is a simple if-statement written in FORTRAN code wherein measured length and resting length were compared with zero on each iterative calculation and a force proportional to the stiffness and strain value was generated if that difference was greater than zero. Essentially, the force vector was only activated when the measured length was greater than L_0, maintaining the tension only specification.

Rather than being reactive to the motion of the surrounding parts, muscles are the driving force behind the motion. Muscle activity was defined based on EMG activity from an experimental study performed by Burnfield et al while the force magnitudes were determined through an inverse dynamics computational study done by Caruthers et al [45, 91]. All insertion sites and physiological lines-of-action were determined primarily through anatomic textbooks [63]. Simple, linear muscles were modeled with point-to-point linear force vectors connecting these insertion sites and representing the desired line-of-action. The ingenuity, however, came in matching the curved and complex shapes for these tissues within the model to what is seen anatomically. Muscles with more non-linear shapes and curvatures that wrap around joints, such as the gluteus maximus, have yet to be successfully modelled without greatly increasing the necessary computational power or the need to make significant compromises. With only simple, linear forces available in SolidWorks Motion, this has been a lingering issue with RBM applied to the organic shapes seen in orthopedic biomechanics. An approach involving the connection of linear forces along a predefined path was used as the solution for this model. A small sphere, or bead as we called it, served to both connect the

force vectors as well providing a physical barrier permitting the forces to follow any defined path. In the case of this research, simple cylindrical shapes were used as the paths and were created based upon the shape of the desired tissue (Figure 3.2-10, Figure 3.2-11). Previous work has utilized this technique without the defined path, limiting each bead only through contact between it and the surrounding solid bodies consequently adding to the required calculations and thus lengthening the time required [99]. By providing a surface path for the beads to follow and using mating techniques rather than contact properties, a higher degree of control and lower amount of calculations necessary were achieved. The gluteus maximus along with the hip joint capsule ligaments were modelled in this manner.

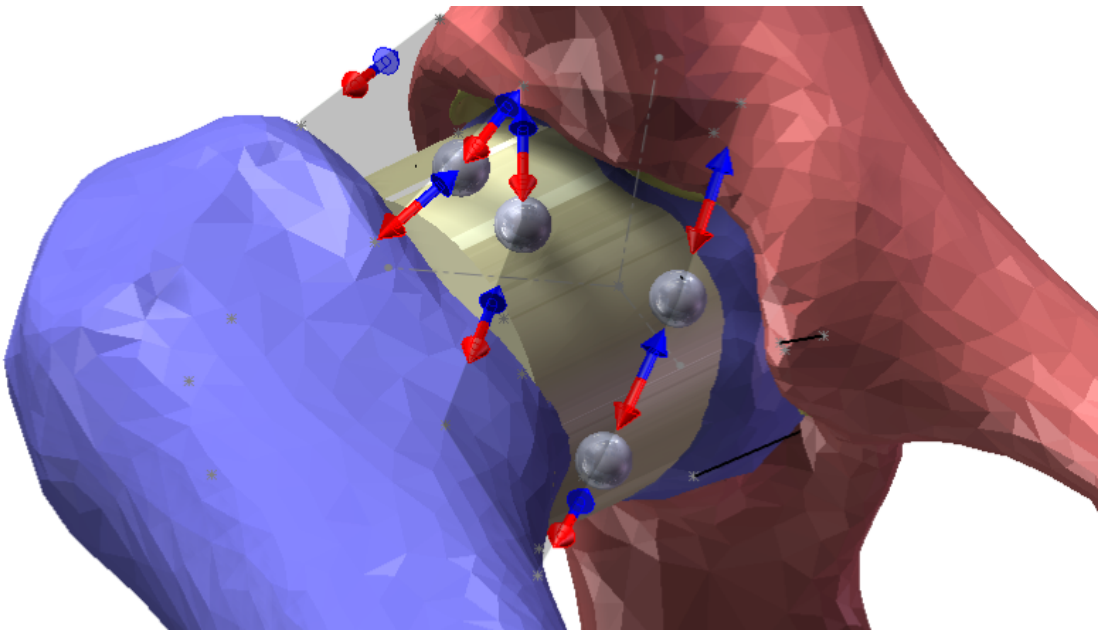

Figure 3.2-10: An example of how the Iliofemoral Ligament was created using several linear force vectors and spheres. The red and blue arrows denote the individual force vectors. Each sphere is set to glide along the yellow cylinder which was generated based upon the shape and orientation of the femoral neck.

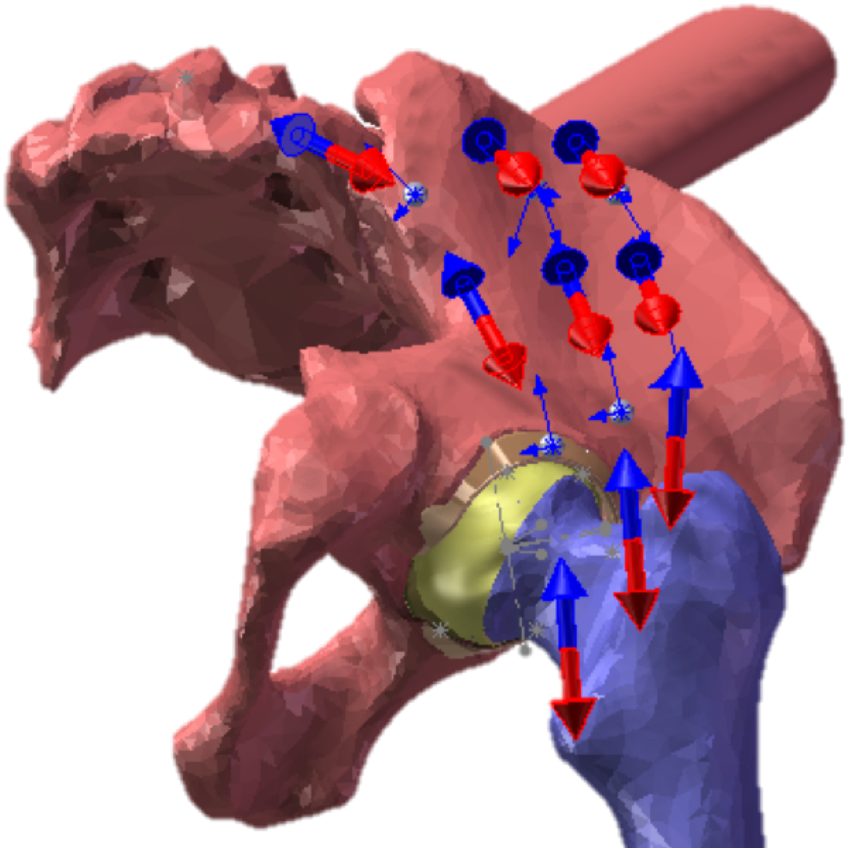

Figure 3.2-11: An inferolateral view of the hip joint portion of the model with the gluteus maximus highlighted. The red and blue arrows represent the gluteus maximum muscle with six silver beads connecting these nine force vectors.

Each force vector was run in parallel with a damper for tissues modeled using this technique. This was exceptionally important in maintaining stability and preventing the beads from scattering and losing effectiveness for that particular tissue (Figure 3.2-12). With the dampers and applied path, each set of forces successfully followed the correct line of action for that particular tissue without much deviation. However, inclusion of dampers provided a viscous element and, in order to prevent the dampers from altering the actual motion, the dampers were provided with a small coefficient of $0.1\,kg \cdot s^{-1}$. This value was low enough to not compromise the kinematics while still successfully stabilizing the bead motion.

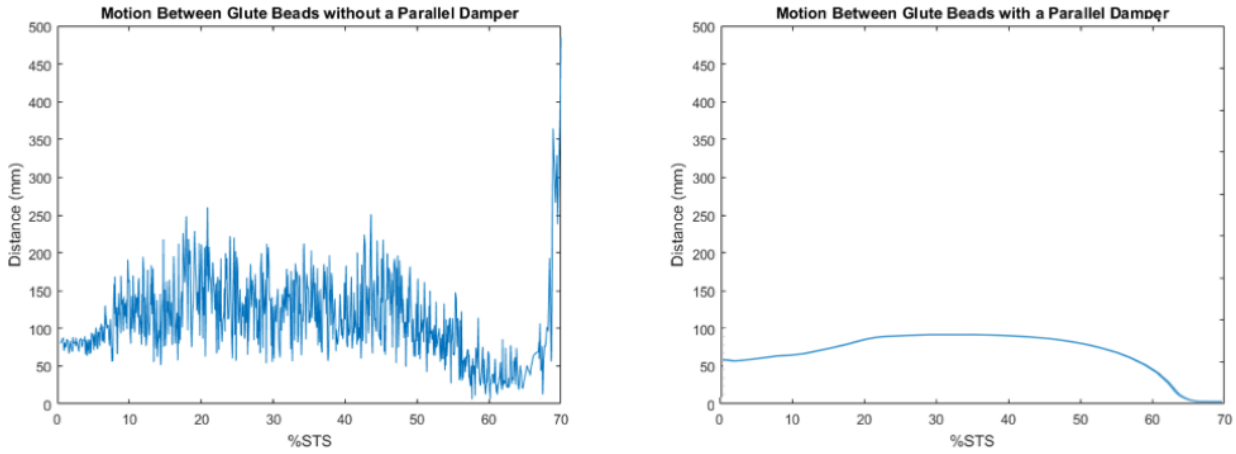

Figure 3.2-12: Plots comparing the linear distance between gluteus maximus beads with and without a parallel damper. (Left) Motion without the damper is much less stable and has a higher maximum distance between beads. (Right) The damper smoothed the motion reducing the random fluctuations.

The remaining soft tissue structures included in the model are the labrum and articular cartilage, both of which contain unique properties difficult to completely incorporate within a rigid body framework. These differ from the previous soft tissues in that neither runs linearly from one insertion site to another. Rather, they both cover an area acting as an additional layer over the skeletal anatomy. Additionally, both experience a great deal of compression which cannot be modeled, even in a simplified manor, with rigid body motion. Cartilage was kept as a simple rigid structure created as an approximately 1 mm extension of the lunate surface of the acetabulum. Femoral cartilage was not included in the model as it caused complications during the analysis. The labrum was modeled in a manner allowing for its tension properties but mostly ignoring its compressive properties. It was separated into 5 different sections with tension-only force elements connecting adjacent elements (Figure 3.2-13). Each force vector was programmed in a similar manor as the ligament structures with the stiffness value gathered from literature but with an initial length of zero. The rigid elements were attached to the acetabular rim via hinges essentially creating a series of flaps with tension force vectors maintaining its shape. Five elements were chosen as a compromise between over-simplification and stability.

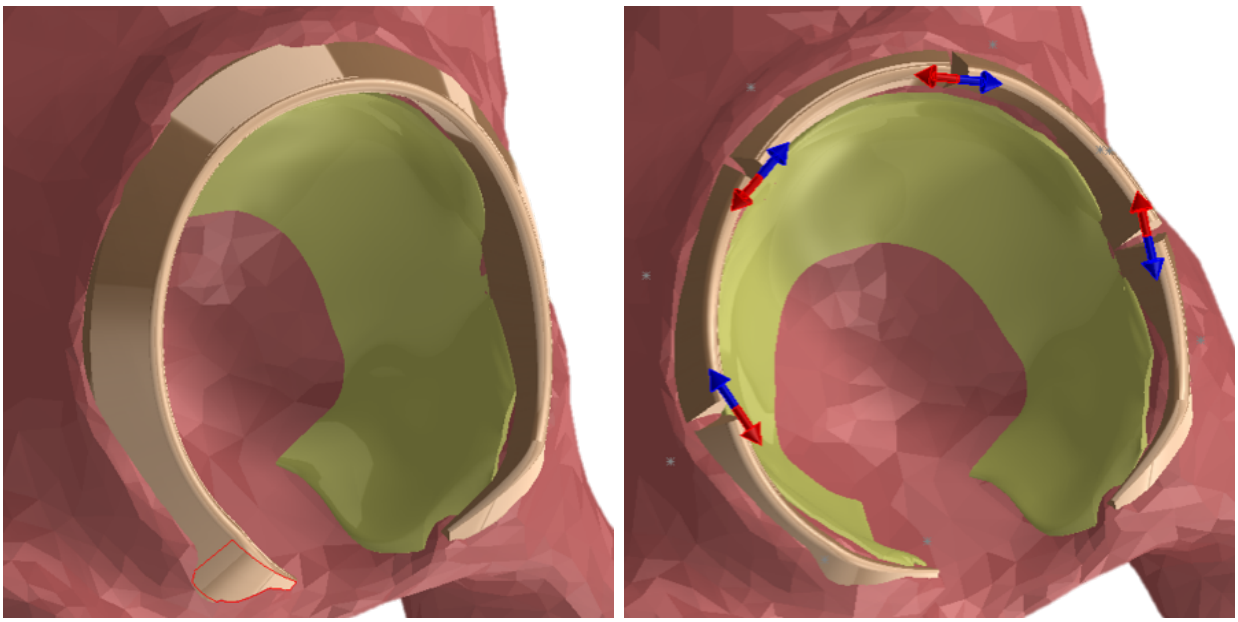

Figure 3.2-13: (Left) The labrum is shown in orange fully intact without any displacement. (Right) The labrum in orange in a displaced state with the force vectors shown between adjacent elements. Both images depict the acetabular cartilage surface (yellow).

3.2.4 Modeling Sit-to-Stand Transfer

The sit-to-stand (STS) transfer is a maneuver performed approximately 60 times per day by a healthy individual regardless of their demographics [47]. It is commonly overlooked as a trivial task but can become rather difficult for those with lower extremity musculoskeletal disorders (MSDs) or even neurological disorders such as Parkinson's disease [100]. These situations can lead to increased incidence of contact between tissues, lowered muscle force output, reduced coordination and general discomfort throughout the motion typically as a result of the high degree of hip flexion experienced during STS. Clinically, STS is commonly used as an indicator of performance during recovery for elderly patients. The entire process involves coordination between many of the lower extremity and torso muscles as well as a large force magnitude. During the initial 40-45% of motion, the body repositions itself to

provide a more ideal moment generated by its weight about the knee joint and thus requiring less muscle force. This is referred to as the pelvic tilt phase. As the torso COM position in space is fixed relative to the pelvis for this model, motion in this phase was entirely based around the hip joint. Immediately following this phase, the actual lift-off to a standing position takes place comprising the remaining 55-60% of motion and involves significantly higher force magnitudes. Modeling this biphasic behavior directly came from the muscle force programming mentioned previously. Both the magnitude and the activation/deactivation timing were accurately represented when developing this model. The combination of EMG activation and inverse dynamics force data provided a great starting point for providing these muscle force vectors with appropriate magnitudes over time. An example of the gluteus maximus force-time plot can be seen below (Figure 3.2-14). Muscles contain negative force values to represent the compression force native to muscle contractile behavior. Subsequent iterations of the model changed the peak magnitudes, within 1 standard deviation as reported (Table 3.2-3).

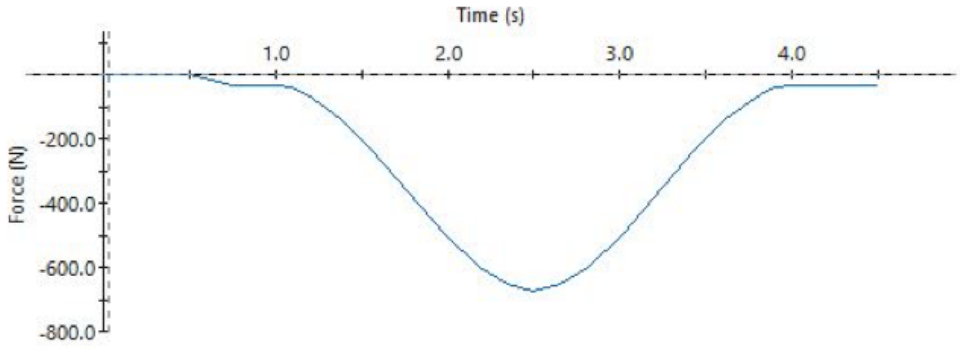

Figure 3.2-14: An example of a force-time plot representing the activation pattern for the glutes maximus muscle. This figure comes directly from the SolidWorks workspace.

Muscle	Peak Force Magnitude (N)
Gluteus maximus	2009.07 ± 277.31
Vastus lateralis	1542.14 ± 359.30
Rectus femoris	944.03 ± 382.21
Vastus medialis	798.88 ± 296.41
Bicep femoris	490.06 ± 380.64

Table 3.2-3: Peak muscle force magnitudes for each of the muscles used to drive this model. This data came from an inverse dynamic calculation based on kinematic data from 7 healthy patients [45].

3.2.5 Model Validation

Validation of this computational model was necessary to ensure that it was an accurate representation of what is seen in the real world. Proper validation fortifies the claims made as a result of future studies performed using the model. In this particular case, kinematics throughout a sit-to-stand transfer was the primary concern and thus should be compliant with the real-world motion. The hip joint was being focused on for this work but both the knee and hip are involved in performing a sit to stand transfer and thus both were properly validated. Since the appropriate equipment for performing an experimental version of this task was not accessible, an indirect means of validation was performed with data gathered from previously published work. Burnfield et al (2012) investigated how the Vera-lift sit-to-stand device affected the motion through a STS transfer [91]. Ten male adult patients with no previous history of musculoskeletal or neuromuscular impairment were recruited to perform this study. Data was gathered using the Qualisys Motion Analysis System, a series of reflective markers and EMG electrodes along the primary muscle groups. Each participant was instructed to perform the STS task without any device, while using the device and still utilizing personal strength, and then finally with complete reliance upon the device. Kinematic and electromyography data were gathered from each case and the

ensemble averages were reported. For the purpose of this thesis, only trials without any device were considered.

In comparing the model with experimental data, the timescale for the motion needed to be scaled appropriately. STS is typically reported with respect to a percentage of the motion, rather than actual time, ranging from 0% at the initiation of the pelvic tilt phase to 100% at a fully standing position. As the muscles drive the motion and were used as the input parameters of this model, the timing arrangement of these muscles was used to scale the motion appropriately from the SolidWorks timescale to a percentage value. More specifically, according to EMG results, most muscles peaked at approximately 50% STS. This relationship provided a ratio used in converting the timescale appropriately. In this case, the success or failure of the applied forces could be monitored based on the motion for proper validation.

Gathering the knee flexion and pelvic tilt angles for the computational model was done indirectly by monitoring key positions in space during the entire process. SolidWorks provides a straightforward means for monitoring the angle between three points but is limited to only values from $0 - 180°$. Rather than continuing on to values greater than 180°, SolidWorks begins to count down back to 0°. For this reason, an approach involving length measurements with simple trigonometry calculations was used in determining the model kinematics (Figure 3.2-15). Linear distances (L_1 and L_2) in the horizontal direction were taken at each time point with respect to a point fixed in space, $1000\,mm$ (L_3) from the knee joint rotational axis. These measurements permitted an accurate calculation of the pelvic tilt (θ_{PT}) and knee flexion (θ_{KF}) angles within the physiologically possible range. Custom Matlab functions (Appendix A) were developed for the validation process. They performed the calculations in determining the resulting kinematics and then performed further analysis on the data in reference to experimental data from Burnfield et al.

As a consequence of fixing the lower leg anatomy with a 20° posterior rotation, full upright posture was unachievable with the current state of this model. At approximately 70% of the motion, knee flexion from the experimental data reaches 20° and thus this was set to be the target point for validation. Root mean square error (RMSE) was used to determine the model or models that most closely resemble the kinematics reported experimentally. RMSE provides a comparison between two data sets by quantifying the sample standard deviation between predicted and observed values [101]. A threshold RMSE of 5° was used as the limit for providing an appropriately validated model based upon the standard deviation reported by Burnfield et al for various points during the motion [91]. Any models above this threshold for both knee flexion and pelvic tilt were determiend to be considerably different from the experimental data. In selecting models that fell within this acceptable range to use for additional analyses, the points of higher deviation from the experimental work were considered. For instance, with femoroacetabular impingement we hypothesized the area of greatest bone interaction would take place during peak hip flexion and thus it was important to have a model accurately representing the transition from pelvic tilt to lift-off with a peak pelvic tilt angle within the range of reported values of $28.1 \pm 7.0°$ [91]. Finally, angular velocity was calculated as the derivative of the angular position data with respect to time for each of the models as well as the experimental data to provide additional analysis.

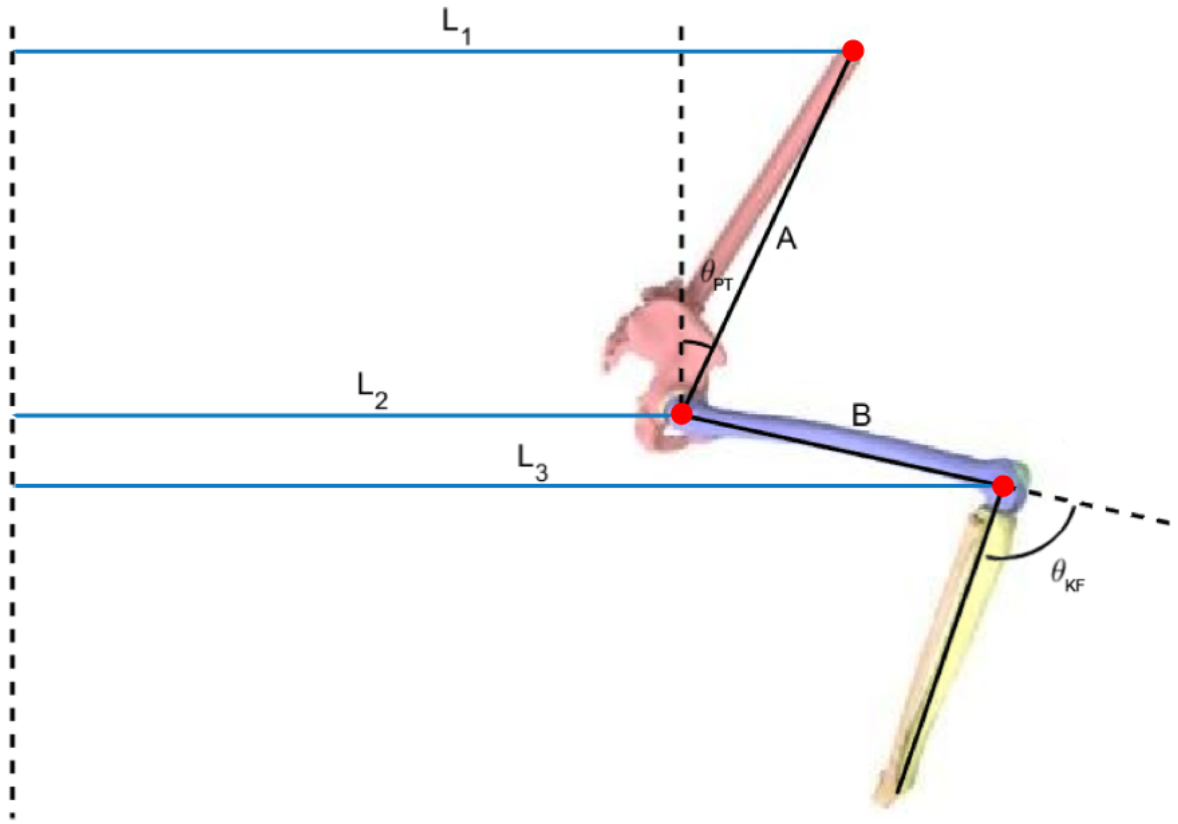

Figure 3.2-15: A visual describing how the kinematic data for both hip and knee motion were calculated throughout the motion. Refer to Equations 3.2 and 3.3 for how these variables and measurements relate to each other and are used in calculating the desired pelvic tilt (θ_{PT}) and knee flexion (θ_{KF}) angles.

$$\theta_{PT} = sin^{-1}\left(\frac{L_1 - L_2}{A}\right) \tag{3.2}$$

$$\theta_{KF} = 90 - cos^{-1}\left(\frac{L_3 - L_2}{B}\right) + 20 \tag{3.3}$$

3.3 Results

Using the RMSE threshold of 5°, this lower extremity computational model was successfully validated up to the 70% of the sit-to-stand motion target for three different variations of muscle force inputs (Table 3.3-1). Two of the models (KT226 and KT227) have nearly identical applied forces but did vary slightly in the torso force wherein the torso force for both models peaked at 85N but decreased down to 40N for KT226 and decreased down to 45N for KT227 (Figure 3.3-1). The third model differed in magnitude between all quadriceps muscles and in the torso force. All three models were used as a means of accounting for slight alterations in the STS kinematics seen between individuals. Each had advantages to the motion while none perfectly matched every aspect of the STS transfer as reported experimentally. Two (KT226 and KT227) were fully validated to the 70% target for both pelvic tilt and knee flexion with RMSE values less than 5° and the last (KT170) contained a near exact replication of the hip motion (RMSE = 1.5°) but with inadequate knee flexion (RMSE = 10.5°) (Table 3.3-2). All this information was plotted with the data from Burnfield et al for direct comparison (Figure 3.3-2). Additionally, all three models had peak pelvic tilt values well within the target range ($28.1 \pm 7.0°$) [91] (Table 3.3-3).

Each of the models performed the lift-off phase at a faster rate than what was seen experimentally. Joint velocity plots show this difference in angular velocity occurring at approximately 60% of STS motion with a spike in the negative direction for both pelvic tilt and knee flexion (Figure 3.3-4). Negative velocity refers to the magnitude of each joint angle decreasing at a higher rate. Models KT226 and KT227 show a very clear and sharp peak with model KT170 displaying only a slight increased rate of negative angular velocity towards the end of the motion. This observation was a reoccurring issue in many of the prior iterations leading to these validated models.

Muscle/Force	Peak Force Magnitudes (N)		
	Model KT170	**Model KT226***	**Model KT227***
Gluteus maximus	2010	2010	2010
Vastus lateralis	1722	1812	1812
Rectus femoris	1134	1039	1039
Vastus medialis	1020	1020	1020
Biceps femoris	395	395	395
Torso	80	85	85

Table 3.3-1: Peak force magnitudes for the muscles used in each of the three validated models. *KT226 and KT227 differ in the torso force but not in peak magnitude. The torso force for KT226 decreases down to $40\,N$ by 100% STS where the torso force for KT227 decreases to $45\,N$ (Figure 3.3-1)

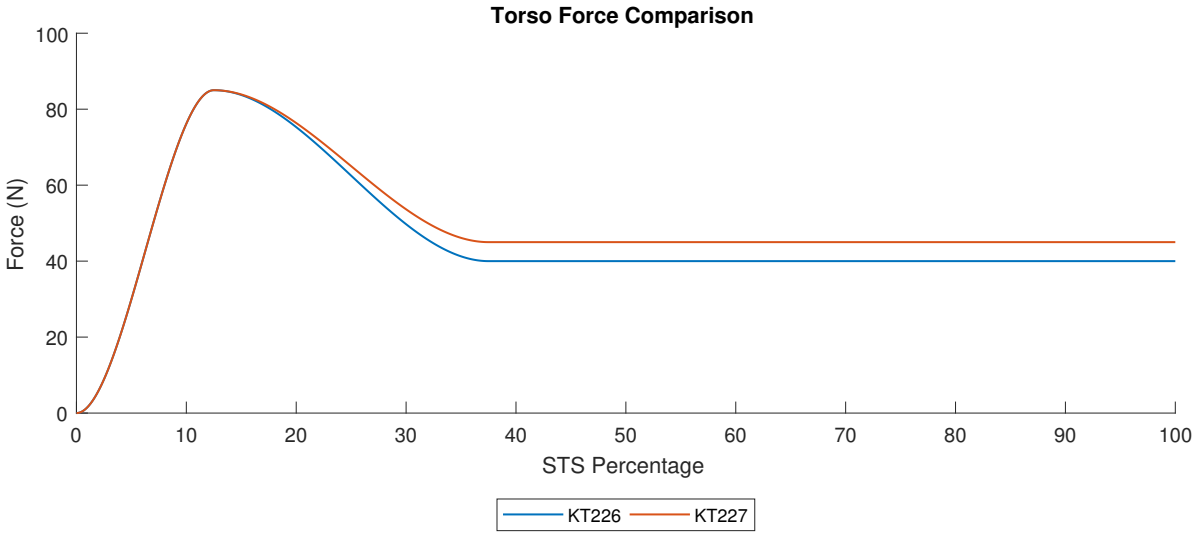

Figure 3.3-1: Models KT226 and KT227 differ only in the torso force. This is a plot displaying the slight variation.

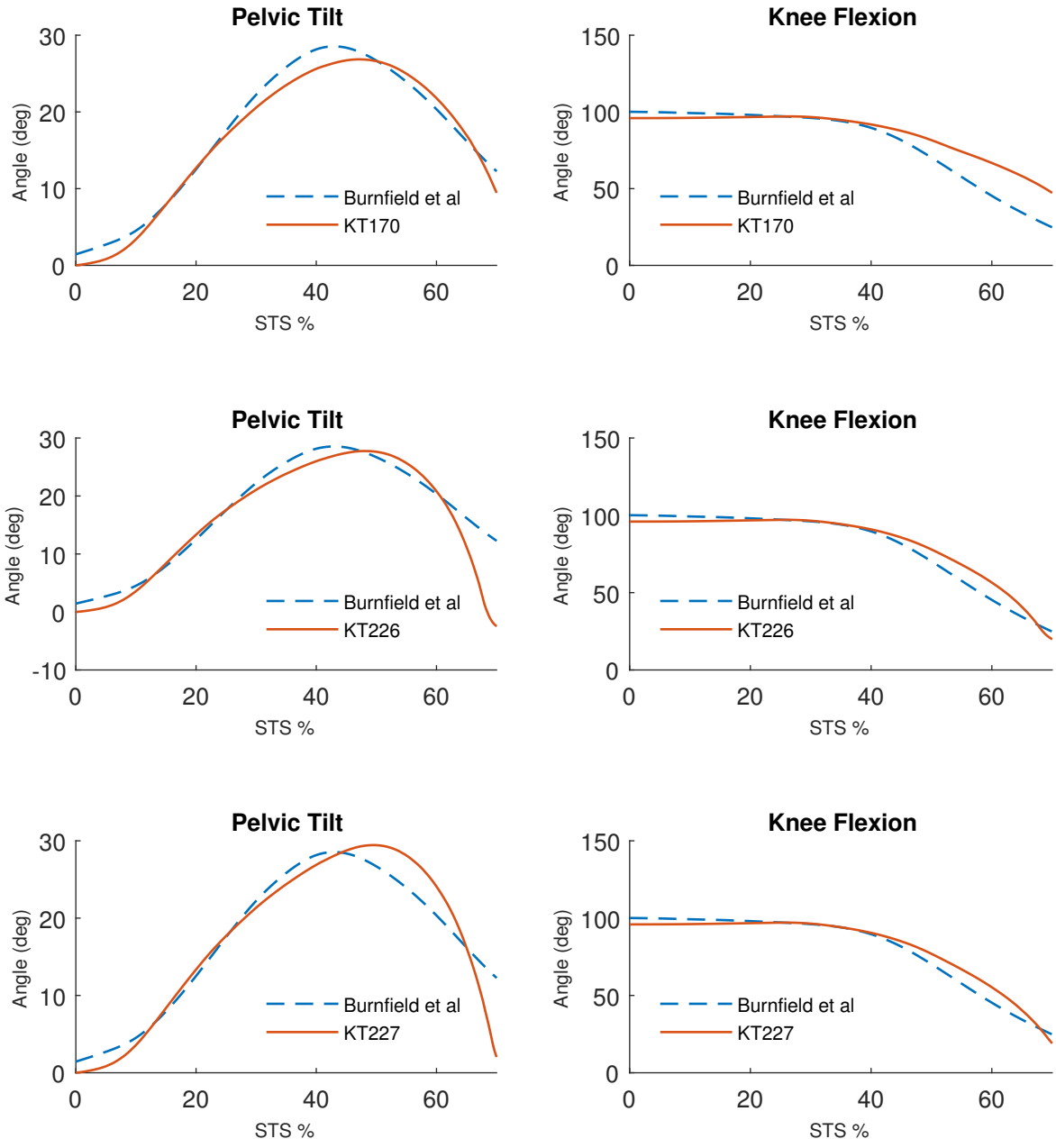

Figure 3.3-2: Kinematic data for the selected models plotted with the data from Burnfield et al [91].

Model	Pelvic Tilt RMSE (°)	Knee Flexion RMSE (°)
KT170	1.5	10.5
KT226	4.2	4.9
KT227	2.7	4.7

Table 3.3-2: Statistical results from the three chosen models displaying the RMSE values for both hip and knee motion.

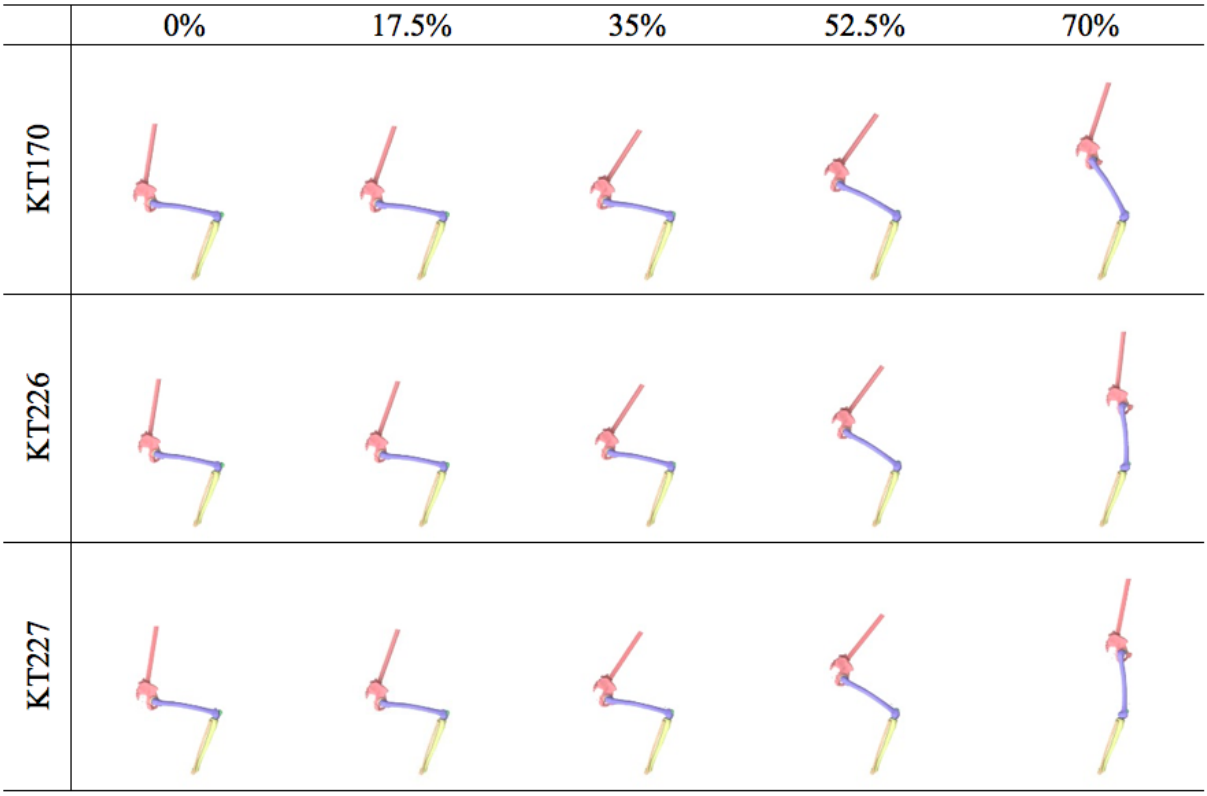

Figure 3.3-3: A series of images taken at five time points for each of the runs to provide context with the kinematic plots.

Model	Peak Pelvic Tilt (°)
KT170	26.9
KT226	27.8
KT227	29.4

Table 3.3-3: Peak pelvic tilt values for each of the models. The reported average was $28.1 \pm 7.0°$ [91].

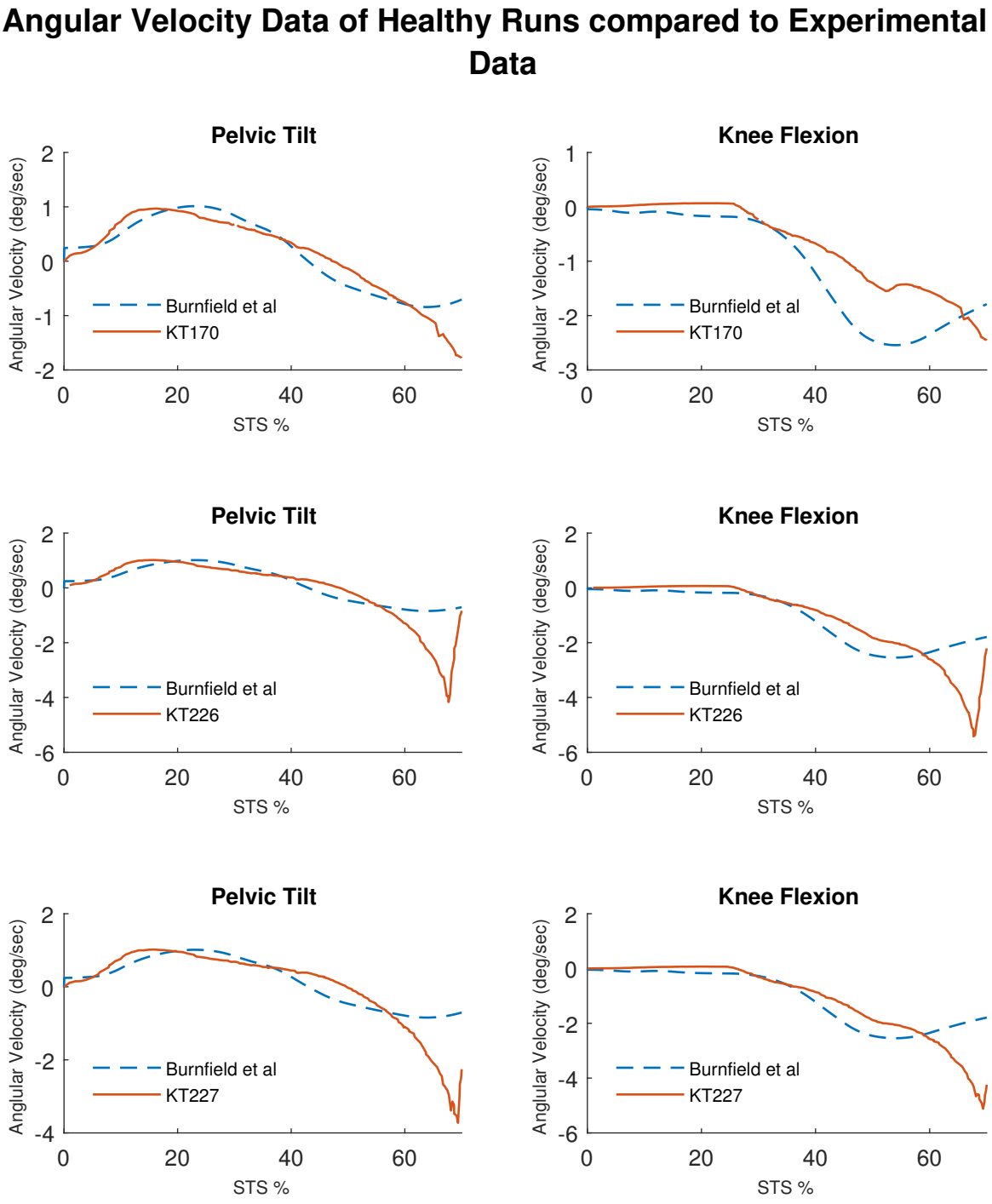

Figure 3.3-4: Angular velocity data for the selected models plotted with the data from Burnfield et al [91]. Velocity was calculated as the first-order derivative of the respective kinematics.

3.4 Discussion

These validated computational models of the lower extremity are capable of accurately representing the first 70% of a STS transfer. All the skeletal structures were represented as 3D rigid bodies and were oriented according to their respective anatomical coordinate system [89]. Soft tissue structures were created as a hybrid of rigid bodies and linear force vectors arranged such that both their line of action and anatomical shape were correctly matched. Outside of physical appearance, these soft tissue structures were programmed based upon data gathered from previous experimental studies. Muscle force magnitudes and activation timing were gathered from inverse dynamic and EMG analyses respectively [88,91]. Ligaments adjust their force magnitude in response to their environment based upon the linear distance between attachment sites and a known stiffness value (Table 3.2-2). This arrangement allowed for ligaments to perform their native function of stability and muscles to provide the driving force for the resulting motion. However, this arrangement also contained some simplifications that must be considered in analyzing the results.

Out of the iterations performed, three different models provided accurate representations of STS kinematics based upon their RMSE calculations. Between these three models, there was not a distinguishing factor for selecting one single model over the others. Consequently, all three models were chosen with each providing a better representation of an aspect of STS relative to the others. For instance, the pelvic tilt motion in model KT170 very closely resembled the experimental data (RMSE = 1.5°) while it lacked the appropriate knee flexion (RMSE = 10.5°). Models KT226 and KT227 were very similar and only differed slightly in their muscular inputs. However, KT226 reached a peak pelvic tilt very similar to that of the experimental data providing more accurate representation of what occurs at that point while KT227 was the best all-around model with a pelvic tilt peak only slightly higher than the experimental data and lower RMSE values than that of KT226. The advantages and disadvantages of each model should be considered when utilizing them for future studies.

Even though these models were successful in performing the STS motion, there were sources for error in the development. Motion during the lift-off phase was an indicator of this error in that the most deviation from experimental data occurred during this region. Both the hip and knee joints tended to experience higher rates of extension motion than what was reported by Burnfield et al [91]. The primary causes have already been mentioned as underlying RBM requirements. Removing deformation mandates creative alternatives to soft tissues that may not be able to fully mimic the native tissue. Matching muscle line of action as well as force generation through only linear force vectors and rigid bodies was a challenge. This model met that challenge with success but may not be perfect in every position throughout STS. Outside of modeling decisions, patient geometry and capability must be considered as the patient used for this model could vary quite a bit in their size and strength from that patients used by Burnfield et al [91].

Finally, it is important to note that sit-to-stand is a task that inherently varies amongst the entire population. Age, weight, strength, etc. all contribute to a person's ability to perform this task and thus affect the overall kinematics. Even the same individual may not perform this task the exact same way on each attempt. Some use their arms as a means for providing additional support while some rely solely on the lower extremity strength. This makes formal validation difficult because providing a baseline to compare to only resembles a select small population. Additionally, the lack of ankle motion could negatively impact these results. Without the ability to rotate the tibia and fibula, the resulting knee motion is only indicative of femur rotation. All of this should be considered when analyzing the validation results along with any future studies performed using this model as this model represents the average between 10 patients and future studies will be indicative of that sample size. However, even with anatomical variation and the simplifications made, this model was successfully able to mimic the kinematics of a true STS maneuver through the use of only soft tissue and osteoarticular constraints and will allow for future investigations

into hip joints kinematics during a sit-to-stand transfer. Continued use of this model will provide an indication of how various MSD's and morphological situations within the hip joint affect the overall kinematics of a STS transfer as well as how performing a STS transfer with these conditions can further affect the anatomy.

Chapter 4: Effect of Femoroacetabular Impingement on Sit-to-Stand Kinematics

4.1 Introduction

Femoroacetabular impingement is a pathological condition in the hip joint that occurs because of abnormal articulation between the femoral neck and acetabular rim. Typically, this occurs as a result of a region of overgrowth residing on either bone. These abnormalities lead to an impairment in joint range of motion and thus issues in performing daily functional activities such as gait. Increased instance of contact between the femur and pelvis causes joint pain and can lead to damage on the surrounding soft tissue structures [102,103]. There is further evidence, recently, that this abutment can lead to articular cartilage damage and thus FAI may be a mechanism leading to the onset of osteoarthritis over time [31]. Diagnosis of FAI involves a combination of clinical testing and medical imaging techniques to provide both an indication of the patient's range of motion and an idea of skeletal morphology. Magnetic Resonance Imaging (MRI) and X-ray are both commonly used in this diagnosis.

Cam-type and pincer-type are the two forms of impingement seen in patients (Figure 4.1-2). Cam impingement involves an unusual offset between the femoral head and neck typically from a bony protrusion present in that region. However, in some cases, the head can have a more posterior placement relative to the neck [103]. Pincer-type impingement involves an unusual overgrowth of the acetabular rim [103]. This can be a result of abnormalities such as acetabular retroversion, coxa profunda or protrusio acetabuli all of which involve irregular geometry in the acetabulum [102]. Both coxa profunda and protrusion acetabuli involve a deeper position of the acetabulum while acetabular retroversion, more commonly referred to as hip dysplasia, occurs when the mouth of the acetabulum has a more posterolateral

orientation [104–106]. Regardless of the impingement type, persistent contact between these structural abnormalities leads to damage on both the surrounding soft tissue as well as the underlying subchondral bone. Pain in the anterior region is consistent amongst both types and is a common indicator of FAI in general [8].

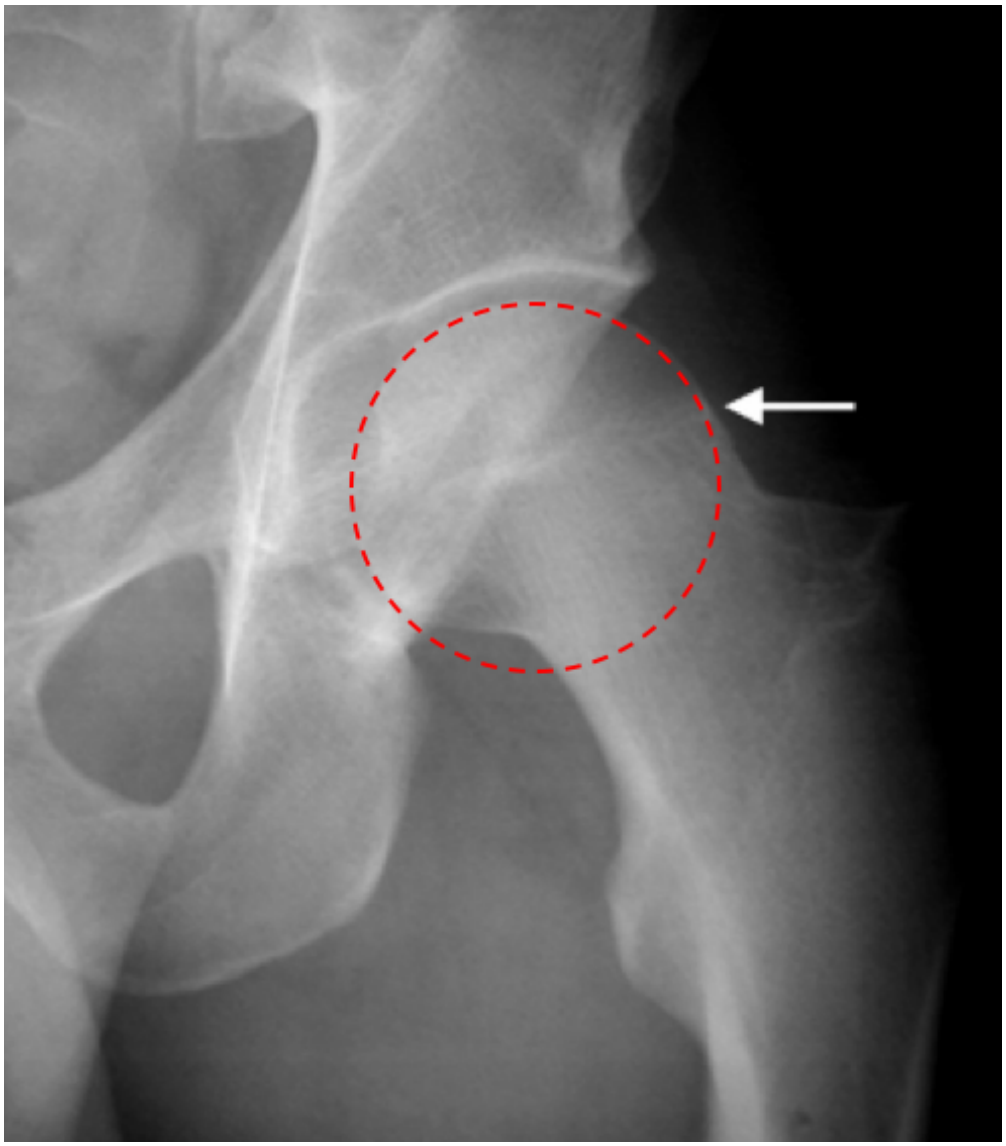

Figure 4.1-1: A radiographic image showing a point of impingement. The red circle is included to show where the asphericity of the femoral head connecting to the femoral neck occurs [102]

Data has shown that FAI has greater prevalence in athletic individuals and, therefore, it has been proposed that the physical activity has an underlying cause on development of FAI. Specifically, researchers believe that osseous growth in a region of higher stress along the neck causes development of the abnormality [29,107]. It has already been seen in phenomena such as stress-shielding that our native bone formation is highly dependent on the mechanical environment. In stress-shielding, the bone experiences less stress due to an implanted device with a high stiffness leading to bone resorption around the device [108]. In regions where the stress is high then, the bone could be remodeled by depositing more calcified matrix providing an opposition effect. In FAI, it is hypothesized that the femoral neck is experiencing higher concentrations of stress from elevated load through different activities, such as jumping or running, leading to elevated bone growth in that region [107].

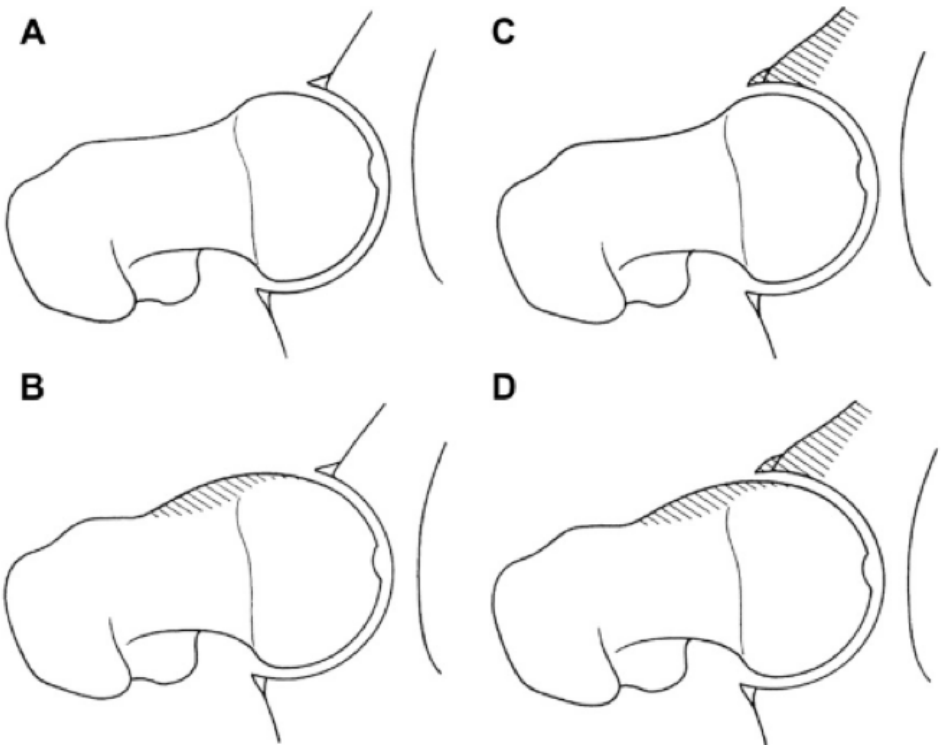

Figure 4.1-2: An anterior view showing the different forms of femoracetabular impingement with impingement zones highlighted: (A) Healthy hip (B) CAM impingement (C) Pincer Impingement and (D) Combined impingement [102]

Clinically, quantifying general acetabular and femoral morphology in reference to FAI involves two different measurements called the alpha angle and center edge angle (CEA) (Figure 4.1-3). Due to the locations for either type of impingement, these measurements are typically made with 2D radiography on an anterosuperior plane view that include the center of the femoral head. With the alpha angle, a circle closely defining the femoral head contour is placed over the 2D radiographic image. A line between the center of this circle and the point of bony defect is connected to the line defining the neck axis passing through the center of the circle. The alpha angle is the angle between these two lines (Figure 4.1-3). Asymptomatic patients present with average alpha angles of $55.0 \pm 8.8^\circ$ in this view while symptomatic patients average $65.2 \pm 7.3^\circ$ [28, 102]. CEA is used to determine acetabular morphology such as dysplasia in addition to pincer impingement. It is defined as the angle between a line perpendicular to the horizontal plane of the scan starting at the center of the femoral head and a line connecting the lateral-most aspect of the acetabulum with the center of the femoral head. A CEA value lower than 20° is typically considered to be dysplastic while pincer-type impingement cases have CEA values greater than 39° [103]. Both measurements were briefly described in Section 2.1. Current research has attempted to use newer 3D imaging technologies to more accurately determine impingement zones through combined femoral and acetabular morphology [61]. Further research on femoroacetabular impingement has focused on etiology, improvements in diagnosis and kinematic alterations [7, 29, 107, 109].

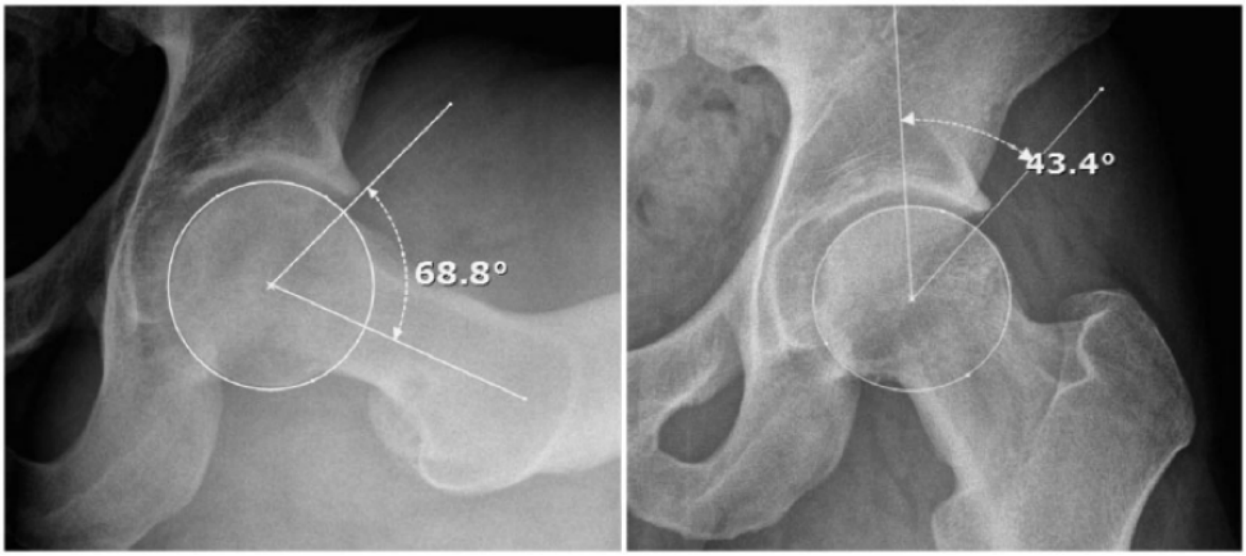

Figure 4.1-3: (Left) Radiographic image displaying the circle defining the femoral head, the line connecting the impingement point to the center of this circle and the line along the neck axis all used to calculate the alpha angle. (Right) Radiographic image showing the center-edge angle defined by a vertical line and the lateral most aspect of the acetabulum. Both lines must intersect at the center of the femoral head [28]

Several experimental studies have been conducted in an attempt to understand how FAI will affect the daily tasks of a patient with the condition [7,40,103]. Tasks such as squatting, walking and rising from a chair directly involve hip flexion motions potentially affected by FAI. FAI abnormalities have shown to affect patients during gait through a decrease in the peak extension angle as a result of the common symptoms of anterior joint pain and soft tissue tension [40]. In the extremes of hip flexion, experienced during a deep squat, patients with symptoms of cam-type impingement had a reduction in peak hip flexion and internal rotation angles. The most common location for the abutment or abnormality typically is located in the anterior region of the hip joint and thus physically limits the motion [7]. [7]. However, the impact of FAI on sit-to-stand has not been fully investigated. Therefore, the purpose of this computational study is to use kinematic and contact information to provide an indication of how FAI affects the kinematics of sit-to-stand and the resulting joint mechanics.

4.2 Methods

4.2.1 Model Development

Structurally, the difference between a hip diagnosed with cam-type FAI and a healthy hip lies in a bony protrusion or overgrowth along the anterosuperior region of the femoral neck and head. Development of a new model using a patient formally diagnosed with FAI would not provide data comparable to the validated healthy model as the skeletal geometry differs between each individual thus creating a variation in moment arms created by muscles. As the goal of this study was to investigate FAI relative to a healthy state, using skeletal anatomy from a separate patient would not permit this direct comparison between healthy and disease states. Rather, the healthy femur used previously was modified within the Mimics software to create a region of cam-type impingement. Mimics provides the ability to easily manipulate 3D geometry with real-time feedback through a contour editing feature (Figure 4.2-1). As mentioned in the previous section, cam impingement is quantified through an alpha angle measurement and typically patients with symptomatic FAI have an alpha angle of around $65.2 \pm 7.3°$. For this particular patient, the original healthy femur had an alpha angle of $53.7°$ and the modified FAI femur had an alpha angle of $65.2°$ measured in the anterosuperior plane. Both of these values match closely to what was defined as being healthy or FAI in the literature [28, 102]. Additional alpha angle measurements were taken in different planes to confirm the success of the modification (Table 4.2-1). Once completed, this modified femur simply replaced the original within the validated healthy models, maintaining all the same soft tissue elements. Ligamentous structures were applied the same stiffness and initial length parameters as seen in the healthy model and muscles applied the same force values over time. Acetabular morphology was not being investigated here so the native pelvis was used. These runs were again limited to 70% of STS transfer with the fixation of the tibia and fibula being the limiting factor.

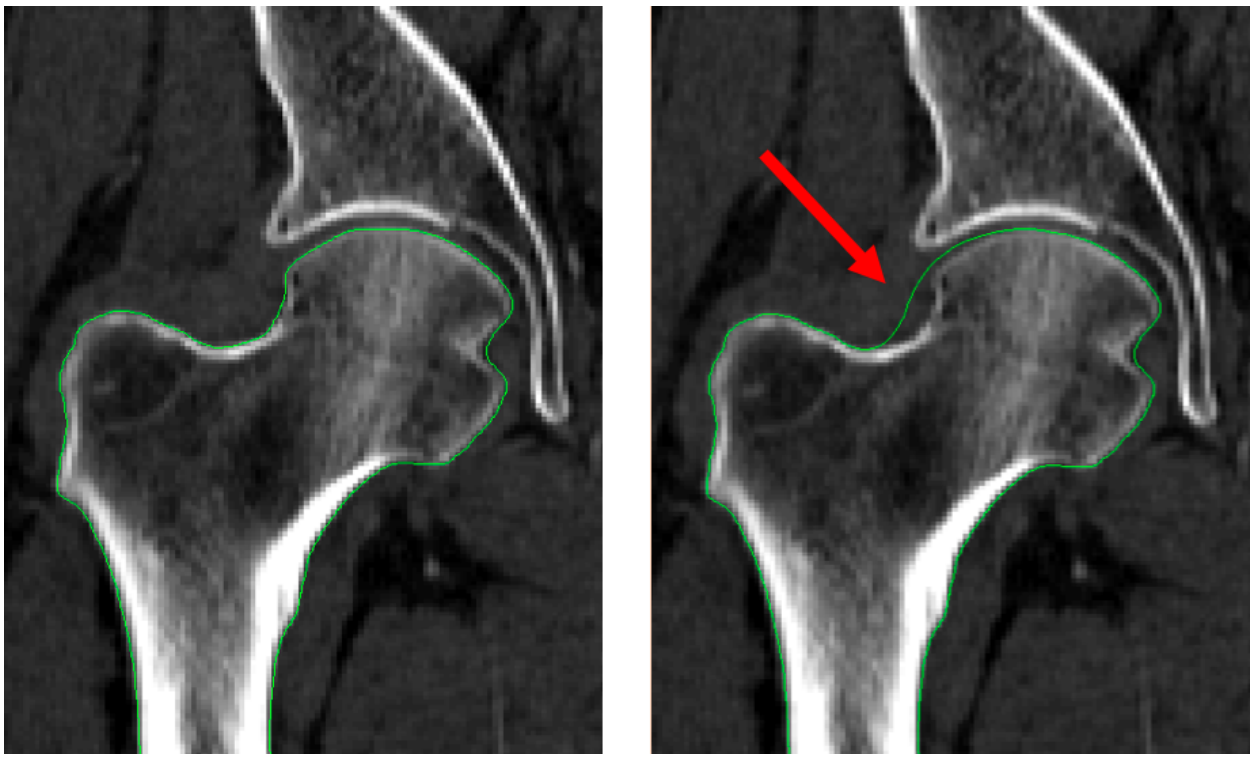

Figure 4.2-1: (Left) The original contour describing the unmodified, native anatomy for this patient. (Right) A modified contour in this particular view to create a region of impingement for this patient.

Plane	**Model Normal (°)**	**Model Disease (°)**	**Literature Normal (°)**	**Literature Disease (°)**
Anterior	48.9	50.1	48.2 ± 6.8	53.0 ± 9.8
Antero-superior	53.7	65.2	55.0 ± 8.8	65.2 ± 7.3
Superior	56.9	64.1	54.3 ± 9.8	54.3 ± 9.8

Table 4.2-1: The measured alpha angle values in different relevant planes compared with the reported values from literature [28, 102].

4.2.2 Data Analysis

Kinematic behaviors were gathered from the models. Results from this FAI model were analyzed using the previously mentioned custom Matlab functions (Appendix A). These functions imported the SolidWorks Model position data with respect to time for each FAI and respective healthy model, performed calculations on both kinematics and comparison, and then finally generated plots of pelvic tilt and knee flexion angles with regards to percentage of STS up to 70%. An additional plot with hip flexion was included to provide a relationship of the femur orientation relative to the pelvis. These hip flexion angles were calculated using a combination of both pelvic tilt and knee flexion angles (Figure 4.2-2). Within each kinematic plot, both the healthy and FAI data were included for a direct comparison. In addition to this kinematic data, the difference magnitude in angles between healthy and FAI data for each model was plotted with particular points of variation highlighted. More specifically, the point where the FAI kinematics began to truly differentiate from the healthy data along with the point of highest variation were marked. Determining the point of initial deviation was done with a threshold of 0.1° based on how the results were rounded. Finally, to provide an overall quantification of the comparison between FAI and healthy models, root mean square deviation (RMSD) was calculated. RMSD is calculated exactly as RMSE but is used to provide an indication of deviation rather than similarity.

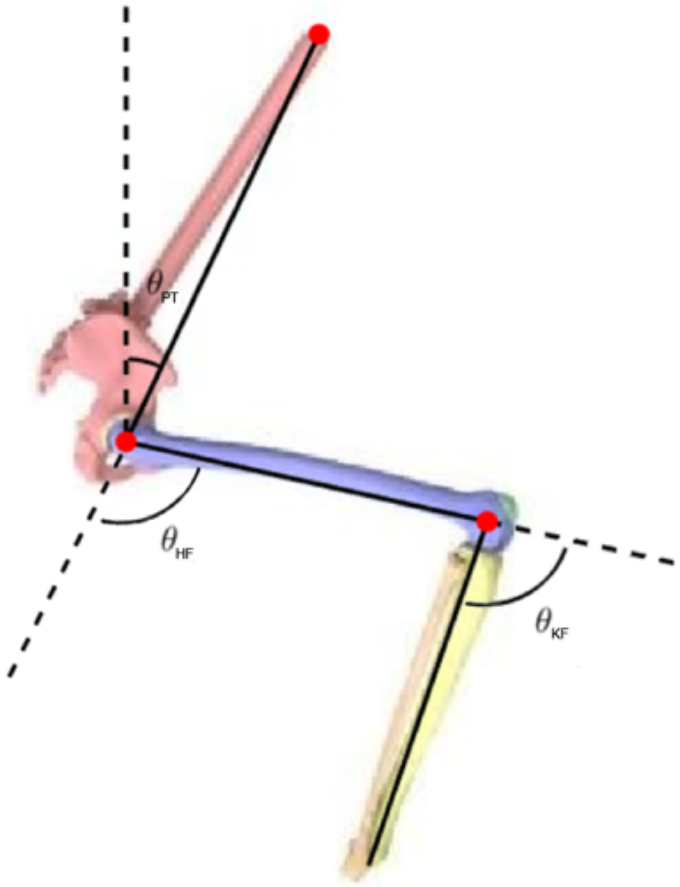

Figure 4.2-2: The hip flexion angles relative to both the pelvic tilt and knee flexion angles. θ_{HF} is the hip flexion angle and provides an indication of the femur orientation relative to the pelvis.

Contact between tissues is another area of concern with FAI patients. It is believed that abnormal contact between the region of bony overgrowth and surrounding structures could lead to tissue damage. As deformation is not permitted in rigid body motion, information regarding stress and strain within the joint throughout the motion could not be obtained. However, an advantage of using the ADAMS solver within SolidWorks for performing rigid body motion calculations is that body penetration and overlap are quantified in terms a volumetric measurement. Interference detection within SolidWorks performs this calculation based upon assigned contact parameters previously mentioned. Both this volume of overlap

and visuals for the overlap regions were gathered for five time points throughout the motion for each impingement model and compared back with their respective healthy model. Specifically, overlap between the femoral head and acetabular cartilage along with the femur and labrum were compared graphically for each validated model. Finally, the translation of the femoral head relative to the acetabulum was measured in all three directions as well as the magnitude of translation to provide context with the volumetric overlap as to the location of this contact.

4.3 Results

The results from each RBM were plotted for a direct comparison between FAI and non-symptomatic. Kinematics of FAI models did not vary much from the original healthy models in either pelvic tilt or knee flexion. Kinematic plots provide a visual representation of this comparison (Figure 4.3-1). It was not until approximately the point of peak pelvic tilt that the overall motion began to change for each model iteration. KT170 ended with higher pelvic tilt and knee flexion angles while KT226 and KT227 both experienced the opposite. These observations were further quantified through magnitude of deviation, RMSD values and deviation points of interest (Figure 4.3-2, Table 4.3-1 and Table 4.3-2). Model KT170 showed very little difference from its healthy alternative with RMSD values of 0.3° and 0.5° for pelvic tilt and knee flexion respectively and maximum amount of deviation of 1.8° and 2.8° for these same angles. Model KT227 resulted in the highest variation from its healthy state with RMSD values of 1.9° and 2.3° and maximum amount of deviation of 6.7° and 8.1°. An additional hip flexion plot was provided for each model, comparing FAI to healthy, to provide a direct indication of how the pelvis and femur are oriented with respect to each other (Figure 4.3-3). All three healthy models and all three FAI models reached a peak hip flexion value of approximately 98°, showing no difference between healthy and FAI models.

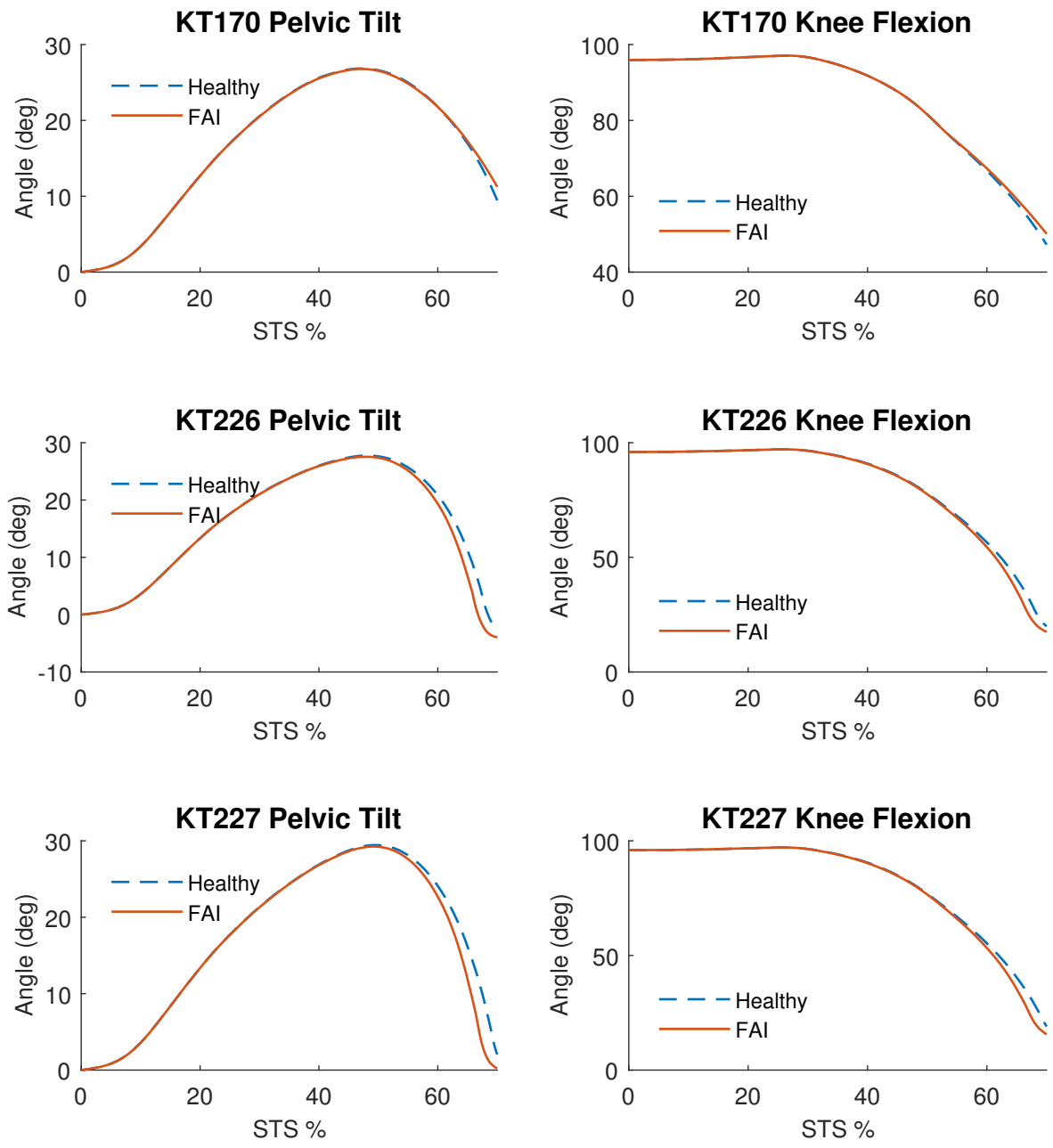

Figure 4.3-1: Plots showing how the healthy and FAI knee and hip kinematics vary for the three validated models.

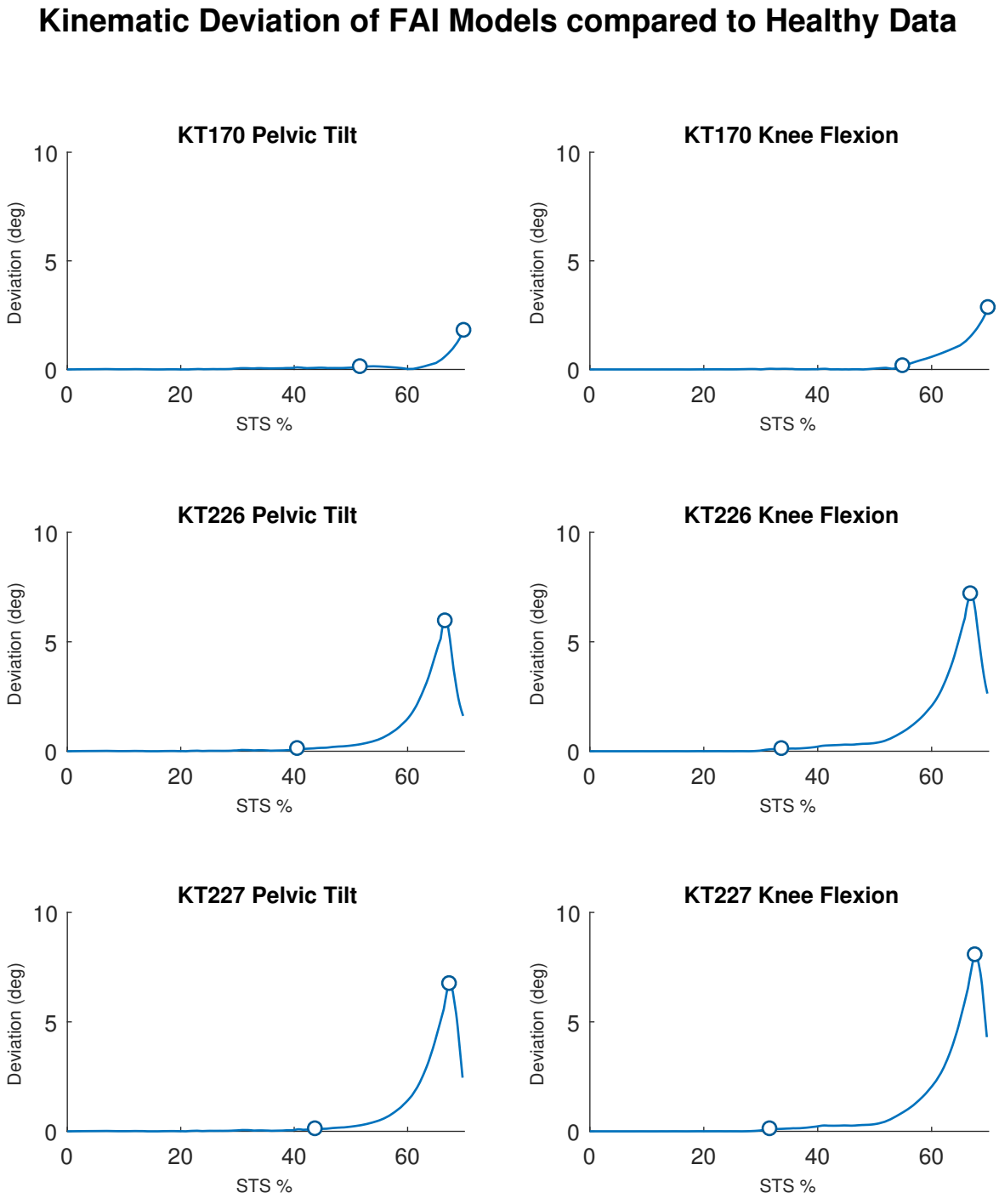

Figure 4.3-2: Plots showing the deviation between healthy and FAI cases for all 3 models. Points of initial variation and highest variation are highlighted. Exact values for these points are in (Table 4.3-2).

Model	Pelvis Tilt RMSD (°)	Knee Flexion RMSD (°)
KT170 - FAI	0.3	0.5
KT226 - FAI	1.7	2.1
KT227 - FAI	1.9	2.3

Table 4.3-1: RMSD values for the FAI models compared with their respective healthy models for both hip and knee motion.

	Pelvic Tilt			Knee Flexion		
	Initial Variation	Maximum Variation		Initial Variation	Maximum Variation	
Model	%STS	%STS	Diff Mag (°)	%STS	%STS	Diff Mag (°)
KT170 - FAI	51.7	70.0	1.8	55.0	70.0	2.8
KT226 - FAI	40.7	66.7	5.9	33.8	66.9	7.2
KT227 - FAI	43.8	67.5	6.7	31.7	67.7	8.0

Table 4.3-2: Highlighted points of variation between the three validated healthy models and their respective FAI models. The %STS for initial variation in addition to the %STS and magnitude of maximum variation are included for all THA models. Point of initial variation indicates the point where the magnitude difference between healthy and FAI models is greater than 0.1 degrees. As each value was rounded to a single decimal point, variation greater than 0.1 provides a numerical indication of this variation seen in the rounded results.

Figure 4.3-3: Hip flexion plots for each model. The angles were calculated based upon pelvic tilt and knee flexion angles to provide a better indication of the pelvis orientation with respect to the femur.

With regards to contact and body penetration, images with overlap regions as well as the volume of overlap magnitudes were recorded for five different time points in each model on both the acetabular cartilage and the labrum. For cartilage contact, all three models showed the same trend in contact amount with very little at 0% STS and increasing to a maximum value at 70% STS. At 0% STS, the pelvis ischial region was resting on a seat platform making in-situ strain from capsular ligaments the only factor promoting contact between the joint articular surfaces. Overlap between the femoral head and acetabular cartilage was slightly greater for the FAI models than the healthy for most cases (Figure 4.3-4). Visually, the difference in amount of overlap is difficult to discern between models (Appendix B). In the recorded results (Table 4.3-3), volume values predicted by the FAI models were given colors based upon their comparison to the healthy model. Red designates higher overlap volume and green refers to lower overlap volume with darker shades of either color representing a difference greater than 10% compared to the healthy state.

Model	Volume of Overlap (mm^3)				
	0%	17.5%	35%	52.5%	70%
KT170 (Healthy)	5.6	54.9	420.5	772.0	844.7
KT226 (Healthy)	5.6	56.2	402.1	766.7	929.8
KT227 (Healthy)	5.6	56.2	410.3	749.7	921.0
KT170 (FAI)	5.6 (+0.0%)	63.4 (+15.5%)	446.0 (+6.1%)	464.5 (−1.0%)	800.9 (−5.2%)
KT226 (FAI)	5.5 (−1.8%)	70.5 (+25.4%)	438.7 (+9.1%)	781.1 (+1.9%)	928.9 (−0.1%)
KT227 (FAI)	7.7 (+37.5%)	63.4 (+12.8%)	437.1 (+6.5%)	780.7 (+4.1%)	946.5 (+2.8%)

Table 4.3-3: Part overlap between femur and acetabular cartilage throughout the motion in units of mm^3. For the FAI models, red signifies a higher volume of overlap, green is a lower volume and grey is equal amounts. Darker shades of either color represent a difference of greater than 10% from the healthy state.

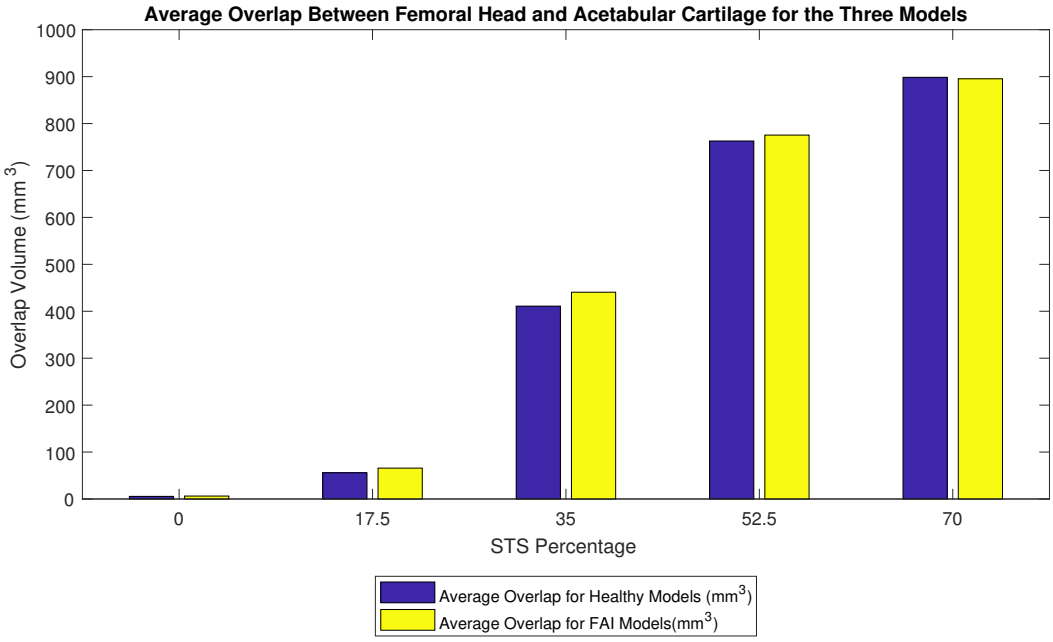

Figure 4.3-4: Average volume of overlap of all three models between femoral head and acetabular cartilage for healthy and FAI models.

With labrum contact, the same data was gathered as with cartilage and there were different results. Most notably, there was not any overlap between femur and labrum bodies until approximately 35% STS and even then there were negligible amounts. The amount of volumetric overlap peaked at the 52.5% STS point for healthy and FAI models and had begun to decline by 70% STS. At 52.5% STS, model KT170 had an increase in overlap volume by 21.1% while both KT226 and KT227 had less than 4% increase. At 70% STS, there was a range of observed results seen for both healthy and FAI cases. In particular, KT170 showed a sharp increase (347.2%) in overlap volume from healthy to FAI cases where both KT226 and KT227 had significant decreases in this overlap volume. Refer to Appendix B to see all images of the overlap for each model at the 5 time steps. Results from FAI models were again given colors based upon their relationship to the healthy model (Table 4.3-4) with the same color scale the previous table. Due to the low amounts of penetration, further investigation into the tension developed through three regions of the labrum was done (Figure 4.3-6). There was higher tension experienced in the labrum posterior region for all three models relative to other regions. Throughout the STS motion, FAI models showed slightly higher magnitudes in labrum tension force for all three regions in comparison to the healthy joint with the posterior and superior regions seeing larger deviations. There was very little tension developed in the anterior region until approximately 65% STS.

Model	Volume of Overlap (mm^3)				
	0%	17.5%	35%	52.5%	70%
KT170 (Healthy)	0.0	0.0	0.0	42.1	12.5
KT226 (Healthy)	0.0	0.0	0.0	43.4	42.0
KT227 (Healthy)	0.0	0.0	0.0	43.1	27.7
KT170 (FAI)	0.0 (+0.0%)	0.0 (+0.0%)	0.0 (+0.0%)	51.0 (+21.1%)	55.9 (+347.2%)
KT226 (FAI)	0.0 (+0.0%)	0.0 (+0.0%)	0.0 (+0.0%)	45.1 (+3.9%)	5.2 (−87.6%)
KT227 (FAI)	0.0 (+0.0%)	0.0 (+0.0%)	0.0 (+0.0%)	43.1 (+0.0%)	21.8 (−21.3%)

Table 4.3-4: Part overlap between femur and labrum throughout the motion in units of (mm^3). For the FAI models, red signifies a higher volume of overlap, green is a lower volume and grey is equal amounts. Darker shades of either color represent a difference of greater than 10% from the healthy state.
*There was part overlap at 35% but it was $< 0.1mm^3$ making the rounded value 0 for all models.

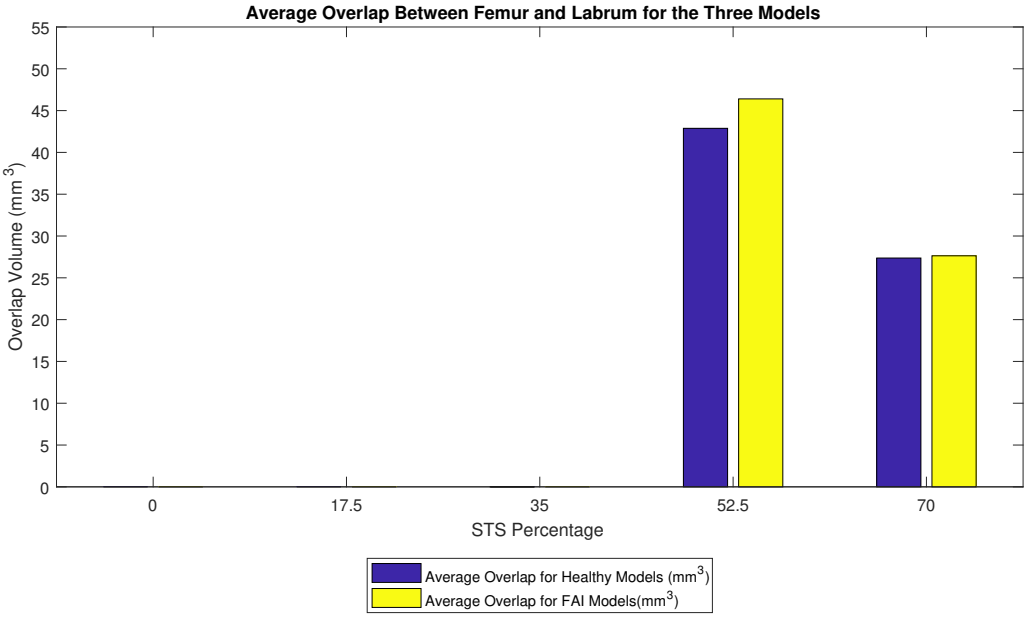

Figure 4.3-5: Average volume of overlap of all three models between femur and labrum for healthy and FAI model.

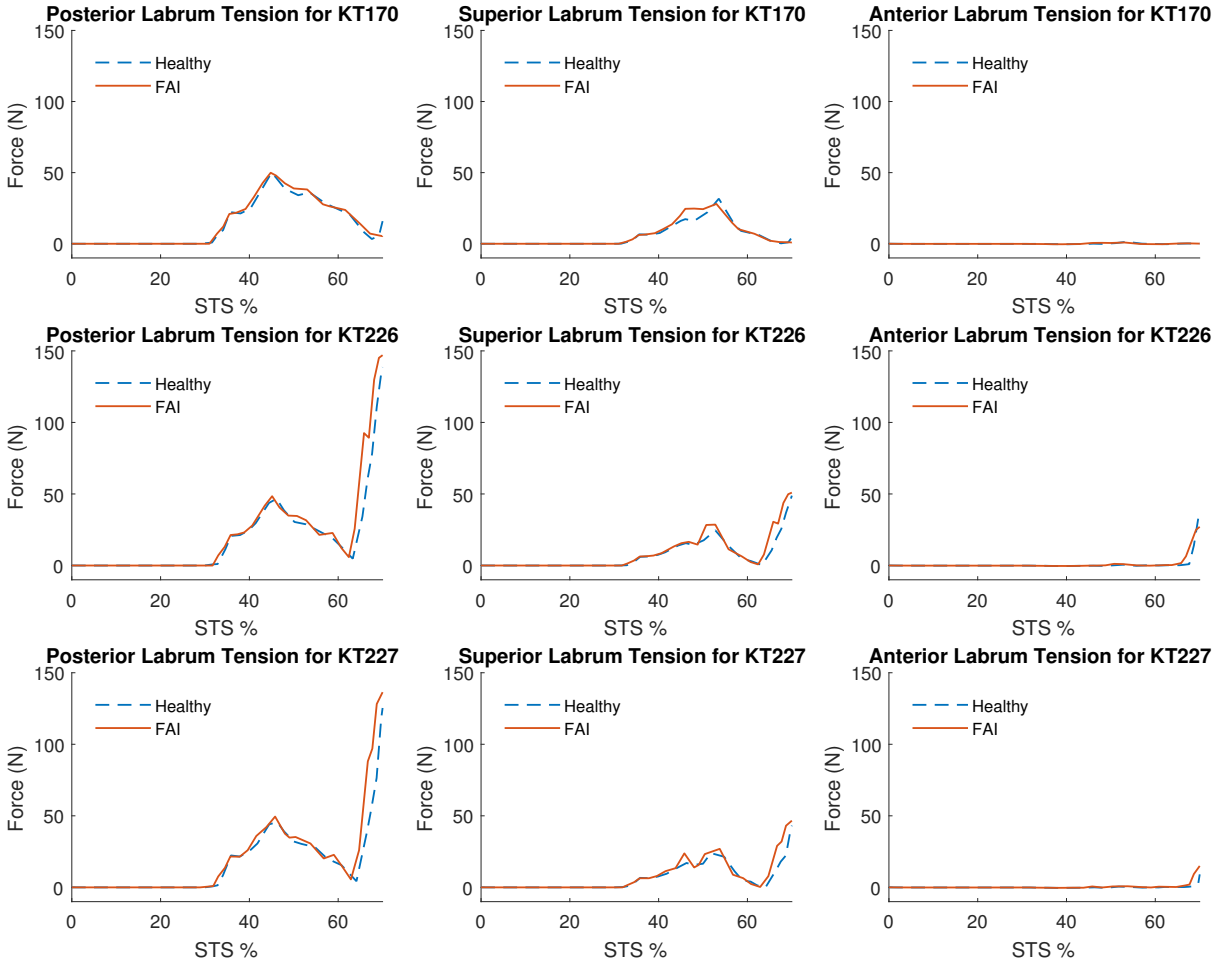

Figure 4.3-6: Tension magnitudes experienced in the posterior (left column), superior (middle column) and anterior (right column) for each of the FAI models compared to their respective healthy states. Each row refers to a single model while each column refers to a region in the labrum.

For all three models, there was a shift of the femoral head posteriorly, medially and superiorly relative to its initial position within the acetabulum suggesting that the femoral head was being forced deeper into the socket as the motion progresses (Figure 4.3-7). Between FAI and healthy cases, there was very little difference in each of the directions meaning the amount of translation occurring during FAI cases was not different from the healthy cases.

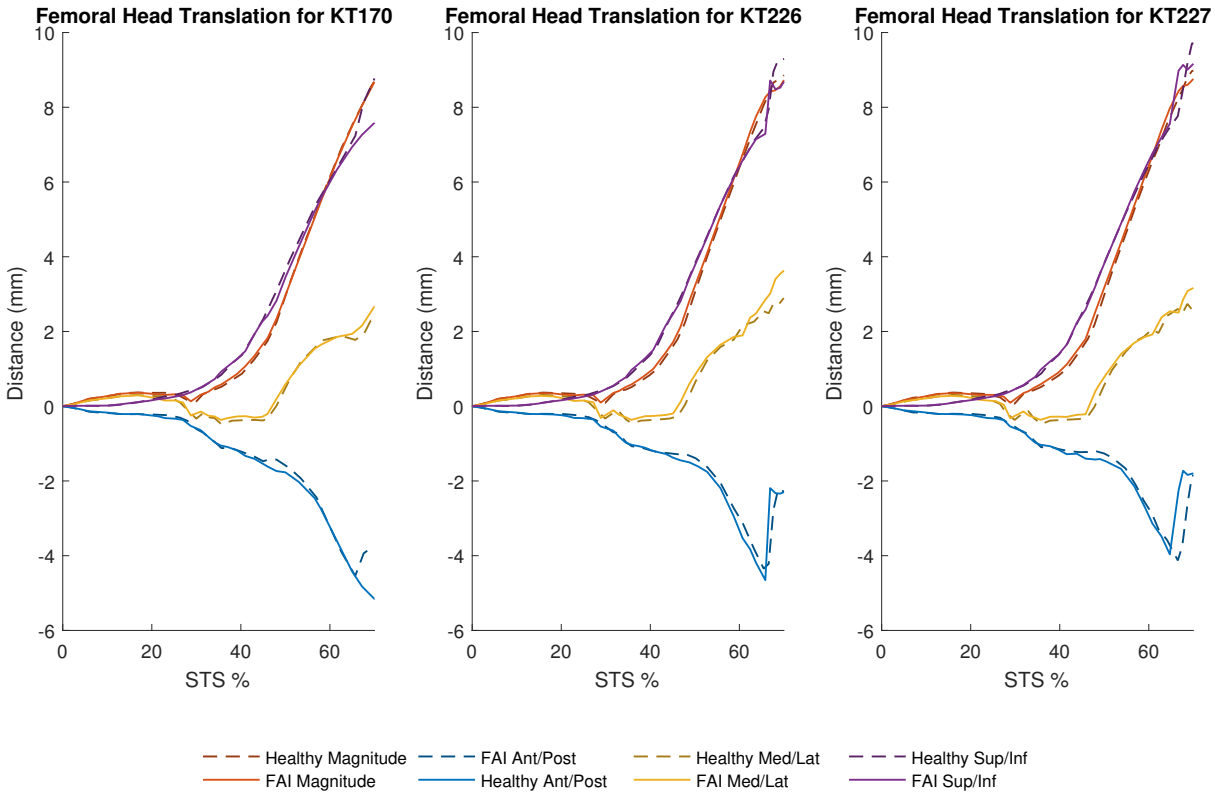

Figure 4.3-7: Femoral head translation in all three directions along with the magnitude relative to its initial position within the acetabulum. In this case, anterior, medial and superior are considered to be positive.

4.4 Discussion

This study utilized three previously validated computational models of the lower extremity to examine how differences in hip morphology due to symptomatic femoroacetabular impingement affected the biomechanics of a sit-to-stand transfer. The models were modified to include a femur with an overgrowth region in the femoral neck consistent with that typically seen in patients diagnosed with FAI. All applied soft tissue structures were maintained to be consistent with the original healthy models. Function of the models was completely

dependent upon the physical skeletal anatomy along with the implementation of surrounding soft tissue structures. Both kinematic and contact data were gathered in the form of joint angles and solid body volumetric overlap.

Results from this study showed that there were only slight alterations in the kinematic data for both pelvic tilt and knee flexion seen in both the low RMSD values (Table 4.3-1) and in the kinematic plots providing a visual comparison between cam-type impingement and healthy hip states (Figure 4.3-1). Most notably, the maximum amount of deviation between FAI and healthy models occurred after the point of peak pelvic tilt for all three models with both the pelvis tilt and knee flexion motion plots. There has been very little work done previously investigating the relationship between cam-type impingement and STS kinematics to provide a comparison. However, previous experimental studies have reported that cam-type FAI does alter kinematics for gait and deep squat tasks through a decrease in range of motion [7, 40]. Bagwell et al (2015) investigated how cam-type FAI affects deep squat kinematics between symptomatic patients (n=15) and healthy participants (n=15) and reported that peak hip flexion angles were all reduced with impingement cases. More specifically, peak hip flexion was reduced for FAI cases from $113.0 \pm 6.7^\circ$ to $106.6 \pm 14.0^\circ$. The measured peak hip flexion was approximately 98° for each of the healthy models and this was not changed with the addition of impingement suggesting that these lower amounts of hip flexion experienced during STS were not high enough for the FAI morphology to provide restrictions similar to what is seen in a deep squat (Figure 4.3-3). During gait, Kennedy et al (2009) reported that patients with cam-type FAI (n=17) experienced a decrease in their hip extension range as opposed to hip flexion when compared with asymptomatic participants (n=14). This was attributed to a pain-coping mechanism as a result of anterior soft tissue damage developed over time, an aspect that cannot be quantified via a computational model. Additionally, the STS models do not experience hip extension passed the neutral position making the results not applicable for comparison. Within both studies, cam-type FAI was

determined by patients with alpha angles greater than 50.5° and healthy participants all presented with no prior history of lower extremity issues. The plane of measurement for these alpha angles was not reported but, in reference to the measurements taken for this model (Table 4.1-3), these studies were most likely referring to the anterior plane where the literature reports alpha angles for symptomatic patients to be $53.0 \pm 9.8°$. The FAI models had an alpha angle of 50.1° in this plane.

The average amount and location of contact regions within both the acetabular cartilage and the labrum as well as the translation of the femoral head within the acetabulum followed a similar trend as seen in the kinematics with a small amount of difference between the healthy and impingement states (Figure 4.3-4, Figure 4.3-5, Figure 4.3-6 and Figure 4.3-7). Between 17.5% and 35% of STS there was a consistent increase in cartilage contact for each of the impingement models relative to their healthy states (Table 4.3-3). This increase could potentially be inconsequential with respect to altered biomechanics. However, with a task performed as frequently as STS, this slight increase in contact could potentially lead to tissue damage through repetitive incidents and fatigue over time. The tendency for the femoral head to have a more posterior shift in contact on the acetabular cartilage during a sit-to-stand transfer has been observed previously in a finite element analysis study performed by Henak et al (Figure 4.4-1) [110].

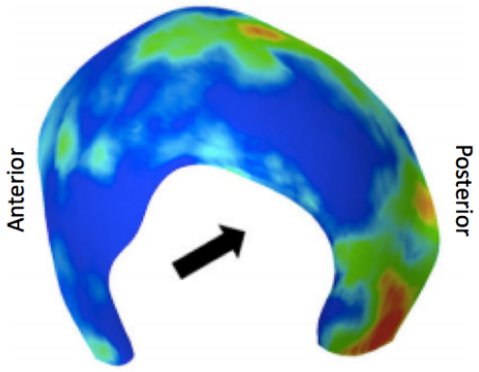

Figure 4.4-1: A stress concentration map of the acetabular cartilage from a study done by Henak et al showing posterior contact during a sit-to-stand transfer [110].

It has been shown previously that tissue damage, as a result of FAI, occurs at the region of contact [31,111]. However, damage reported in those studies occurred due to high incidences of anterior contact from the impingement region, as a result of high angles of hip flexion. In contrast, the overlap images in Appendix B along with the translation plots (Figure 4.3-7) show that the region of overlap for both the healthy and the FAI models occured posteriorly and superiorly for cartilage and labrum without any anterior overlap occurring. In addition, there is almost no tension developed in the anterior portion of the labrum until later in the motion (Figure 4.3-6). This further suggests that the amount of hip flexion experienced during STS in all models is not large enough to induce the contact necessary to provide anterior pain and potentially damage. However, as a consequence of the confined acetabular coverage around the femoral head, it is feasible that these slight increases in contact and translation posteriorly during FAI models could increase the stress experienced along the articular surfaces in the cartilage potentially leading to damage on these surfaces. Lastly, at 70% STS, there were rather large differences between healthy and FAI states in labrum contact with KT170 showing a significantly larger amount of contact and both KT226 and KT227 having much less contact (Table 4.3-4). This is most likely attributed to the slightly altered joint angles at 70% STS for these FAI models. KT170 had a higher pelvic tilt angle in comparison to its healthy state whereas KT226 and KT227 had lower pelvic tilt angles at this point (Figure 4.3-1).

The manner in which this model was developed provided a potential source for error. To proceed with the validated STS model from Chapter 3, the same skeletal structure and anatomy had to be maintained. Using anatomy from a separate patient diagnosed with FAI would result in different bone geometry leading to changes in the muscle moment arms. Therefore, the original femur was modified to mimic conditions of FAI. More specifically, the femoral neck and head were modified to create a region of overgrowth consistent with cam-type impingement. The resulting morphology was verified through alpha angle measure-

ments taken in three different planes to provide confidence in the modifications. In addition, these models assumed there was no alteration in soft tissue mechanical properties or muscle strength as a result of long-term diagnosis of FAI. It has been mentioned in previous work that these structures could become damaged over time as a result of FAI [8, 102, 103]. Regardless, these structures maintain the same parameters in the impingement models as implemented and defined during the validation process for consistency between models. Finally, similar to the validation process, simplifications had to be made during the actual development process for the original model. These simplifications were outlined in the previous chapter. However, even with these errors and assumptions, the previously validated computational models were successfully able to provide insight into how femoroacetabular morphology alone affects STS kinematics and articular contact surfaces contributing to the further understanding of cam-type impingement cases.

Chapter 5: A Computational Study of Combined Version in Total Hip Arthroplasty Using Sit-to-Stand Kinematics

5.1 Introduction

Surgical intervention for hip joint diseases dates as far back as the 1820's when John Rhea Barton performed an osteotomy on an ankylosed hip. However, it was not until nearly a century later, in 1927, that a true replacement for the femoral head was attempted in a patient. It was constructed entirely out of ivory, and was unsuccessful, but it opened a door to years of research into this topic. In 1948, the Judet brothers developed a methyl methacrylate femoral head implant, which truly began the widespread use of hip replacement surgeries. Their work became rather significant is this field for proving that the interaction between human biological tissue and non-organic materials was possible with minimal damage or infection. Throughout the 1950's, there was a shift in the research done in this area. Non-metallic materials were replaced with sturdier metallic materials and longer stems were implemented providing more stability. In the years to follow, more sophisticated techniques and materials were formed. Techniques including how the actual device is fixated or attached in the skeletal anatomy, handling of the surface topography for articulating surfaces and attachment sites, and the actual material for the implant all were key areas of research for the past century [55].

In present times, total hip arthroplasty surgery is becoming an increasingly popular procedure treatment of pain and dysfunction associated with common hip joint diseases of Osteoarthritis (OA), Rheumatoid arthritis (RA) and chondromalacia. These involve either skeletal damage, cartilage damage or both and tend to develop over time in elderly patients

rather than appearing as a sudden onset. By 2010, approximately 2.5 million individuals in the United States had undergone a THA procedure with approximately 253,000 performed in 2010 alone [48, 112, 113]. It is projected that by 2030 this number will rise to approximately 572,000 THA procedures per year, a 126% increase [112]. Coinciding with this rise in popularity of clinical practice, comes a rise in the amount of research to improve the current standards. Improvements in design of the arthroplasty components, the materials comprising the components, as well as the surgical techniques for implantation have all led to the increased success of the procedure and implant longevity [34,35,114,115]. An implant can vary in complexity from only a single part to several different parts each interacting with one another. Implants tend to have their own material or set of materials chosen for specific purposes. Known materials commonly used include metals and alloys, polymers such as polyethylene (more specifically UHMWPE), bulk metal glasses (BMG) and ceramics such as aluminum oxide [55,116,117]. PTFE was originally chosen as a potential bearing material due to its frictional properties but was later abandoned due to its high wear rates compared to the other listed materials.

In general, a THA procedure is a highly traumatic event that typically leads to inflammation surrounding the joint, high levels of stress hormones and an elevated immune response. These symptoms could remain for weeks post-operation [118]. However, a successful implant will vastly improve the lifestyle and functional capabilities of the patient. There are several factors that play a role in the success or failure of a THA procedure that can be narrowed down into either material chosen or implant placement and specifications. Due to the nature of a RBM, the material of each part is irrelevant for the results of this study. However, the placement and alignment could affect the kinematics relative to the native healthy state under identical applied forces. More specifically, version and inclination of both the acetabular cup and femoral neck are important to keep in mind. These measurements provide an indication of the orientation of the native femur and acetabulum in addition to the placement

of THA components.

Femoral anteversion describes the femoral neck orientation relative to the condylar axis thus describing the femoral shape and orientation in the transverse plane (Figure 5.1-1). Anteversion refers to an anterior orientation of the neck relative to the condylar axis while retroversion refers to a posterior orientation. According to Fujishiro et al, preoperatively, patients typically present with a wide range of femoral version from 13.4° of retroversion to 80.0° of anteversion with an average of 31.0° of anteversion (n=1,555) [119]. Femoral inclination is the angle between the femoral neck and the femoral shaft and typically ranges from 120° to 135° for a healthy femur [120, 121] (Figure 5.1-1). Acetabular anteversion is defined as the angle between a line connecting the lateral anterior and posterior margins of the acetabular cup and the sagittal plane [119] (Figure 5.1-2). According to Fujishiro et al, patients have a range of 24.0° of acetabular retroversion to 56.7° of anteversion with an average of 20.2° of anteversion in the native anatomy (n=1,555) [119]. Acetabular inclination is the angle between the transverse plane and the line connecting either end of the acetabular rim taken in the frontal plane (Figure 5.1-2) and, according to Fowkes et al, ranges from 32.1° to 45.5° with an average of 38.8° in native hips (n = 200) [122]. The native anatomy for this model contained 27.9° of acetabular anteversion, 33.7° of acetabular inclination, 15.5° of femoral anteversion and 121.2° of femoral inclination.

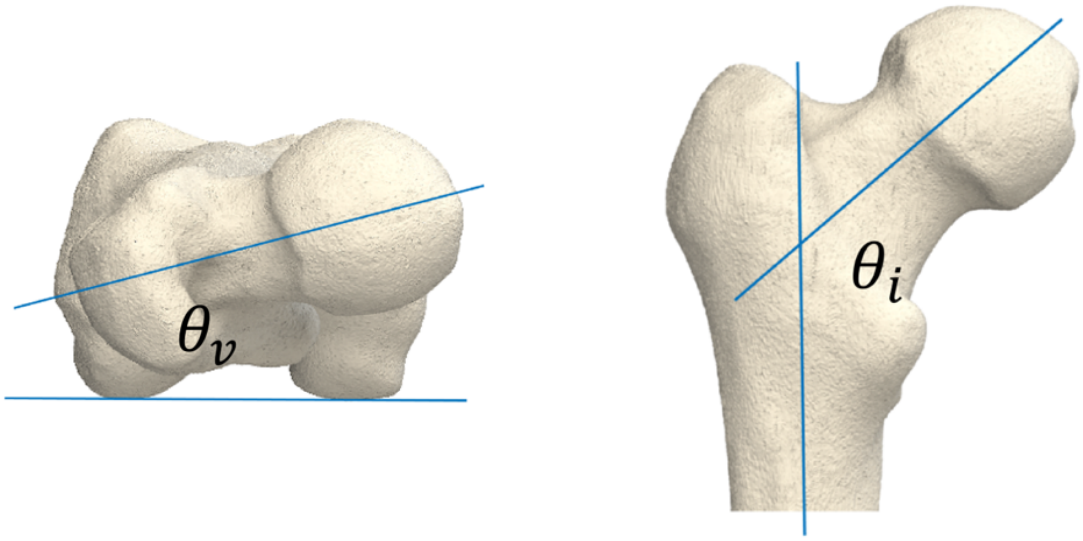

Figure 5.1-1: (Left) The neck axis and condylar axes, measured in the transverse plane, are used to determine femoral version. (Right) The neck and shaft axes, measured in the frontal plane, are used to determine femoral inclination.

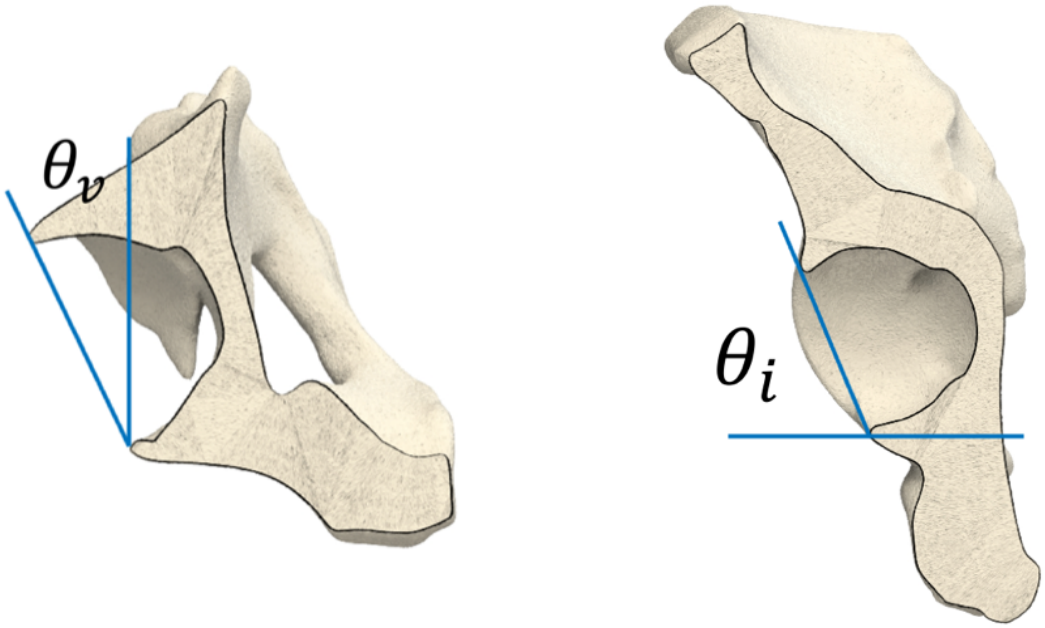

Figure 5.1-2: (Left) Acetabular version is measured as the angle between the sagittal plane and the line connecting either end of the acetabular rim in the transverse plane. (Right) Acetabular inclination is the angle between the transverse plane and the line connecting either end of the acetabular rim taken in the frontal plane.

Native anteversion and inclination are not always replicated with a THA procedure [123]. When performing a THA procedure using cemented fixation, the acetabular component is typically placed first and should be aligned according to the Lewinnek range of $5 - 25^\circ$ of anteversion and $30-50^\circ$ of inclination with average values of 15° and 40° respectively [35,124]. Subsequently, the femoral component is placed such that a combined version (CV) goal is met. An ideal range for this measurement is inconsistent in the literature with some sources stating combined version should be between 40–60° and others stating it should be between 25–45° [68, 125–127]. Improper application of the implants could lead to lower hip stability and thus higher incidents of dislocation, decreased range of motion and, excessive contact between parts [55]. Each of these will lead to discomfort for the patient and potentially a revision procedure to correct the initial failed attempt. With this study, these issues will be considered further. The sit-to-stand rigid body model previously validated was used further by producing the conditions of a total hip arthroplasty in order to refine the inconsistencies for a desired CV angle through investigation of STS kinematics.

5.2 Methods

5.2.1 Model Development

Total hip arthroplasty implants have a degree of variation between companies in shape and size of the parts. Universally speaking, the acetabular cup could be considered as a simple hemispherical cup with an inner polyethylene (PE) liner and a metallic outer shell. As deformation and attachment methods were disregarded, fixation between these two parts and material properties between metal and PE were not considered in developing the acetabular parts. A simple hemispherical shell with a hemispherical liner were developed based upon the DePuy Synthes PINANCLE acetabular cup to represent this component (Figure 5.2-1, Figure 5.2-2). Similarly, the femoral component has a variety of intricacies in shape that differ between brands and companies with stem size and shape as well as neck shape. Only

the neck and head were considered in this case as fixation within the rigid body model does not require direct contact between parts. A simple cylindrical shape transforming into a somewhat rectangular base was developed as the femoral neck with a spherical ball capping the end as the femoral head component. This was based on the DePuy Synthes SUMMIT tapered femoral component (Figure 5.2-1, Figure 5.2-3).

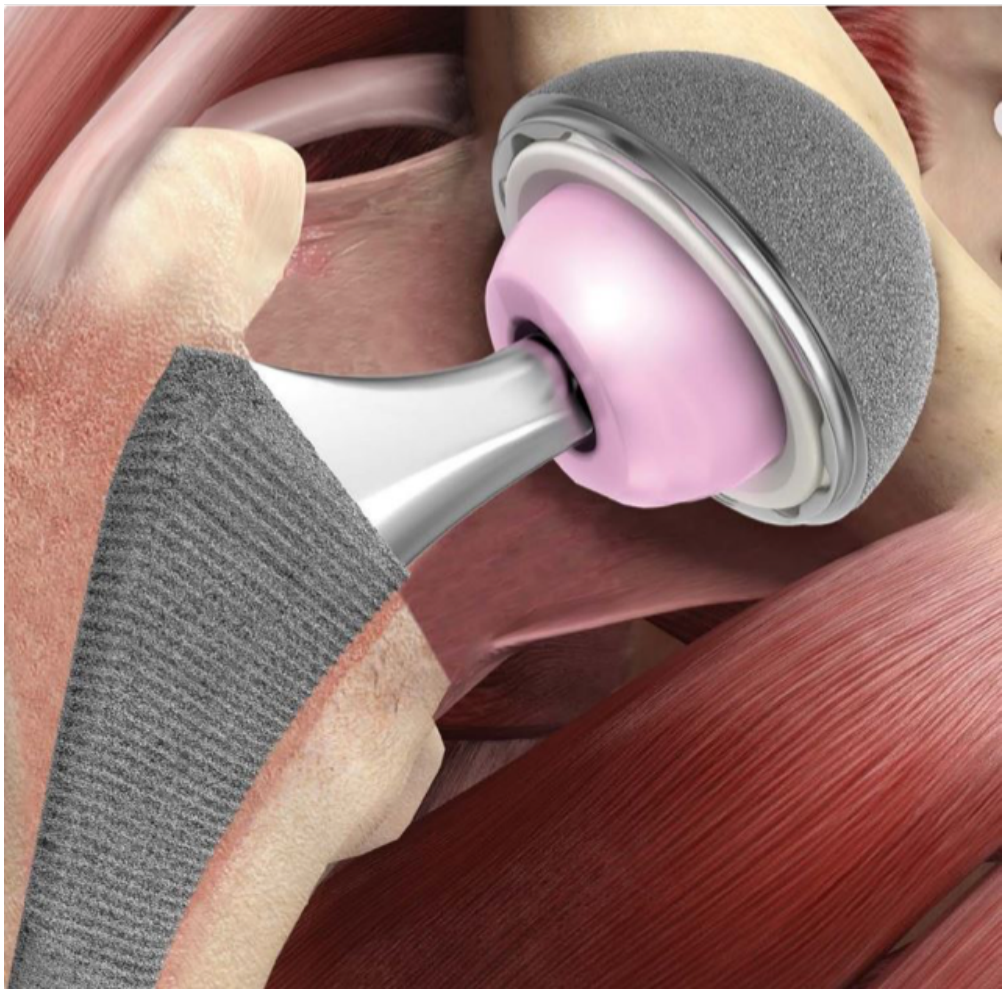

Figure 5.2-1: A visual of the DePuy Sythes PINNACLE acetabular cup and SUMMIT tapered femoral head components implanted into a hip joint. A section view of the femur shows how the component stem is placed and both layers of the acetabular cup can be seen.

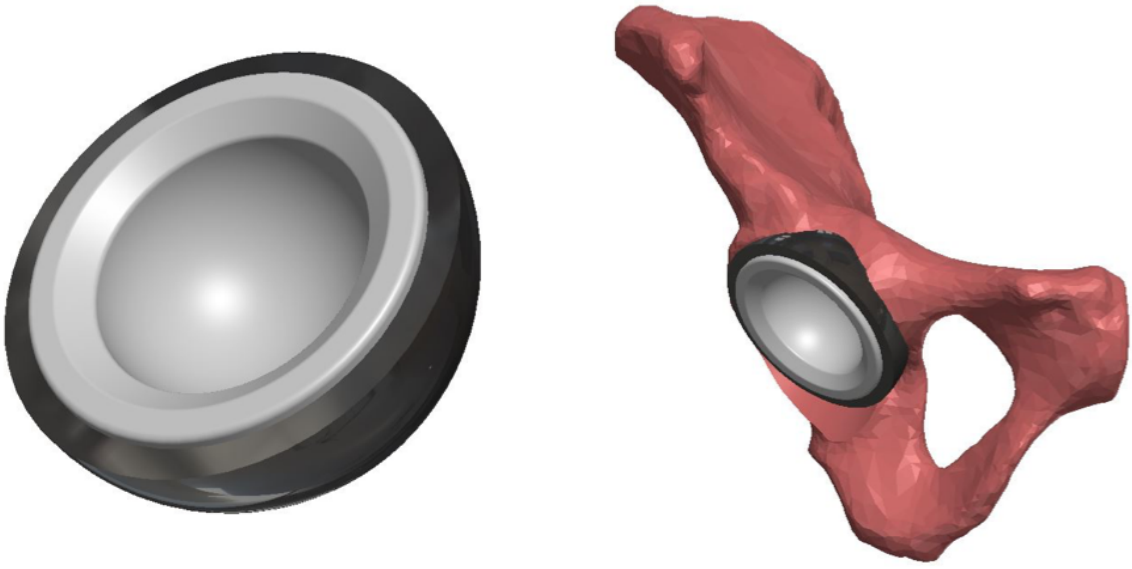

Figure 5.2-2: (Left) The acetabular cup as a stand-alone part. It was modeled as two separate parts in an attempt to match the true size and specifications as was is seen clinically. (Right) This cup was placed within the native acetabulum concentrically and then aligned according to the Lewinnek ranges for version and inclination.

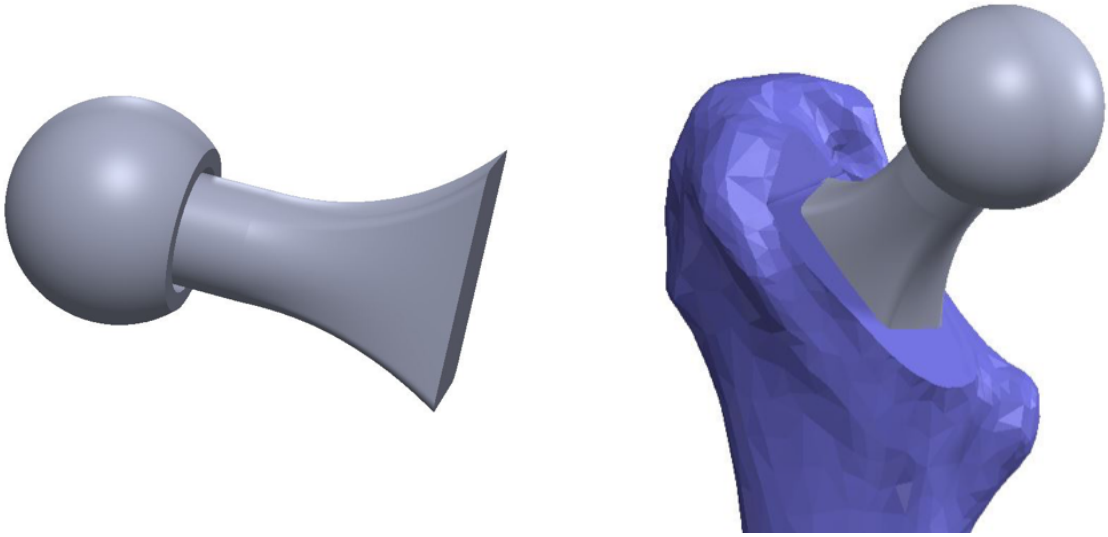

Figure 5.2-3: (Left) The femoral component alone. It consists of a spherical femoral head and an intricate neck that forms from a simple cylinder to a rectangular base. The specifications are based upon a typical implant. (Right) The femoral component placed within the native femur used in this model.

With the parts created according typical specifications, they were implemented within the previously validated model similarly to what is done clinically. Initially, the acetabular cup was arranged according to the Lewinnek averages for inclination ($40 \pm 10°$) and anteversion ($15 \pm 10°$) [124]. This cup was placed with the assumption that it would be concentric with the native acetabular cup providing a point of rotation and allowing for simple manipulation to ensure proper alignment. Prior to implementing the femoral component, the native neck and head anatomy were removed to provide a location for the implant. A point of rotation for altering the inclination and version was defined based on the native shaft axis and neck axis. This provided an initial position for the implant while also considering the need for future manipulation with the primary desire being how these femoral anteversion, and thus combined version, affect kinematics. Typically, femoral version is used to reach a target CV and there is an inconsistency within the literature as to what an ideal range should be. As mentioned previously, reported values range from 25–60° and so three values in this range were selected. 35°, 45° and 55° of combined version were used making the femoral anteversion 20°, 30° and 40° (Figure 5.2-4) with acetabular anteversion set to 15°. Femoral inclination was set to 130° for each model (Figure 5.2-5).

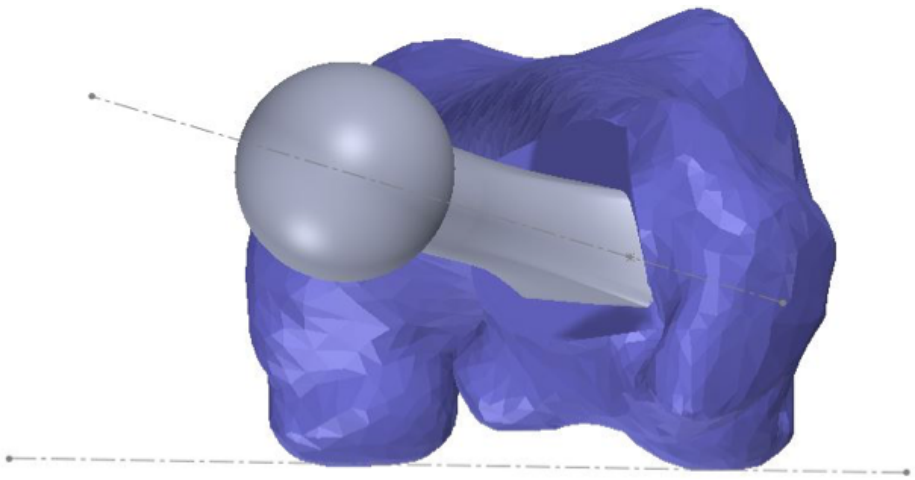

Figure 5.2-4: Femoral version is based upon the femoral condylar axis and the femoral neck axis. This image displays each of these axes within the transverse plane with regards to the THA models.

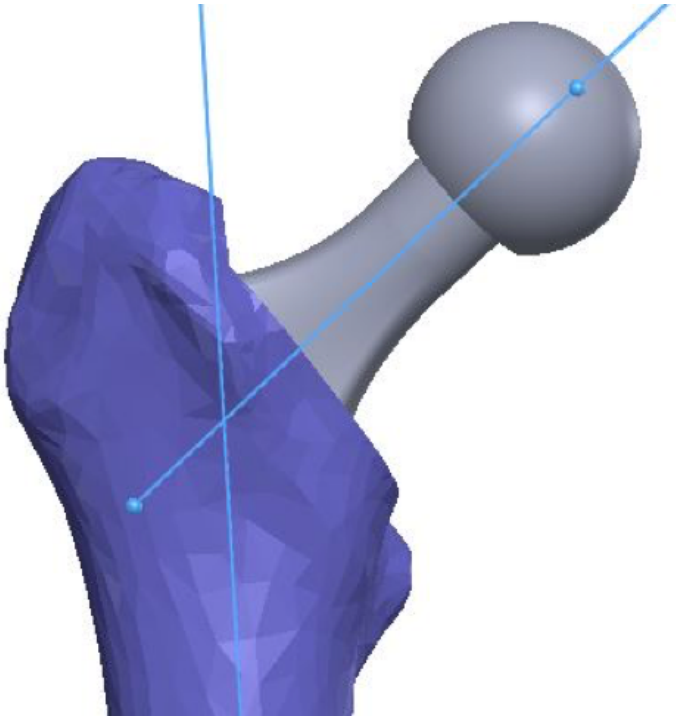

Figure 5.2-5: Inclination describes the neck relationship with the femoral shaft. This image displays the inclination relationship in the frontal plane used in the models.

5.2.2 Data Analysis

Similar to the FAI model, kinematic data output from this SolidWorks RBM model was read and analyzed with a custom Matlab script (Appendix A). The same lengths and calculations done on the healthy and FAI models for determining joint angles were performed on the THA models. Again, plots displaying kinematic angles with regards to STS percentage for both healthy and THA data and plots with the difference magnitudes throughout the motion for each THA model relative to the healthy models were created. Root mean square deviation (RMSD) values for each model relative to the respective healthy model were calculated as a way to provide a quantification of their relationship. If unstable motion or a dislocation occurred, there was further investigation on that particular model or version angle.

5.3 Results

Kinematic data for all three models was plotted to directly compare motion for healthy with the three different THA combined version angles (Figure 5.3-1). THA created a significant alteration in the kinematics when compared to the initial healthy state for all three models. Both the models with 45° of CV and the models with 55° of CV had the same trend for each case with a lower peak pelvic tilt angle and a sharp, quick pelvic extension motion during the lift-off phase. The pelvis tilt angle continued to decrease even after reaching the target neutral position to values that would suggest an un-physiological position. On the other hand, all three models provided with 35° of CV experienced dislocation. Further investigation showed that this dislocation did not occur due to an impingement-type abutment between the neck and acetabular cup (Figure 5.3-2). The precise time of this dislocation was apparent in the kinematics plots as a slight spike in pelvic tilt angles leading to a sharp decline to a point past the neutral 0° whereas the other two cases have a more gradual shift to this decline. In the knee joint, all models displayed similar knee flexion angles to the healthy model during the pelvic tilt phase. However, during the lift-off phase, rate of knee extension for all models began to rapidly increase to its target position including the models where dislocation occurred. This observation was unanimous between all three validated models.

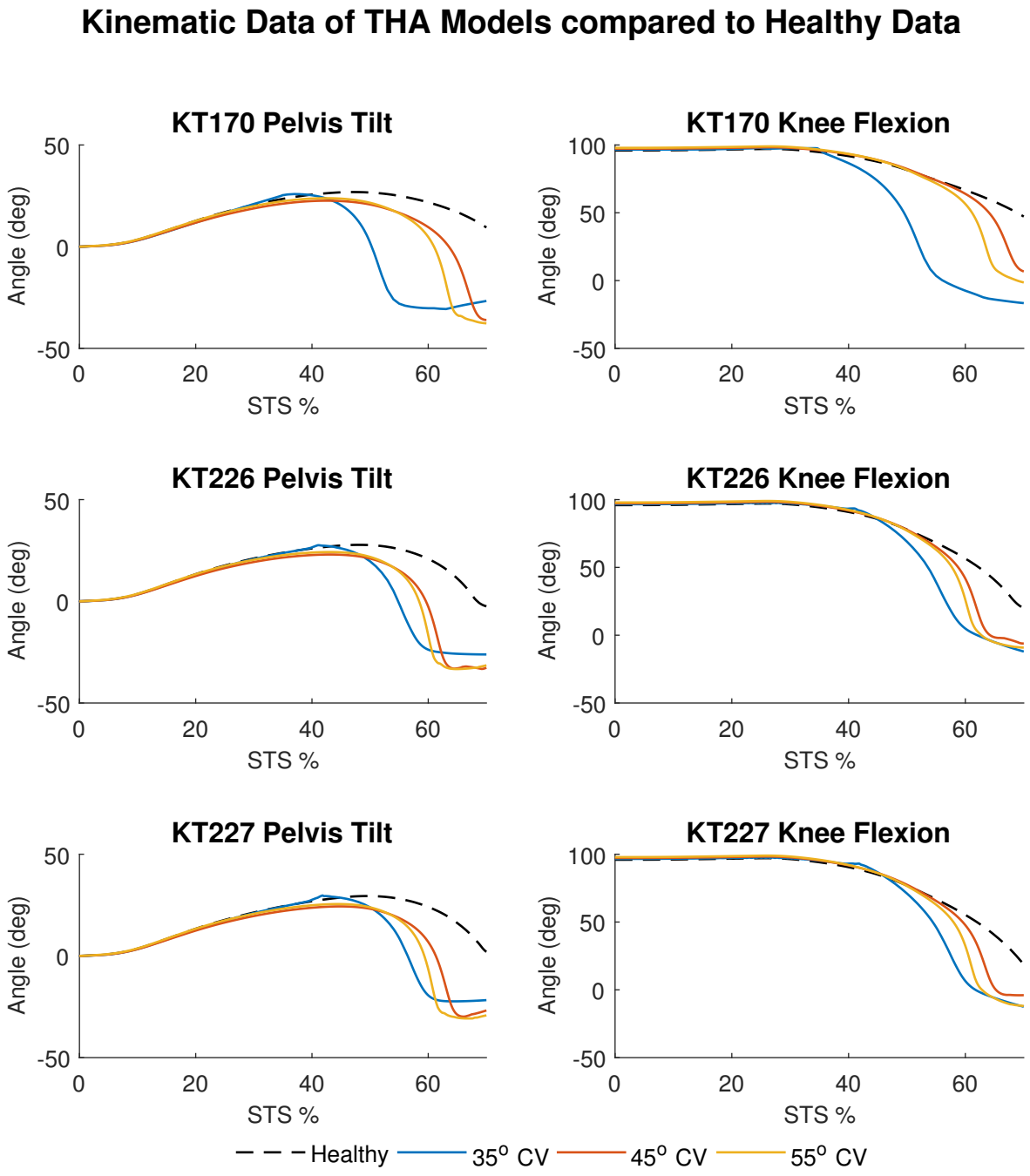

Figure 5.3-1: Plots comparing all three healthy models with their respective THA models. The THA models were altered to have 35° (blue), 45° (red) and 55° (yellow) degrees of combined version. For each model with 35° of CV, there is a slight spike in the hip motion at the time of dislocation.

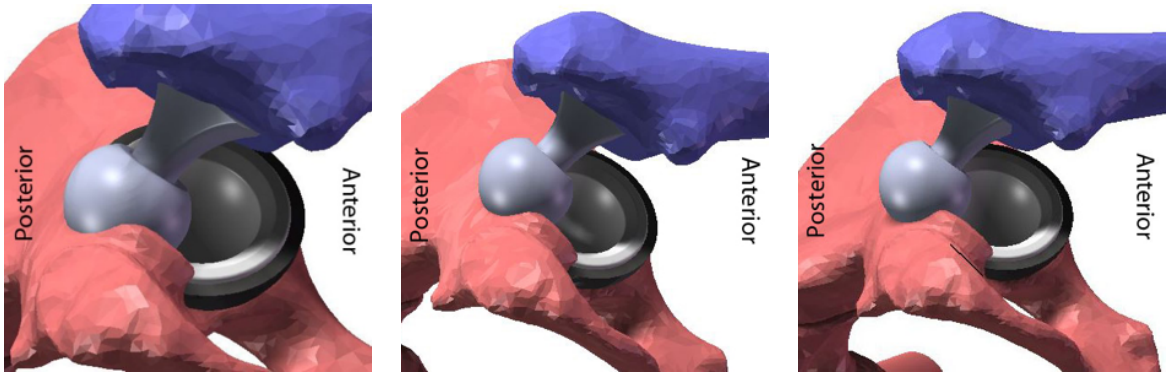

Figure 5.3-2: Inferior views at the time of dislocation for each model provided with 335° of CV. (Left) Model KT170, (Center) Model KT226 and (Right) Model KT227. All of these occur late into the pelvic tilt phase.

The magnitude difference between each THA model and their respective healthy model was plotted with areas of interest highlighted such as peak and initial deviation (Figure 5.3-3, Table 5.3-2). Unanimously, pelvis tilt motion began to differ from the healthy data for each THA model, regardless of CV angle, early in the motion with an average initial point of variation of 5.6% STS. Knee flexion did not change much until the lift-off phase initiated apart from cases with 35° CV due to the general lack of femur motion early in a STS transfer. On average, models with 35° of CV started to differ in knee motion at around 28.6% STS whereas models with 45° or 55° of CV remained similar to the experimental knee motion until 54.3% STS. Maximum deviation for all THA models was large for both pelvis tilt and knee flexion and occurred well into the lift-off phase of STS. All FAI models, regardless of CV angle, varied by a great deal during this phase (Figure 5.3-4). These high amounts of deviation for each THA model were further quantified through RMSD values (Table 5.3-1) wherein all models showed high amounts of deviation.

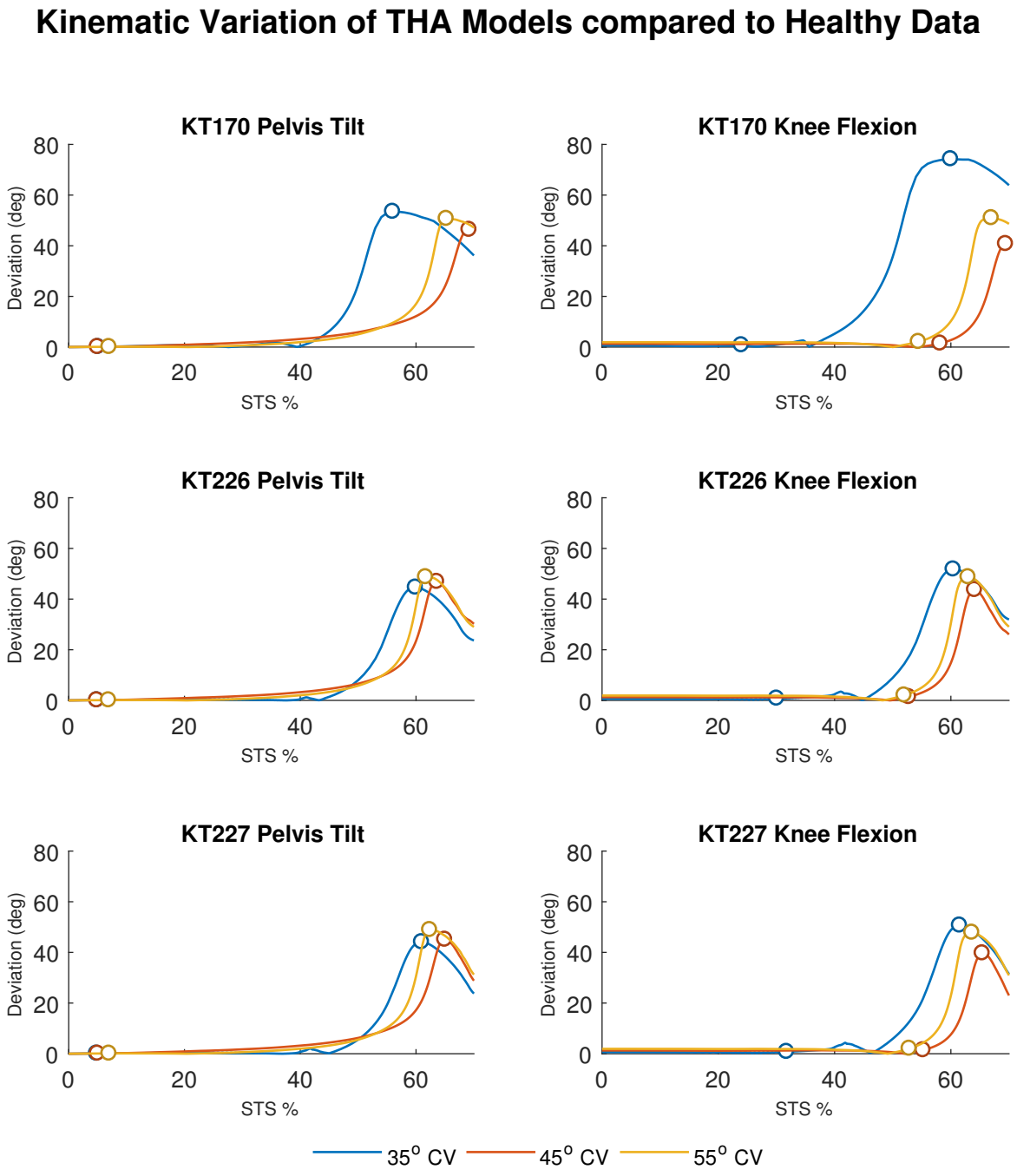

Figure 5.3-3: Plots showing the difference magnitude between the healthy models and THA models for 35° (blue), 45° (red) and 55° (yellow) degrees of combined version.

Model		Pelvis Tilt RMSD (°)	Knee Flexion RMSD (°)
KT170	35° CV	16.0	23.4
	45° CV	12.0	8.6
	55° CV	17.0	16.0
KT226	35° CV	18.5	22.0
	45° CV	15.7	13.4
	55° CV	17.3	16.7
KT227	35° CV	17.9	20.9
	45° CV	14.6	11.5
	55° CV	17.3	16.3

Table 5.3-1: The root mean square values for each variation of THA model compared with its respective healthy model.

		Pelvic Tilt			Knee Flexion		
		Initial Variation	Maximum Variation		Initial Variation	Maximum Variation	
Model		%STS	%STS	Diff Mag (°)	%STS	%STS	Diff Mag (°)
KT170	35° CV	5.1	56.0	53.5	24.0	53.5	56.0
	45° CV	5.0	69.2	46.4	58.2	69.5	40.8
	35° CV	7.0	65.3	50.7	54.5	67.0	51.0
KT170	35° CV	4.9	59.9	44.6	30.1	60.4	51.8
	45° CV	4.9	63.6	46.9	52.8	64.1	43.6
	35° CV	6.9	61.7	48.7	52.0	63.0	48.7
KT170	35° CV	4.8	61.0	44.1	31.8	61.5	50.7
	45° CV	5.0	65.0	45.1	55.3	65.4	39.7
	35° CV	7.0	62.4	48.9	52.9	63.7	47.9

Table 5.3-2: Highlighted points of variation between the three validated healthy models and their respective variations of THA models. The %STS for initial variation in addition to the %STS and magnitude of maximum variation are included for all THA models. Point of initial variation indicates the point where the magnitude difference between healthy and FAI models is greater than 0.1 degrees. As each value was rounded to a single decimal point, variation greater than 0.1 provides a numerical indication of this variation seen in the rounded results.

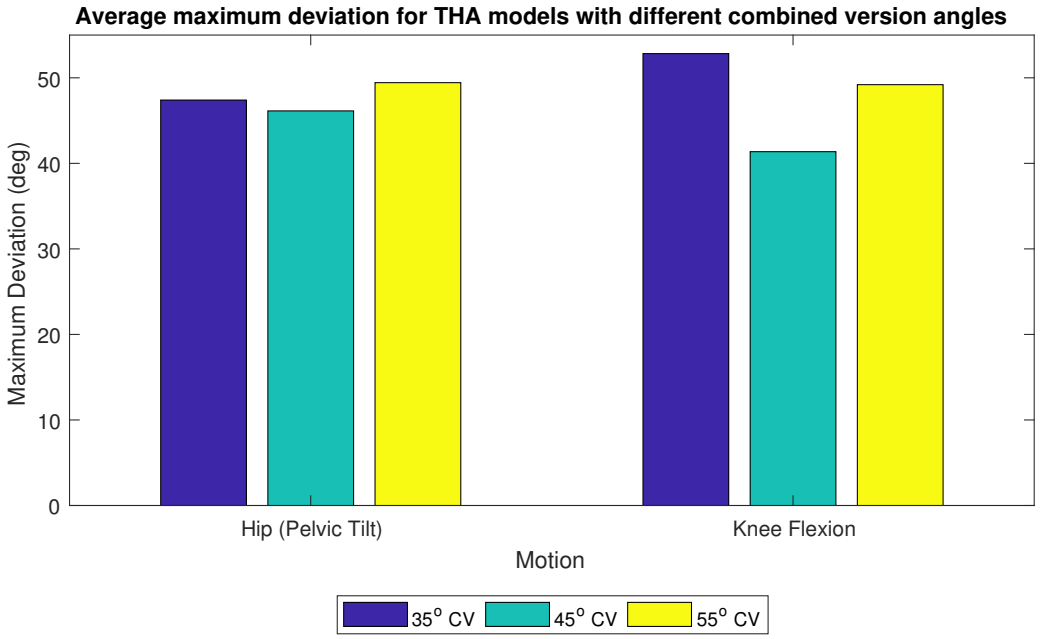

Figure 5.3-4: The average maximum deviation from healthy motion for the three different femoral version angles for both hip and knee motion.

5.3.1 Discussion

This study took advantage of the previously discussed and validated STS computational models to investigate the wide range of acceptable combined version angles in a THA procedure using postoperative kinematics. The three healthy model variations, differing only in their applied muscle forces, were provided with a complete THA procedure starting with resection of the native anatomy and then accurate placement of the parts compliant with what is done clinically. All soft tissue structures, except the labrum, were left intact exactly as they were in the healthy models to maintain consistency. Typically, when using a cement fixation, the acetabular component is placed first according to a previously established range developed by G. E. Lewinnek in 1978 for both version and inclination. Femoral anteversion is then implemented to provide an ideal combined version. There is inconsistency as to what

this combined version should be in the literature with different sources suggesting different ranges varying from $25 - 60^{\circ}$ of CV. This aspect was tested during this study. With regards to kinematics and biomechanics in general, a common indicator of a failed THA procedure is dislocation of the femoral head from the acetabular socket [119].

Up until now, there have not been any studies comparing THA combined version with STS kinematics. A postoperative kinematic study was performed by Lamontagne et al (2012) to provide a general indication of how patients (n=20) performed sit-to-stand and stand-to-sit tasks postoperatively, independent of combined version angles, and did find that hip flexion was lower for most of the motion compared with the control participants. The component placement measurements were not reported in the study [128]. Results from the computational models in this thesis show similar trends through reduced pelvic tilt angles and further expanded the investigation to include the effect of anteversion angles. All models with THA, regardless of their CV angle, showed an alteration in kinematics when compared with the native healthy model with this lower peak pelvic tilt angle and a faster rise to a standing position (Figure 5.3-1). Degree or amount of deviation from the healthy models further suggests that all three combined version angles differed drastically from their respective healthy models with the high root mean square deviation values reported making it difficult to refine the range of acceptable CV angles with this data alone. RMSD for all but one case in both pelvic tilt and knee flexion was above 10° with the average maximum deviation being above 40°. Most of this variance occurred during the lift-off phase which was also an area of concern during the validation phase.

The models with 35° of CV experienced a posterior dislocation during the pelvic tilt phase. However, this dislocation did not occur as a result of an impingement situation but rather due to a lack of coverage posteriorly (Figure 5.3-2). This is unusual as posterior dislocations, regardless of CV angle, typically occur as a result of anterior impingement forming a lever-type release of the femoral head component [119, 125]. Postoperative hip

abductor deficiency is a rare situation that has resulted in cases of instability with THA procedures and, as these muscles were not included in the original healthy model, could be a cause of this finding [129]. Hip abductors help in maintaining hip stability for THA by providing a force that prevents lateral motion of the femoral head relative to the cup. Further testing on this situation should be performed.

Potential sources for error include all areas mentioned in both Chapter 3 and 4. As a RBM study, this model required simplifications and compromises with all soft tissue structures. A combination of rigid body elements and linear force vectors were combined to develop these tissues. With the diverse range of motion seen in the hip joint, many different positions and the resulting muscle line of action had to be considered. Finally, the assumption that muscle weakness and surrounding tissue damage does not occur as a result of the THA procedure was made to maintain consistent applied forces between these models and their healthy comparison. Regardless, these THA models successfully provided information as to how the kinematics change with respect to different combined version angles and created a foundation for defining a more consistent combined version target range. This information could prove to be useful for providing more successful total hip arthroplasty procedures and lower the potential for revision surgeries.

Chapter 6: Conclusion

The work in this thesis applied computational techniques to study common pathological situations experienced in the hip joint throughout the frequently performed task of sit-to-stand. An anatomically accurate three-dimensional rigid body model of the lower extremity was developed using parts derived from CT scans. Soft tissue structures were incorporated, according to insertion sites reported in literature, as a series of linear force vectors aligned to match the line of action or fiber orientation for their respective tissue. Each tissue was programmed according to its native physiological function with ligaments provided tension only properties based upon stiffness and strain while muscles generated the necessary moments to create the desired motion. Magnitudes and properties for each of these were gathered from literature. This model went through an indirect validation using results from a former experimental study by Burnfield et al [91] to match both pelvic tilt and knee flexion angles throughout the motion. Using a threshold root mean square error value of 5°, three different models, differing slightly in applied muscle force magnitudes, were chosen to proceed forward.

The hip joint undergoes a wide range of both loading conditions and range of motion consequently leading to more many possible of pathological situations [32,70]. Femoroacetabular impingement (FAI) and total hip arthroplasties (THA) are both common morphological states experienced with hip joints today. FAI occurs with a region of overgrowth in the anterior femoral neck and head leading to painful situations involving extreme hip flexion and can cause chronic tissue pain from repetitive incidents of unusual contact [7,30,31,40]. THA is the most common corrective procedure for patients diagnosed with degenerative joint disease (DJD), or osteoarthritis (OA), which is a painful loss of articular tissue that occurs with age [32, 35, 119]. Both of these cases are common morphologies and lower extremity kinematics could potentially be affected by and contribute to the issues with both cases and

thus were the focal point of this thesis. The three previously mentioned validated models were modified to include both FAI and THA conditions based upon the current standard for quantifying their morphology. For FAI, a single case, representing the average patient presenting with symptomatic cam-type impingement, was studied by implementing the reported average alpha angle value to the femoral head and neck on each of the three models. THA component placement is quantified via four different angles describing orientation of either component in both the frontal (acetabular inclination and femoral inclination) and transverse (acetabular anteversion and femoral anteversion) planes. Combined version provides an indication of how both parts are oriented within the transverse place and there is an inconsistency as to what this value should be with literature ranging from 25–60° [119]. Combined version was set to 35°, 45°, and 55°, all of which fall within this range, for investigating THA in all three validated models. Acetabular anteversion remained constant at 15° for every model making femoral anteversion the determining factor that changed between each model.

It is well understood that FAI is not a pathology that results in a sudden onset of symptoms but rather a gradual increase in symptoms over time with repetition [31, 103]. The results from this work support that conclusion in that there were only slight deviations between kinematics and contact between healthy and FAI models. This brings about the question of whether the difference is due to the altered morphology or to assumptions made during model development. Aside from the magnitudes of contact, the actual location of contact occured more posteriorly for every model, both heathy and FAI, without any anterior contact between the femoral neck and labrum occurring. Typically, FAI causes discomfort in the anterior region of the hip joint during the upper limits of hip flexion. During a deep squat, it was observed that patients with FAI reported, on average, approximately 6.4° less of peak hip flexion compared with healthy patients [7]. However, average peak hip flexion reported for these FAI patients was still approximately 8.6° greater than the peak

hip flexion measured by the models used in this thesis which showed no difference in hip flexion between FAI and healthy cases (Figure 4.3-3). With regards to contact, there were slight increases in contact for FAI models relative to healthy models but this was located in the posterior region of the acetabular cartilage. There was no observed contact or significant labrum tension developed in the anterior region that would be indicative of unusual abutment between femur and acetabulum. Therefore, it can be said that the motion of STS may not provide traumatic enough conditions of hip flexion for cam-type impingement to induce an effect on the kinematics.

Proper placement of the different parts in a THA procedure plays a crucial role in the patient's ability to perform motions as well as in the decreasing the probability of dislocation. The three different CV cases mentioned previously were successfully implemented into the three validated STS models. Kinematics of the THA models did have a significant change from the respective healthy models regardless of the CV angle with the cases of 35° CV dislocating. Each incidence of dislocation occurred approximately at the point of peak pelvic tilt suggesting that this increase in hip flexion provided instability with this combination of anteversion and inclination angles. Further investigation into this dislocation showed that it was due to a lack of coverage posterior with the head simply slipping out (Figure 5.3-2), contradicting what is typically observed clinically with posterior dislocation occurring as a result of anterior impingement between the neck and cup [119, 130]. It is possible for posterior dislocation to occur in situations of hip capsular or hip abductor weakness as a result of a posterior surgical approach but capsular strength was maintained constant between healthy and THA models [129, 130]. Regardless, based upon these results, the combined version should be on the higher end of the literature ranges with both 45° and 55° CV cases successfully completing the STS task, even with a different motion than their healthy states. This statement should be further investigated to include the hip abductor muscles for confirmation. Considering the inconsistency in literature as to what this angle

should be, these results provide information to potentially develop a more definitive CV range able to reduce the amount of dislocations experienced.

As this is the first attempt at developing a model that accurately represents a sit-to-stand transfer, future uses of this model should attempt to improve representation of the healthy state compared to literature. Additional musculature for control could be implemented as well as including more samples of experimental data during the validation phase. By accounting for the inherent variation that occurs between individuals in STS and increasing the sample size, more confidence can be developed in the results gathered from this model. In addition, implementation of the talocrural (ankle) joint would permit full 100% STS by allowing for rotation of the tibia and fibula to achieve full 100% validation rather than limiting to only 70% of the motion. This would increase the complexity along with the potential for error but, if successful, would allow for a more accurate representation of what occurs in-vivo. All work in this thesis focused primarily on femoral morphology. Situations of pincer-type FAI and improper acetabular cup placement with THA could be easily investigated with this model providing information with regards to how acetabular morphology affects STS. Regardless, this model was able to provide insight into areas that either cannot be investigated or would be difficult and require expensive equipment to investigate experimentally. It has shown to be a useful tool in understanding different situations of STS in its initial form and further work to improve the validation will only increase its ability to contribute to our understanding of hip pathologies and how they ultimately affect this commonly performed motion.

References

[1] S. H. Weinberg, D. B. Mair, and C. A. Lemmon. Mechanotransduction dynamics at the cell-matrix interface. *Biophysical Journal*, 112:1962–1974, 2017.

[2] H. Babhosseini, B. Carmichael, J. S. Strobl, and M. Agah. Sub-cellular force microscopy in single normal and cancer cells. *Biochemical and Biophysical Research Communication*, 463:587–592, 2015.

[3] Q. Guo, S. P. Duffy, M. Kerryn, A. T. Santoso, M. D. Scott, and H. Ma. Microfluidic analysis of red blood cell deformability. *Journal of Biomechanics*, 47:1767–1776, 2014.

[4] Y.C. Fung. *Biomechanics: Mechanical Properties of Living Tissues*, volume 2. Springer, 1993.

[5] A. Krishnamurthy, C. T. Villongco, J. Chuang, L. R. Frank, V. Nigam, E. Belezzuoli, P. Stark, D. E. Krummen, S. Narayan, J. H. Omens, A. D. McCulloch, and R. C. P. Kerckhoffs. Patient-specific models of cardiac biomechanics. *Journal of Computational Physics*, 244:4–21, 2013.

[6] J. Kim, R. L. Heise, A. M. Reynolds, and R. M. Pidaparti. Aging effects on airflow dynamics and lung function in human bronchioles. *PLoS ONE*, 12, 2017.

[7] J.J. Bagwell, J. Snibbe, M. Gerhardt, and M. C. Powers. Hip kinematics and kinetics in persons with and without cam femoroacetabular impingement during a deep squat task. *Clinical Biomechanics*, 231:87–92, 2015.

[8] M.J. Kennedy, M. Lamontagne, and P.E. Beaule. Femoroacetabular impingement alters hip and pelvic biomechanics during gait: Walking biomechanics of fai. *Gait and Posture*, 30:41–44, 2009.

[9] I.D. Hutchinson, J.R. Baxter, S. Gilbert, M.V. Hogan, S.M. Saunders J. Ling, H. Want, and J.G. Kennedy. How do hindfoot fusions affect ankle biomechanics: A cadaver model. *Clinical Orthopedics and Related Research*, 474:1008–1016, 2015.

[10] R.M. Mardones, C. Gonzalez, Q. Chen, M. Zobitz, K.R. Kaufman, and R.T. Trousdale. Surgical treatment of femoroacetabular impingement: Evaluation of the effect of the size of the resection. *Journal of Bone and Joint Surgery*, 87A:273–279, 2005.

[11] J.G. Galbraith, C.J. Daly, J.A. Harty, and H. L. Dailey. Role of the fibula in the stability of diaphyseal tibial fractures fixed by intramedullary nailing. *Clinical Biomechanics*, 38:42–49, 2016.

[12] J.D. Hewitt, R.R. Glisson, F. Guilak, and T.P. Vail. The mechanical properties of the human hip capsular ligaments. *The Journal of Arthroplasty*, 17:82–89, 2002.

[13] M.J. Crawford, C.J. Dy, J.W. Alexander, M. Thompson, S.J. Schroder, C.E. Vega, R.V. Patel, A.R. Miller, J. McCarthy, W.R. Lowe, and P. C. Noble. The biomechanics of the hip labrum and the stability of the hip. *Clinical Orthopedics and Related Research*, 465:16–22, 2007.

[14] M.G. Pandy. Computer modeling and simulation of human movement. *Annual Review of Biomedical Engineering*, 3:245–273, 2001.

[15] H.B. Henninger, S.P. Reese, A.E. Anderson, and J.A. Weiss. Validation of computational models in biomechanics. *Proceedings of the Institution of Mechanical Engineers, Part H*, 224:801–812, 2010.

[16] J.N. Reddy. *An Introduction to the Finite Element Method*.

[17] R.C. Henak, G.A. Ateshian, and J.A. Weiss. Finite element prediction of transchondral stress and strain in the human hip. *Journal of Biomechanical Engineering*, 136, 2014.

[18] V.C. Mow, L.A. Setton, F. Guilak, and A. Ratcliffe. Mechanical factors in articular cartilageand their role in osteoarthritis. *American Academy of Orthopedic Surgeons*, 1995.

[19] A.R. Poole. Imbalances of anabolism and catabolism of cartilage matrix components in osteoaritis. *American Academy of Orthopedic Surgeons*, 1995.

[20] A.E. Anderson, B.J. Ellis, S.A. Maas, and J.A. Weiss. Effects of idealized joint geometry on finite element predictions of cartilage contact stresses in the hip. *Journal of Biomechanics*, 43:1351–1357, 2010.

[21] MSC Software Corp. Adams solver user's guide. 2006.

[22] B.A. Smith, R.S. Adelaar, and J.S. Wayne. Patient specific computational models to optimize surgical correction for flatfoot deformity. *Journal of Orthopedic Research*, 2016.

[23] E.J. Tremols. Design and validation of a computational model for study of scapholunate joint kinematics. *Dissertation*, 2012.

[24] E.M. Spratley and J.S. Wayne. Computational model of the human elbow and forearm: Application to complex varus instability. *Annals of Biomedical Engineering*, 39:1084–1091, 2011.

[25] E.M. Spratley, E.A. Matheis, C.W. Hayes, R.S. Adelaar, and J.S. Wayne. Validation of a population of patient-specific adult acquired flatfoot deformity models. *Journal of Orthopedic Research*, pages 1861–1868, 2013.

[26] Musculographics Inc. Simm. `http://www.musculographics.com/html/products/SIMM.html`. 2016 (accessed March 2017).

[27] A.J. van den Bogert, L. Read, and B.M. Nigg. An analysis of hip joint loading during walking, running, and skiing. *Medicine & Science in Sports & Excercise*, 31:131–142, 1999.

[28] G.J. Farkas, G.L. Cvetanovich, K.B. Rajan, A.A. Espinoza, and S.J. Nho. Impact of femoroacetabular impingement morphology on gait assessment in symptomatic patients. *Sports Health*, pages 429–436, 2015.

[29] S.W. Mayer, J.C.M. Abdo, M.K. Hill, L.A. Kestel, Z. Pan, and E.N. Novais. Femoroacetabular impingement is associated with sports-related posterior hip instability. *American Journal of Sports Medicine*, 2016.

[30] H.D. Martin, A. Savage, B.A. Braly, I.J. Palmer, D.P. Beall, and B. Kelly. The function of the hip capsular ligaments: A quatitative study. *The Journal of Arthroscopic and Related Surgery*, 24:188–195, 2008.

[31] M. Tannast, D. Goricki, M. Beck, S. Murphy, and K. Siebenrock. Hip damage occurs at the zone of femoroacetabular impingement. *Clinical Orthopedics and Related Research*, 466:273–280, 2008.

[32] M. Beck, M. Kalhor, M. Leunig, and R. Ganz. Hip morphology influences the pattern of damage to the acetabular cartilage. *Journal of Bone and Joint Surgery*, 87B:1012–1018, 2005.

[33] L. Ejnisman, N.Z. Leonhardt, L.F.L. Fernandes, M.D.C. Leonhardt, J.R.N. Vicente, and A.T. Croci. Comparison of total hip arthroplasty in osteoarthritis of mechanical and rheumatologic causes. *Acta Orthopedica Brasileira*, 22:38–42, 2014.

[34] S.D. Steppacher, J.H. Kowal, and S.B. Murphy. Improving cup positioning using a mechanical navigation instrument. *Clinical Orthopedics and Related Research*, 469:423–428, 2014.

[35] J.T. Moskal and S.G. Capps. Acetabular component positioning in total hip arthroplasty: An evidence-based analysis. *The Journal of Arthroplasty*, 26:1432–1437, 2011.

[36] JK.T. Suh, J.H. Kang, H.L. Roh, K.P. Moon, and H.J. Kim. True femoral anteversion during primary total hip arthroplasty: Use of postoperative computed tomography-based sections. *The Journal of Arthroplasty*, 21:599–605, 2006.

[37] L. Cerezal, J. Arniaz, A. Canga, T. Piedra, J.R. Altonaga, R. Munafo, and L. Perez-Carro. Emerging topics on the hip: Ligamentum teres and hip microinstability. *European Journal of Radiology*, 81:3745–3754, 2012.

[38] F.K. Fuss and A. Bacher. New aspects of the morphology and function of the human hip joint ligaments. *The American Journal of Anatomy*, 192:1–13, 1991.

[39] V. Sanchis-Alfonso, M. Tey, and J.C. Monllau. A novel association between femoroacetabular impingement and anterior knee pain. *Pain Research and Treatment*, 2015.

[40] M.A. Hunt, J.R. Gunether, and M.K. Gilbart. Kinematic and kinetic diferences during walking in patients with and without symptomatic femoroacetabular impingement. *Clinical Biomechanics*, 28:519–523, 2013.

[41] K.D. Huffman, B.A. Sanford, A.R. Zucker-Levin, J.L. Williams, and W.M. Mihalko. Increased hip abduction in high body mass index subjects during sit-to-stand. *Gait and Posture*, 41:640–645, 2015.

[42] N. Vusirikala. Development of human hip capsule finite element model. *Injury Biomechanics Research*.

[43] J.A. Weiss, C.R. Henak, B.J. Ellis, M.D. Harris, A.E. Anderson, and C.L. Peter. Role of the acetabular labrum in load support across the hip joint. *The Journal of Biomechanics*, 44:2201–2206, 2011.

[44] F. Vallon, A. Reymond, P. Furnstahl, P.O. Zingg, A.F. Kamath, J. Snedeker, and C. Dora. Effect of angular deformities of the proximal femur on impingement-free hip range of motion in a three-dimensional rigid body model. *Hip International*, 25:574–580, 2015.

[45] E.J. Caruthers, J.A. Thompson, A.M. Chaudhari, L.C. Schmitt, T.M. Best, K.R. Saul, and R.A. Siston. Muscle forces and their contributions to vertical and horizontal acceleration of the center of mass during sit-to-stand transfer in young, healthy adults. *Journal of Applied Biomechanics*, 32:487–503, 2016.

[46] L. Ren, R.K. Jones, and D. Howard. Whole body inverse dynamics over a complete gait cycle based only on measured kinematics. *Journal of Biomechanics*, 41:2750–2759, 2008.

[47] P.M. Dall and A. Kerr. Frequency of the sit to stand task: an observational study of free-living adults. *Applied Ergonomics*, 41:58–61, 2010.

[48] H.M. Kremers, D.R. Larson, C.S. Crowson, W.K. Kremers, R.E. Washington, C.A. Steiner, W.A. Jiranek, and D.J. Berry. Prevalence of total hip and knee replacement in the united states. *The Journal of Bone and Joint Surgery*, pages 1386–1397, 2015.

[49] P. de Leva. Adjustments to zatsiorsky-seluyanov's segment inertia parameters. *Journal of Biomechanics*, 29:1223–1230, 1996.

[50] R.E. Steldt and B.D. Schmidt. Modulation of coordinated muscle activity during imposed sinusoidal hip. *The Journal of Neurophsyiology*, pages 673–685, 2004.

[51] J.J. Callaghan, A.G. Rosenberg, and H.G. Rubash. *The Adult Hip*. Lippincott-Raven: Philadelphia, PA, 1998.

[52] K.F. Bowman, J. Fox, and J.K. Sekiya. A clinically relevant review of hip biomechanics. *Arthroscopy*, 26:1118–1129, 2010.

[53] Dorland. *Dorland's illustrated medical dictionary*. Saunders/Elsevier: Philadelphia, PA, 2011.

[54] J. Hall. *Guyton and Hall textbook of medical physiology*. Saunders/Elsevier: Philadelphia, PA, 12 edition, 2011.

[55] N.S. Eftekar. *Total Hip Arthroplasty*. Mosby, 1993.

[56] M.C. Lee and C.P. Eberson. Growth and development of the child's hip. *Orthopedic Clinics of North America*, 37:119–132, 2006.

[57] A. Dimeglio. Growth in pediatric orthopedics. *Journal of Pediatric Orthopedics*, 21:549–555, 2001.

[58] K.E. Roach and T.P. Miles. Normal hip and knee active range of motion: the relationship to age. *Physical Therapy*, 71:656–665, 1991.

[59] C.C. Norkin. *Measurement of joint motion: A guide to goniometry*. F.A. Davis Company: Philadelphia, PA, 2009.

[60] Wikipedia. Long bone. `https://en.wikipedia.org/wiki/Long_bone`. 18 April 2017 (accessed October 2017).

[61] H. Bouma, T. Hogervorst, E. Audenaert, and P. van Kampen. Combining femoral and acetabular parameters in femoroacetabular impingement: the omega surface. *Medical & Biological Engineering & Computing*, pages 1239–1246, 2015.

[62] S.K. Sarrafian. *Anatomy of the Foot and Ankle: Descriptive, Topographic, Functional*. J.B. Lippincott Company: Philadelphia, PA, 1993.

[63] A.M.R. Agur and A.F. Dalley. *Grant's Atlas of Anatomy*. Lippincott Williams & Wilkins, 2013.

[64] C.J. Stanley, A. Creighton, M.T. Gross, W.E. Garrett, and B. Yu. Effects of a knee extension constraint brace on lower extremity movements after acl reconstruction. *Clinical Orthopedics and Related Research*, 469:1774–1780, 2011.

[65] A.M. Bhosale and J.B. Richardson. Articular cartilage: structure, injuries and review of management. *British Medical Bulletin*, 87:77–95, 2008.

[66] M.J. Philippon, M.T. Rasmussen, T.L. Turnbull, C.A.C. Trindade, M.G. Hamming, M.B. Ellman, M. Harris, R.F. LaPrade, and C.A. Wijdicks. Structural properties of the native ligamentum teres. *The Orthopedic Journal of Sports Medicine*, 2, 2014.

[67] M.V. Smith, R.S. Costic, R. Allaire, P.L. Schilling, and J.K. Sekiya. A biomechanical analysis of the soft tissue and osseous constraints of the hip joint. *Knee Surgery, Sports Traumatology, Arthroscopy*, 22:946–952, 2011.

[68] C.S. Ranawat and M.J. Maynard. Modern technique of cemented total hip arthroplasty. *Techniques in Orthopedics*, 6:17–25, 1991.

[69] F.V. Wagner, J.R. Negrao, J. Campos, S.R. Ward, P. Haghighi, D.J. Trudell, and D. Resnick. Capsular ligaments of the hip: Anatomic, histologic, and positional study in cadaveric specimens with mr arthrography. *Radiology*, 263:189–198, 2012.

[70] A.S. Ranawat and B.T. Kelly. Anatomy of the hip: Open and arthroscopic structure and function. *Operative Techniques in Orthopedics*, pages 160–174, 2005.

[71] D. Nam, D.C. Osbahr, D. Choi, A. Ranawat, B.T. Kelly, and S.H. Coleman. Defining the origins of the iliofemoral, ischiofemoral, and pubofemoral ligaments of the hip capsuloligamentous complex utilizing computer navigation. *Hospital for Special Surgery Journal*, 7:239–243, 2011.

[72] K.J. Stewart, R.H. Edmonds-Wilson, R.A. Brand, and T.D. Brown. Spatial distribution of hip capsule structural and material properties. *Journal of Biomechanics*, 35:1491–1498, 2002.

[73] B.P. O'Hara, J.P. Urban, and A. Maroudas. Influence of cyclic loading on the nutrition of articular cartilage. *Annals of Rheumatic Diseases*, 49:536–539, 1990.

[74] J.T.A. Makela, M.R.J. Huttu, and R.K. Korhonen. Structure-function relationships in osteoarthritic human hip joint articular cartilage. *Osteoarthritis and Cartilage*, 20:1268–1277, 2012.

[75] F.S. Chen, S.R. Frenkel, and P.E. Di Cesare. Repair of articular cartilage defects: part i. basic science of cartilage healing. *American Journal of Orthopedics*, 28:31–33, 1999.

[76] G.E. Kempson, H. Muir, C. Polland, and M. Tuke. The tensile properties of the cartilage of human femoral condyles related to the content of collagen and glycosaminoglycans. *Biochimica et Biophysica Acta (BBA)*, 279:456–472, 1973.

[77] M. Venn and A. Maroudas. Chemical composition and swelling of normal and osteoarthritic femoral head cartilage. i. chemical composition. *Ann Rheum Dis*, 36:121–129, 1977.

[78] A. Maroudas, M.T. Bayliss, and M.F. Venn. Further studies on the composition of human femoral head cartilage. *Annals of Rheumatic Diseases*, 39:514–523, 1980.

[79] M.M. Groh and J. Herrera. A comprehensive review of hip labral tears. *Current Review in Musculoskeletal Medicine*, 2:105–117, 2009.

[80] S.J. Ferguson. Biomechanics of the acetabular labrum. *Dissertation*, 2000.

[81] S.J. Ferguson, J.T. Bryant, R. Ganz, and K. Ito. An in vitro investigation of the acetabular labral seal in hip joint mechanics. *Journal of Biomechanics*, 36:171–178, 2003.

[82] V. Tan, R.M. Seldes, and M.A. Katz. Contribution of acetabular labrum to articulating surface area and femoral head coverage in adult hip joints: An anatomic study in cadavera. *American Journal of Orthopedics*, 30:809–812, 2001.

[83] B.M. Koeppen and B.A. Stanton. *Kinesiology of the musculoskeleta system: Foundations for rehabilitation*, volume 6. Mosby Elsevier, 2010.

[84] S. Martelli, D. Calvetti, E. Somersalo, and M. Viceconti. Stochastic modeling of muscle recruitment activity. *Interface focus*, 2014.

[85] H.U. Kuriki, F.M. de Azevedo, L.S.O. Takahashi, E.M. Mello, R.F. Filho, and N. Alves. The relationship between electromyography and muscle force. *EMG Methods for Evaluating Muscle and Nerve Function*, pages 31–54, 2012.

[86] R. Khanmohammadi, S. Talebian, M.R. Hadian, and G. Olyaei. Characteristic muscle activity patterns during gait initiation in the healthy younger and older adults. *Gait & Posture*, 43:148–153, 2001.

[87] J. Wakeling, O. Blake, and H. Chan. Muscle coordination is key to the power output and mechanical efficiency of limb movements. *Journal of Experimental Biology*, 213:487–492, 2010.

[88] S. Yoshioka, A. Nagano, D.C. Hay, and S. Fukashiro. The minimum required muscle force for a sit-to-stand task. *Journal of Biomechanics*, 45:699–705, 2011.

[89] G. Wu, S. Siegler, P. Allard, C. Kirtley, A. Leardini, D. Rosenbaum, M. Whittle, D.D. D'Lima, L. Cristofolini, H. Witte, O. Schmid, and I. Stokes. Isb recommendation of definitions of joint coordinate system of various joints for the reporting of human joint motion - part i: ankle hip and spine. *Journal of Biomechanics*, 35:543–548, 2002.

[90] A.M. Hollister, S. Jatana, A.K. Singh, W.W. Sullivan, and A.G. Lupichuk. The axis of rotation of the knee. *Clinical Orthopedics and Related Research*, 290:259–268, 1993.

[91] J.M. Burnfield, Y. Shu, T.W. Buster, A.P. Taylor, M.M. McBride, and M.E. Krause. Kinematic and electromyographic analyses of normal and device-assisted sit-to-stand transfers. *Gait & Posture*, 36:516–522, 2012.

[92] R. Rose and K. Johnson-Throop. *NASA Man-Systems Integration Standards*. 2008.

[93] K. Turcot, S. Armand, D. Fritschy, P. Hoffmeyer, and D. Suva. Sit-to-stand alterations in advanced knee osteoarthritis. *Gait & Posture*, 36:68–72, 2012.

[94] P. Kumar, M. Oka, J. Toquichida, M. Kobayashi, E. Uchida, T. Nakamura, and K. Tanaka. Role of uppermost superficial surface layer of articular cartilage in the lubrication mechanism of joints. *Journal of Anatomy*, 199:241–250, 2001.

[95] E.L. Radin and I.L. Paul. A consolidated concept of joint lubrication. *Journal of Bone and Joint Surgery*, 54:607–613, 1972.

[96] M.G. Pandy, Y.-C. Lin, and H.J. Kim. Muscle coordination of mediolateral balance in normal walking. *Journal of Biomechanics*, 43:2055–2064, 2010.

[97] E. Hidaka, M. Aoki, T. Izumi, D. Suzuki, and M. Fukimiya. Ligament strain on the iliofemoral, pubofemoral, and ischiofemoral ligaments in cadaver specimens: Biomechanical measurement and anatomical observation. *Clinical Anatomy*, 27:1068–1075, 2014.

[98] G.A. Turley, M.A. Williams, R.M. Wellings, and D.R. Griffin. Evaluation of range of motion restriction within the hip joint. *Medical & Biological Engineering Computing*, 51:467–477, 2013.

[99] K. Elmore. Mechanical structures resisting anterior instability in a computational glenohumeral joint model. *VCU Scholars Compass*, 2009.

[100] E. Nikfekr, D. Playford, and S. Anfield. Kinematic analysis of the trunk motion during sit to stand in parkinson's disease. *Gait & Posture*, 10:76–77, 1999.

[101] Wikipedia. Root-mean-square-deviation. `https://en.wikipedia.org/wiki/Root-mean-square_deviation`. 2017 (accessed October 2017).

[102] M.A. Bredella, E.J. Ulbrich, D.W. Stoller, and S.E. Anderson. Femoroacetabular impingement. *Magnetic Resonance Imaging Clinics of North America*, 21:45–64, 2013.

[103] D.E. Martin and S. Trashman. The biomechanics of femoroacetabular impingement. *Operative Techniques in Orthopedics*, pages 248–254, 2010.

[104] D. Reynolds, J. Lucas, and K. Klaue. Retroversion of the acetabulum. a cause of hip pain. *Journal of Bone and Joint Surgery*, 81:281–288, 1999.

[105] C.V. Diesel, T.A. Ribeiro, C. Coussirat, R.B. Scheidt, C.A.S. Macedo, and C.R. Galia. Coxa profunda in the diagnosis of pincertype femoroacetabular impingement and its prevalence in asymptomatic subjects. *Bone and Joint Surgery*, 97:478–483, 2015.

[106] M. Leunig, S.J. Nho, L. Turchetto, and R. Ganz. Experience with joint preservation. *Clinical Orthopedics and Related Research*, 467:2241–2250, 2009.

[107] A.A. Zadpoor. Etiology of femoroacetabular impingement in athletes: A review of recent findings. *Sports Medicine*, 45:1097–1106, 2015.

[108] D.R. Sumner. Long-term implant fixation and stress-shielding in total hip replacement. *Journal of Biomechanics*, 48:797–800, 2015.

[109] L.L. Buchan, H. Zhang, S. Konan, I. Heaslip, C.R. Ratzlaff, and D.R. Wilson. Open-mri measures of cam intrusion for hips in an anterior impingement position relate to acetabular contact force. *Journal of Orthopedic Research*, pages 205–216, 2016.

[110] C.R. Henak, E.D. Carruth, A.E. Anderson, B.J. Ellis, C.L. Peters, and J.A. Weiss. Finite element predictions of cartilage contact mechanics in hips with retroverted acetabula. *Osteoarthritis Cartilage*, 10:1522–1529, 2013.

[111] A.L. Kapron, S.K. Aoki, C.L. Peters, and A.E. Anderson. Subject-specific patterns of femur-labrum contact are complex and vary in asymptomatic hips and hips with femoroacetabular impingement. *Clinical Orthopedics and Related Research*, 472:3912–3922, 2014.

[112] S. Kurtz, K. Ong, E. Lau, F. Mowat, and M. Halpern. Projections of primary and revision hip and knee arthroplasty in the united states from 2005 to 2030. *Journal of Bone and Joint Surgery*, 89:780–785, 2007.

[113] M. Long and H.J. Rack. Titanium alloys in total joint replacements - a materials science perspective. *Biomaterials*, 19:1621–1639, 1998.

[114] D.L.P. Macuvele, J. Nones, J.V. Matsinhe, M.M. Lima, and C. Soares. Advances in ultra high molecular weight polyethylene/hydroxyapatite composites for biomedical applications: A brief review. *Materials Science and Engineering C*, 76:1248–1262, 2017.

[115] A.M. DiGioia, B. Jaramaz, A.Y. Plakseychuk, J.E. Moody, C. Nikou, R.S. Labarca, T.J. Levision, and F. Picard. Comparison of a mechanical acetabular alignment guide with computer placement of the socket. *Journal of Arthroplasty*, 3:359–364, 2002.

[116] G. Pezzoti and K. Yamamoto. Artificial hip joints: The biomaterials challenge. *Journal of of the Mechanical Behavior of Biomedical Materials*, pages 3–20, 2014.

[117] A.A. Edidin and S.M. Kurtz. influence of mechanical behavior on the wear of 4 clinically relevant polymeric biomaterials in a hip simulator. *the Journal of Arthroplasty*, pages 321–331, 2000.

[118] X. Chen, C. Bai, and L. Xie. Inflammatory response to orthopedic biomaterials after total hip replacement. *Journal of Orthopedic Science*, 17:407–412, 2012.

[119] T. Fujishiro, S. Hayashi, N. Kanzaki, S. Hashimoto, M. Kurosaka, T. Kanno, and T. Masuda. Computed tomographic measurement of acetabular and femoral component version in total hip arthroplasty. *International Orthopedics*, 38:941–946, 2014.

[120] K.L. Moore, A.M. Agur, and A.F. Dalley. *Essential Clinical Anatomy*, volume 4. Lippincott Wiliams and Wilkins: Baltimore, MD, 2011.

[121] D.A. Neumann. *Kinesiology of the musculoskeleta system: Foundations for rehabilitation*, volume 4. Mosby Elsevier: St. Louis, MO, 2010.

[122] L.A. Fowkes, E. Petridou, C Zargorski, A. Karuppiah, and A.P. Toms. Defining a reference range of acetabular inclination and center-edge angle of the hip in asymptomatic individuals. *Skeletal Radiology*, 40:1427–1434, 2011.

[123] T.-Y. Tsai, D. Dimitriou, G. Li, and Y.-M. Kwon. Does total hip arthroplasty restore native hip anatomy? three-dimensional reconstruction analysis. *International Orthopedics*, 38:1577–1583, 2014.

[124] G.E. Lewinnek, J.L. Lewis, and R. Tarr. Dislocations after total hip arthroplasties. *journal of Bone and Joint Surgery*, 60, 1978.

[125] M. Weber, M. Woerner, B. Craiovan, F. Voellner, M. Worlicek, H.-R. Springorum, J. Grifka, and T. Renkawitz. Current standard rules of combined anteversion prevent prosthetic impingement but ignore osseous contact in total hip arthroplasty. *Internation Orthopedics*, 40:2495–2504, 2016.

[126] B.M. Jolles, P. Zangger, and P.F. Leyvraz. Factors predisposing to dislocation after primary total hip arthroplasty: a multivariate analysis. *Journal of Arthroplasty*, 17:282–288, 2002.

[127] K.H. Widmer and B. Zurfluh. Compliant positioning of total hip components for optimal range of motion. *Journal of Orthopedic Research*, 22:815–821, 2004.

[128] M. Lamontagne, M.L. Beaulieu, D. Varin, and P.E. Beaule. Lower-limb joint mechanics after total hip arthroplasty during sitting and standing tasks. *Journal of Orthopedic Research*, 30:1611–1617, 2012.

[129] B.K. Mock, A.S. Olsen, and B.A. Klatt. Abductor deficiency in total hip arthroplasty: Evaluation, diagnosis and treatment strategies. *Operative Techniques in Orthopedics*, 27:186–191, 2017.

[130] A. Zahar, A. Rastogi, and D. Kendoff. Dislocation after total hip arthroplasty. *Current Reviews in Musculoskeletal Medicine*, 6:350–356, 2013.

Appendix A: Matlab Scripts

A.1 Function for calculating kinematics from raw SolidWorks data

```
function [run_points,spline_fit,parameters,muscles,status] = getRunData
    (run_path)
%Gather data about a particular run and return calculations

% Data cell structure for folder of runs:
%   1. Kinematic Data*
%   2. Spline fit*
%   3. Input parameters*
%   4. RMSE values
%   5. Difference magnitudes

% Data cell structure for data to compare to:
%   1. Kinematic Data
%   2. Spline fit

% Parameter matrix structure:
%   1. Z-Damper
%   2. Y_Damper
%   3. Glute Damper
%   4. t_R
%   5. Muscle spline fit binary value

% Muscle force matrix structure:
%   1. Glute
%   2. Rectus femoris
%   3. Vastus L
%   4. Vastus M
%   5. Biceps femoris
%   6. Body weight
%   7. Abdominal force


% --------- INITIAL VARIABLES --------- %
% Data file names
data_files = {'COM Position.csv' 'Hip Position.csv' 'Parameters.csv'};

femur_L = 415.74; %Femur length
```

```
37  COM_L = 492.95; %Length from hip to COM
38  d_3 = 1000; %Horizontal distance from point to origin
39  knee_offset = 20; %Knee angle offset
40
41  act_perc = 50; %STS Percentage of full muscle activation
42
43
44  % Check for file existance
45  if ~exist(fullfile(run_path,'Run Data'),'dir') == 7
46      fprintf('%s is not a run.\n', run_path);
47      status = 0;
48      run_points = [];
49      spline_fit = [];
50      return;
51  end
52  status = 1;
53
54
55  % -------- INPUT PARAMETERS --------- %
56  path = fullfile(run_path,'Run Data',data_files{3});
57  parameters = zeros(7,1); %Initial blank cell matrix
58  parameters(1:3) = csvread(path,3,1,[3,1,5,1]); %Damper values
59
60  % Read muscle variables and convert to cell matrix
61  muscle_values = num2cell(xlsread(path,'B10:M17'));
62
63  % Create multidimensional cell matrix based on muscles
64  s = size(muscle_values); %Size of matrix
65  muscles = cell(s(1)-1,1);
66  muscles_temp = cell(2,s(2));
67
68  % Change NaN cells to blank, remove the blanks and separate by muscle/
       force
69  for a=1:s(1)-1
70      for b=1:s(2)-1
71          muscles_temp{1,b} = muscle_values{1,b+1};
72          muscles_temp{2,b} = muscle_values{a+1,b+1};
73
74          % Set all NaN cells to be blank
75          if isnan(muscles_temp{2,b})
76              muscles_temp{1,b} = [];
77              muscles_temp{2,b} = [];
78          end
79      end
80
81      % Convert back to double matrix (removes blank cells)
```

```
82        muscles_temp = cell2mat(muscles_temp);
83        muscles_temp(1,:) = muscles_temp(1,:)-0.5; %Subtract 0.5 from the
              time
84
85        % Store the data in a cell matrix
86        muscles{a} = muscles_temp;
87        clear muscles_temp;
88    end
89    clear s;
90
91    % Use glute values to determine percentage values
92    glute_max = min(muscles{1}(2,:)); %Find the maximum glute value
93    [~,column] = find(muscles{1}==glute_max); %Find location of max
94    parameters(4) = muscles{1}(1,column(1)); %Get the timing of max
95    clear column glute_max;
96
97    % Determine if cubic spline fitting is used and adjust points
98    spline_val = xlsread(path,'B10:B20');
99    parameters(5) = spline_val(end);
100   clear spline_val;
101
102   %Determine conversion rate from time to percentage based on muscle
          timing
103   rate = act_perc/parameters(4);
104   parameters(4) = act_perc; %Change from timescale to percent scale
105   clear act_per;
106
107   % Loop through each muscle to make adjustments
108   for a=1:length(muscles)
109       % Adjust each timestamp from seconds to percentage
110       muscles{a}(1,:) = muscles{a}(1,:) * rate;
111
112       % Add additional values to the end of the force matrix for 100
              percent
113       n = length(muscles{a}(1,:));
114       muscles{a}(1,n+1) = 100;
115       muscles{a}(2,n+1) = muscles{a}(2,n);
116       clear n;
117   end
118
119
120   % --- SPLINE FIT FOR MUSCLES --- %
121   % Loop through each muscle to make adjustments (except TBW)
122   for a=1:length(muscles)
123       temp_array(1:2,1) = muscles{a}(1:2,1); %Temp array for this muscle
124
```

```
125         % Loop through each value comparing with the following value
126         for b=1:length(muscles{a}(1,:))-1
127             %Spline fit matricies
128             x = [muscles{a}(1,b) muscles{a}(1,b+1)];
129             y = [muscles{a}(2,b) muscles{a}(2,b+1)];
130 
131             %Check if the timestamp is a duplicate
132             if x(1) ~= x(2)
133                 p_spline(1,:) = linspace(x(1),x(2),200);
134                 if parameters(5) == 1 && a ~= 6
135                     p_spline(2,:) = spline(x,[0 y 0],p_spline(1,:));
136                 else
137                     p_spline(2,:) = spline(x,y,p_spline(1,:));
138                 end
139 
140                 n = length(temp_array); %Current temp_array size
141                 n2 = length(p_spline(1,:)); %Number of values used
142 
143                 temp_array(1:2,n+1:n+n2) = p_spline;
144                 clear n n2 x y p_spline;
145             end
146         end
147 
148         muscles{a} = temp_array;
149         clear temp_array;
150     end
151 
152 
153     % --------- KINEMATIC DATA --------- %
154     % Gather position data
155     com_pos = csvread(fullfile(run_path,'Run Data',data_files{1}),2,0);
156     hip_pos = csvread(fullfile(run_path,'Run Data',data_files{2}),2,0);
157 
158     % Make sure the timing variables are the same for both sets of points
159     if length(hip_pos) == length(com_pos)
160         run_points = zeros(length(hip_pos),3); %Single array for data
161 
162         if hip_pos(:,1) == com_pos(:,1)
163             run_points(:,1) = hip_pos(:,1); %Time points
164             run_points(:,2) = com_pos(:,2); %Lengths that determine hip
                    angles
165             run_points(:,3) = hip_pos(:,2); %Lengths that determine knee
                    angles
166         else
167             % What to do if the time values are not the same
168             disp('Array mismatch');
```

```
169             return;
170         end
171     else
172         % What to do if the the number of timestamps are not the same
173         disp('Array mismatch');
174         return;
175     end
176     clear hip_pos knee_pos;
177
178     % Remove all data from before time t=0.5 add in percentage values
179     index = find(run_points(:,1)==0.5,1);
180     run_points = run_points(index:length(run_points),:);
181     run_points(:,1) = (run_points(:,1) - 0.5)*rate;
182     clear index;
183
184     %Adjust run data to make sure there is a max percentage value of 100%
185     run_points = run_points(run_points(:,1)<=100,:);
186
187
188     % --- ANGLE CALCULATIONS --- %
189     % Pelvis Angles
190     % Determine the initial offset of the COM (it is not perfectly vertical
        )
191     offset = run_points(1,2) - run_points(1,3);
192     hip_offset = asin(offset/COM_L)*(180/pi());
193     clear offset;
194
195     % Find the difference between com and hip lengths
196     dist = run_points(:,2) - run_points(:,3);
197
198     % Correct for any data that is longer than COM_L (weird results)
199     dist(dist > COM_L) = COM_L - 0.01;
200     dist(dist < (-1*COM_L)) = (-1*COM_L)+0.01;
201
202     % Calculate the angles
203     run_points(:,2) = (asin(dist(:,1)/COM_L)*(180/pi()))-hip_offset;
204     clear dist;
205
206
207     % Knee Angles
208     %Offset the data by d_3
209     dist = d_3 - run_points(:,3);
210
211     %Correct for any data that is longer than COM_L (weird results)
212     dist(dist > femur_L) = femur_L-0.01;
213     dist(dist < (-1*femur_L)) = (-1*femur_L)+0.01;
```

```
214
215 %Use trig to calculation the actual angle considering negative values
216 run_points(:,3) = 90 - acosd((dist(:,1)/femur_L)) + knee_offset;
217 clear dist;
218
219 % Fit a spline to the data (only for tar_data)
220 spline_fit{1} = csaps(run_points(:,1),run_points(:,2));
221 spline_fit{2} = csaps(run_points(:,1),run_points(:,3));
222
223
224 end
```

A.2 Function for comparing data sets

```
1  function [error,diff_mag,rmse_array] = compData(run_data,tar_data,val,
       error_max)
2  % This function compares the input run data with the given target data
       both
3  % provided by the GUI interface
4
5  % Change run data if target data goes to a lower value
6  tar_spline = tar_data{2};
7  tar_data = tar_data{1};
8  comp_to = min(tar_data(end,1),run_data(end,1));
9  comp_to = min(comp_to,val);
10 run_data = run_data(run_data(:,1)<=comp_to,:);
11 clear tar_data;
12
13 % Generate target data points from the run data and spline fit
14 % (Need to adjust if target data is less than run data)
15 tar_data(:,1) = run_data(:,1);
16 tar_data(:,2) = fnval(tar_spline{1}, tar_data(:,1));
17 tar_data(:,3) = fnval(tar_spline{2}, tar_data(:,1));
18
19 % Error calculations
20 diff_mag = zeros(length(tar_data(:,1)),2);
21 rmse_array = zeros(length(tar_data(:,1)),2);
22 error = zeros(10,1);
23 for a=1:2
24     % Difference magnitudes
25     diff_mag(:,a) = abs(run_data(:,a+1) - tar_data(:,a+1));
26
27     % RMSE calculations
28     squ_err(:,1) = diff_mag(:,a).^2;
```

```
29        error(a) = sqrt(mean(squ_err));
30
31        % RMSE calculations for data below target value
32        error(a+2) = sqrt(mean(squ_err(run_data(:,1)<=val,1)));
33
34        % Array with rmse for each step
35        for b=1:length(squ_err)
36            rmse_array(b,a) = sqrt(mean(squ_err(1:b,1)));
37        end
38
39        % Determine the percentage validated to
40        if error(a) <= error_max
41            error(a+4) = run_data(end,1);
42        else
43            % Find where the difference is greater than the error threshold
44            index = rmse_array(:,a) > error_max;
45            rmse_error = run_data(index,1);
46            error(a+4) = rmse_error(1);
47        end
48
49        % Find where true deviation begins and the max deviation accounting
              for
50        % initial position
51        dev_index = find(diff_mag(:,a) > 0.1 + diff_mag(1,a));
52        if ~isempty(dev_index)
53            error(a+6) = dev_index(1);
54            [~,error(a+8)] = max(diff_mag(:,a));
55            clear dev_index;
56        else
57            error(a+6) = 0;
58            error(a+8) = 0;
59        end
60    end
61
62    clearvars -except error diff_mag rmse_array;
63    end
```

Appendix B: Contact Result Images

%	Acetabular Cartilage Contact		Labrum Contact	
	KT170 - Healthy	KT170 - FAI	KT170 - Healthy	KT170 - FAI
0	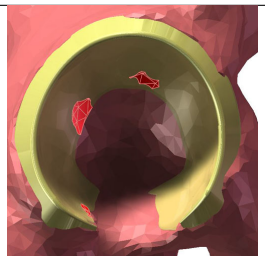	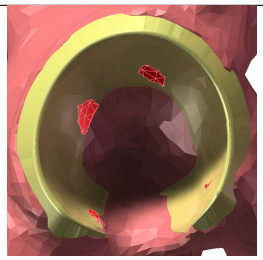	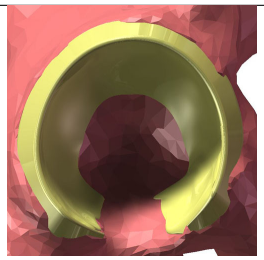	
17.5	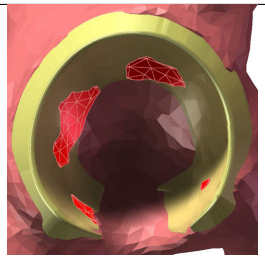	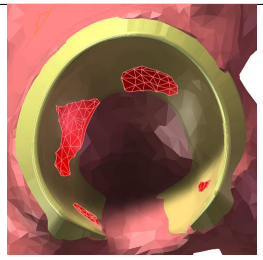		
35	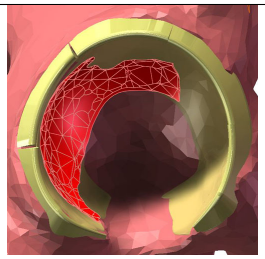	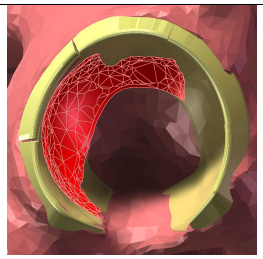	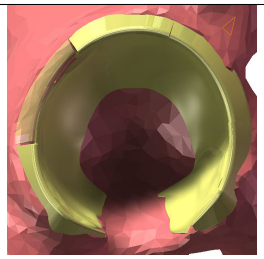	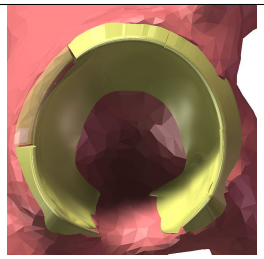
52.5	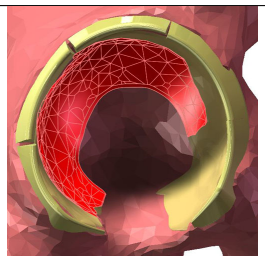	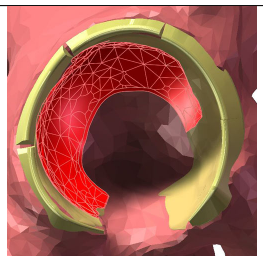	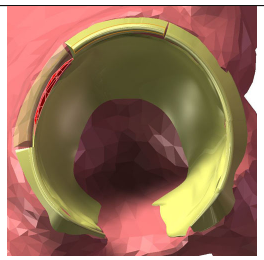	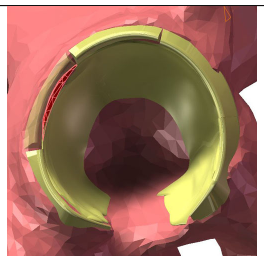
70	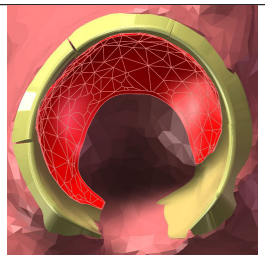	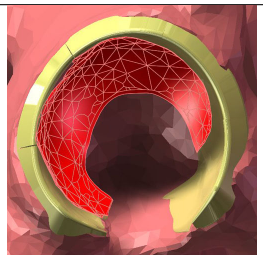	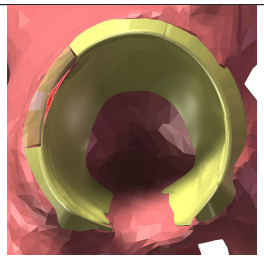	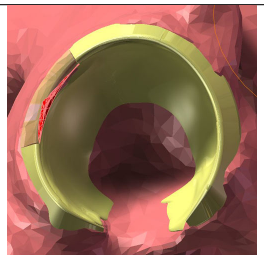

%	Acetabular Cartilage Contact		Labrum Contact	
	KT226 - Healthy	KT226 - FAI	KT226 - Healthy	KT226 - FAI
0	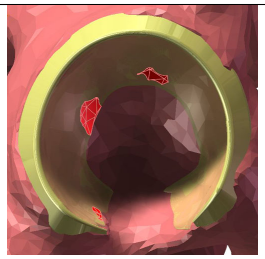	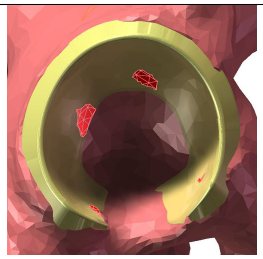	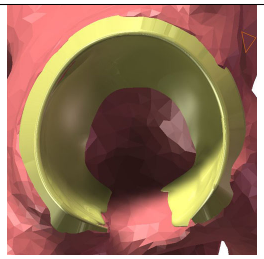	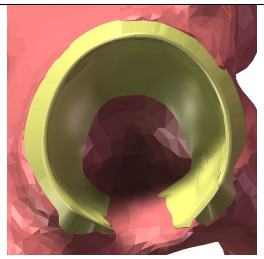
17.5	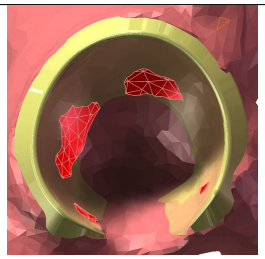	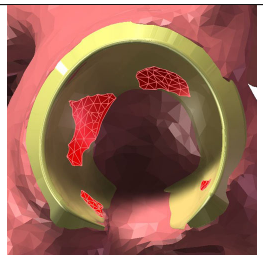	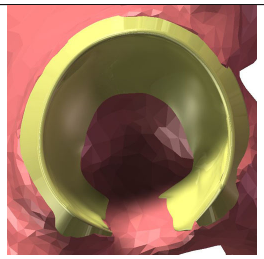	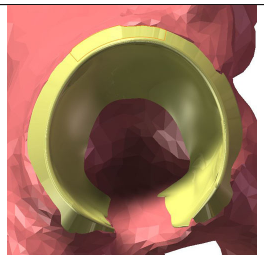
35	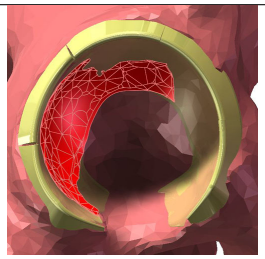	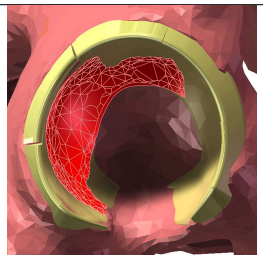	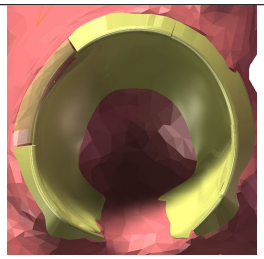	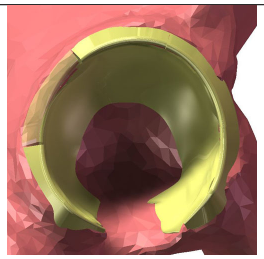
52.5	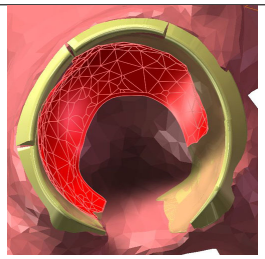	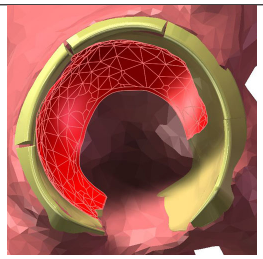	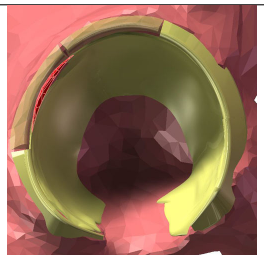	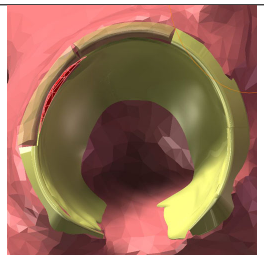
70	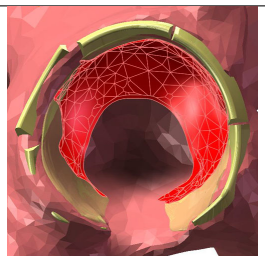	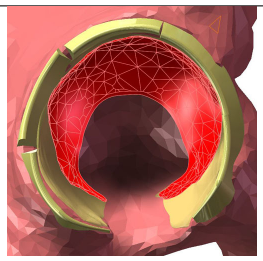	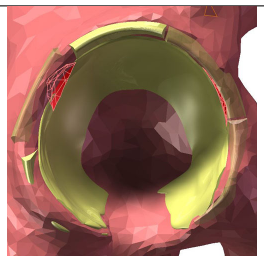	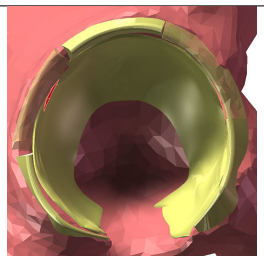

%	Acetabular Cartilage Contact		Labrum Contact	
	KT227 - Healthy	KT227 - FAI	KT227 - Healthy	KT227 - FAI
0	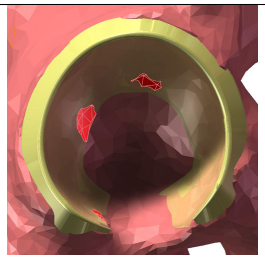	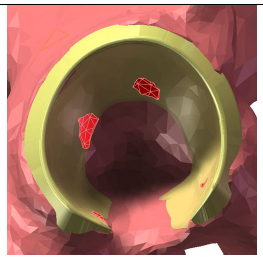	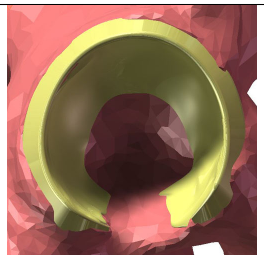	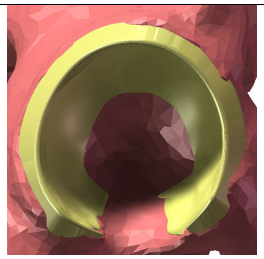
17.5	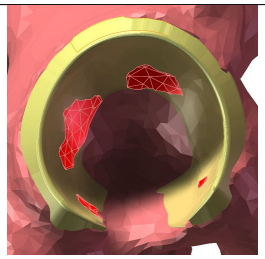	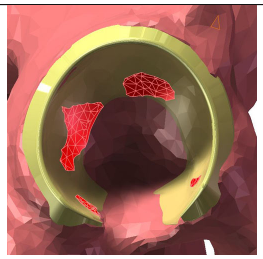	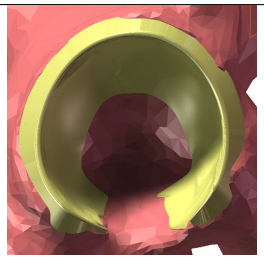	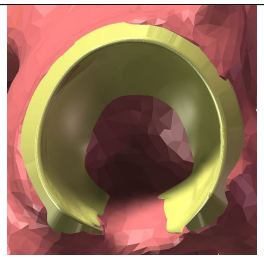
35	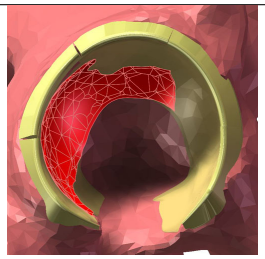	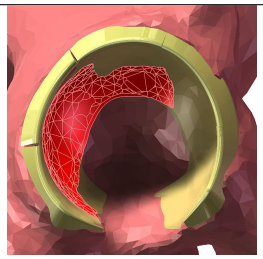	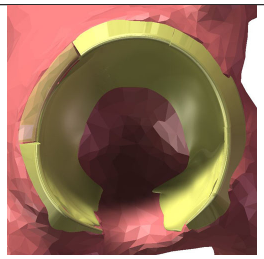	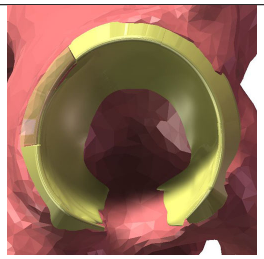
52.5	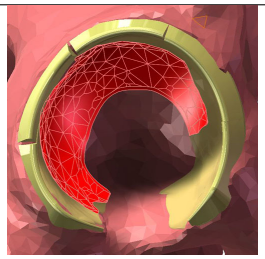	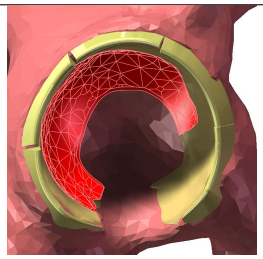	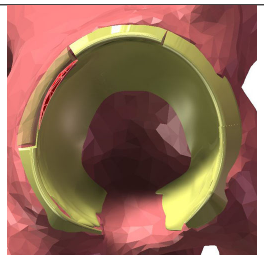	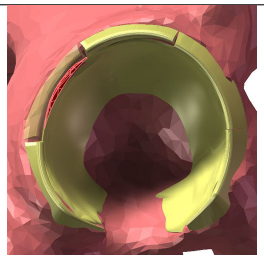
70	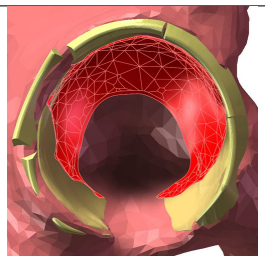	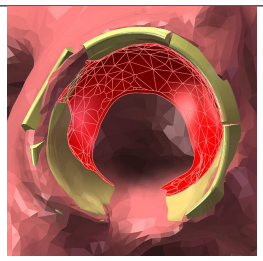	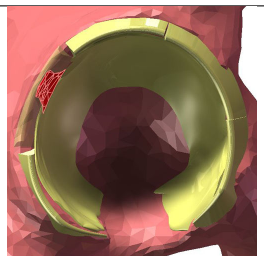	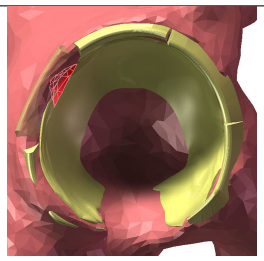

Vita

Brandon Keith Marine was born on April, 3^{rd} 1991 in Fairfax, Virginia but was raised in Fredericksburg, Virginia. He graduated from James Monroe High School in June of 2009. After High School, Brandon attended Virginia Polytechnic Institute and State University where he was an active member of the Student Government Association as a representative of the College of Science and worked a Biotechnology laboratory under the direction of Dr. Kristi DeCourcey. He graduated with his Bachelor of Arts in Physics with a concentration in Medicine in May of 2014. Immediately after graduation, he spent a year and a half working under Dr. Kash Eagleton and Dr. Marshall Rennie at Orthopedic and Sports Physical Therapy Associates, gaining clinical experience. In August 2015 Brandon enrolled in a Master of Science in Biomedical Engineering program at Virginia Commonwealth University, under the guidance of Dr. Jennifer S. Wayne, conducting research on orthopedic biomechanics. Following graduation, Brandon plans to enter industry to continue with computational approaches applied towards medicine.